# Study on the influence of Nuclear Deformation on the Pygmy Dipole Resonance in Samarium isotopes

Harshna Jivan

A thesis submitted to the Faculty of Science,University of the Witwatersrand,
in fulfillment of the requirements for the
Degree of Doctor of Philosophy

*Supervisor* Dr. Luna Pellegri
*Co-Supervisor* Prof. Elias Sideras-Haddad

Johannesburg, 2023

# Declaration

I, Harshna Jivan, hereby declare that this Thesis is my own, unaided work. It is being submitted for the Degree of Doctor of Philosophy in Physics at the University of the Witwatersrand, Johannesburg. It has not been submitted before for any degree or examination at any other University.

Harshna Jivan

28 day of September 2023 in Johannesburg, South Africa.

For Her,

The one who carried her even before she carried me,

Who fed my heart and showed me that I could play with carefree glee,

My sweet and precious Aji.

.

For Her,

The one that nurtured me,

Who fed my wild imagination and grew my curiosity,

My dear darling Mummy.

.

For Her,

The one that always stood beside me,

Who held my hand and lead the way between dreaming to possibility,

My inspiring Sis, Rupli.

# Acknowledgements

I am extremely grateful to my advisors, Dr Pelegri and Prof Haddad for their guidance, advice, patience and continuous support over the course of my PhD study. Thank you both for believing in my capabilities and not letting me give up despite my personal challenges.

To Luna, you're mentorship has been invaluable in introducing me to the niche of PDR studies as well as in helping me navigate through the intricacies that analyzing these data-sets entailed. Thank you for your commitment to me and this project. I would not have reached the finish line without your guidance or support. From the very first day that I arrived at iThemba LABS, you welcomed me with open arms and took me under your wing. I truly appreciate the bond that we have built, the life lessons shared and all the opportunities I got to experience along this journey.

To Prof Haddad, thank you for steering me towards joining the Wits Nuclear Structure Group, encouraging me to take on this endeavor and providing the opportunity for me to spend time based at iThemba LABS. I am grateful for your insight and perspectives shared with me about life, physics and everything in-between. Thank you for your genuine care and fatherly advice in helping me navigate through my personal challenges.

A big hearty Thank You to the iThemba LABS Beam staff and all the BaGeL campaign collaborators for all their efforts during the setting up of equipment and for dedicating their time to taking shifts and ensuring a successful experimental run. A special mention goes to Dr Retief Neveling, Dr Ricky Smit, Dr Paul Papka, Dr Lindsay Donaldson, Dr Phil Adsley, Dr Vicente Pesudo and Dr Daniel Marin Lambarri. I have had the fortunate pleasure to work alongside each of you and have gained so much as a result. Thank you to Dr Ntombi Kheswa for making the targets needed for the experiments.

To Retief and Phil, thank you for showing me the ropes behind the K600 analyser, assisting me in the integration of the gamma analysis codes and for teaching me so many nifty coding tips and tricks. Thank you both for sharing your insights and opinions in the analysis and also for your willingness to troubleshoot through the various challenges encountered along the way.

Thank you to Dr Edoardo Lanza for performing the semi-classical model calculations in order to extract the theoretical cross-sections needed to interpret the experimental data. Thank you for taking the time to explain each step of the calculation in detail, aiding in my understanding of the theoretical description of the PDR and for making my time in Catania so memorable. Thank you also to Dr Elena Litvinova and Dr Kenichi Yoshida for providing the transition density calculations required for the semi-classical model calculations for the $^{144}$Sm and $^{154}$Sm cases respectively.

The financial assistance of the National Research Foundation (NRF) towards this research is hereby acknowledged. Opinions expressed and conclusions arrived at, are those of the author and are not necessarily to be attributed to the NRF. I also wish to thank thé L'Oréal-UNESCO For Women in Science Sub-Saharan Africa Programme for the endowment awarded to me towards my PhD research.

And finally, to my family and friends, I truly appreciate all the support and care each of you have given me. To my three pillars of support, Mum, Rupal and Nish, no words could suffice to express the gratitude I have for everything you all have been for me over these last few years. Thank you for believing in me so fiercely, for supporting my choices and decisions, for accepting my weird eccentricities and loving me for who I am. No matter how big any challenge presents, I know that I can get through it as long as I have you three on my team. From the top of my head to the bottom of my toes, out of every bit of me, appreciation flows!

# Abstract

The past decade has seen an increase in studies dedicated to understanding the low-lying electric dipole (E1) response, commonly referred to as the Pygmy Dipole Resonance (PDR). These studies revealed that the PDR has a mixed isospin nature, and that the use of complimentary probes is needed to fully understand this response. Since majority of studies on the PDR focused on spherical nuclei, the influence that deformation has on the PDR response is yet to be understood. Preliminary relativistic proton scattering studies on $^{154}$Sm performed at RCNP (Japan), showed potential evidence for a splitting in the PDR response similar to that of the Giant Dipole Resonance with deformation. A tentative interpretation suggested that this splitting could be connected to the splitting of the resonance structure with respect to the K quantum number. Theoretical studies considering the deformed HFB+QRPA model however, suggest that this splitting is connected to the isospin mixed character of these states as observed in spherical nuclei.

The isoscalar responses of the spherical $^{144}$Sm and axially deformed $^{154}$Sm isotopes were investigated for the first time using the inelastic scattering of alpha particles at 120 MeV. The comparative experiments were performed at iThemba LABS in South Africa, coupling together for the first time, the K600 magnetic spectrometer in zero-degree mode with the BaGeL (Ball of Germanium and LaBr3:Ce detectors) array. The particle-gamma coincidence measurement was used to obtain the cross section for the population of the pygmy states. In both nuclei, the region of the PDR was excited and the E1 multipolarity of the transitions was supported by the angular correlation between the $\alpha$-particles and the co-incident $\gamma$-rays measured.

The total exclusive cross section measured for $^{144}$Sm amounted to $24.3 \pm 3.8$ mb/sr while for $^{154}$Sm to $18.8 \pm 2$mb/sr. The experimental results were compared with the prediction

of the RQTBA and the deformed HFB+QRPA theories, respectively. The theoretical cross sections were extracted within a semiclassical coupled-channel approach. The fragmentation observed in the experiment for the $^{144}$Sm was underestimated by the calculations, although good agreement with the total cross section measured was found. In the case of the deformed $^{154}$Sm however, the experimental cross section accounted for only 52% of the predicted cross section in the same excitation region.

The isoscalar response extracted in this thesis was compared with the isovector strength obtain from an experiment performed at RCNP using the relativistic proton scattering at forward angles. The double hump observed in the isovector channel was not found in the case of the isoscalar strength. This implies that the difference obtained between these two experiments is related to the "isospin splitting" of the PDR rather than a splitting of the strength connected with the K quantum number.

# Table of Contents


**1 Introduction** **1**

**2 Review of the PDR** **5**

2.1 Macroscopic description . . . . . 5

2.2 Microscopic description . . . . . 6

2.3 Experimental studies of the PDR . . . . . 10

2.4 The PDR with deformation . . . . . 13

**3 Theoretical considerations** **16**

3.1 Cross-section calculations . . . . . 16

3.2 Angular Correlations . . . . . 19

**4 Experimental Techniques and Equipment** **23**

4.1 iThemba LABS accelerator facilities . . . . . 24

4.2 The K600 magnetic spectrometer . . . . . 26

4.3 The Focal Plane detector system . . . . . 27

4.3.1 Multiwire Drift Chamber . . . . . 27

4.3.2 Paddle detector . . . . . 29

4.4 The BaGeL array . . . . . 29

4.5 Signal Processing and DAQ . . . . . 32

4.5.1 Electronics . . . . . 32

4.5.2 DAQ system . . . . . 34

**5 Data Analysis** **36**

5.1 K600 Focal-Plane Data reduction . . . . . 36

5.1.1 Particle identification . . . . . 39

5.1.2 VDC position tracking . . . . . 41

5.1.3 VDC efficiency . . . . . 47

5.1.4 Line-shaping procedures . . . . . 48

5.1.5 Energy Calibration . . . . . 50
5.2 BaGeL - Clover Data reduction . . . . . 55
5.2.1 Energy Calibration . . . . . 55
5.2.2 Gamma Time Selection . . . . . 57
5.2.3 Addback . . . . . 60
5.2.4 Clover Efficiencies . . . . . 61
5.3 The Coincidence matrix . . . . . 62
5.4 Background subtraction . . . . . 66
5.5 Contaminant Subtraction . . . . . 69
5.6 Cross Sections . . . . . 69
5.7 Multipolarity assessment . . . . . 70

**6 Results and Discussion** **76**
6.1 Co-incidence matrix and extracted decay spectra . . . . . 77
6.2 $^{144}$Sm vs $^{154}$Sm . . . . . 78
6.3 Theoretical Modelling . . . . . 80
6.3.1 $^{144}$Sm . . . . . 81
6.3.2 $^{154}$Sm . . . . . 83
6.4 $(\alpha, \alpha'\gamma)$ vs $(\gamma, \gamma')$ . . . . . 87
6.5 $(\alpha, \alpha'\gamma)$ vs $(p, p')$ . . . . . 89

**7 Conclusions** **91**

# List of Figures

1.1 An illustrative depiction of the Electric dipole (E1) excitations typically observed for spherical nuclei. . . . . 2

2.1 The isovector and isoscalar dipole strength distribution obtained from HF plus QRPA with SGII interaction model calculations [21] for isotopes of Ca, Ni, Zr and Sn as presented in ref.[18]. The results are smoothed using a Lorentzian of width 1-2 MeV. The electromagnetic responses are shown in the upper panels in red and the isoscalar responses are shown in blue. . . . . 8

2.2 QPM calculations of the reduced transition probabilities B(E1) for $^{136}$Xe comparing different phonon coupling configurations taken from ref.[22]. Panel (a) shows the results for when only one-phonon states are taken into account, (b) when coupling up to two-phonons are included and (c) when coupling up to three-phonons are included. . . . . 9

2.3 Results of the dipole response obtained in a HF+RPA calculation with a SGII interaction for the $^{68}$Ni nucleus. In the left part, the isovector (top frame) and isoscalar (bottom frame) (multiplied by $-1$) strength functions calculated by convoluting the corresponding reduced transition probability with a Lorenzian of 1 MeV width are shown. The regions for the PDR, IVGDR and ISGDR excitation modes is indicated. In the left part, the proton and neutron transition densities (upper frames) and isoscalar and isovector transition densities (lower frames) are shown, for the dipole states at energies 10.8 MeV (PDR), 15.6 MeV (IVGDR) and 31.6 MeV (ISGDR). Images adapted from [16]. . . . . 11

2.4 Average cross sections measured in $^{128}$Te and $^{130}$Te with quasi-monochromatic photons. Panels (a) and (b) depict the total elastic cross section (blue squares) highlighting the contribution of the strength in peaks with green open squares. Panels (c) and (d) shows the photoabsorption cross sections dividing the contributions into total elastic (blue squares), inelastic (red triangles) component. The total cross section below particle emission threshold is shown with black circles and the one obtained from $(\gamma, n)$ measurement is shown with green diamonds. Images obtained from [25]. . . . . 13

3.1 Deflection function for the system $\alpha$+$^{144}$Sm at $E_\alpha = 120$ MeV. The horizontal lines indicate the experimental $\alpha$-scattering angle range. . . . . 19
3.2 Deflection function for the system $\alpha$+$^{154}$Sm at $E_\alpha = 120$ MeV. The horizontal lines indicate the experimental $\alpha$-scattering angle range. . . . . 20
3.3 Angular correlations obtained from ANGCOR after averaging over the opening angle of the K600 spectrometer for $^{144}$Sm, $^{154}$Sm, $^{24}$Mg and $^{16}$O. Green, pink and blue correspond to dipole, quadrupole and octapole modes respectively 22

4.1 Photograph of the experimental set-up in the K600 vault at iThemba LABS 23
4.2 A schematic layout of the accelerator and ancillary facilities at iThemba LABS [0]. . . . . 25
4.3 Schematic layout of the K600 magnetic spectrometer. Scattered particles enter the spectrometer via the scattering chamber and are focused by the magnets on the high dispersion focal plane where they are measured by the Focal Plane Detection System (FPDS). . . . . 26
4.4 Photograph of the UX type MWDC as mounted near the focal plane (left) and the U-type wireplane (right) where the wires are inclined at 50°. . . . . 28
4.5 Example of the drift lines associated with a typical particle track travelling through the VDC. . . . . 29
4.6 Photograph of a set of paddle detectors with the scintillators wrapped in foil. The PMT's are not mounted here. . . . . 30
4.7 Photographs of BaGeL taken during experiments on $^{144}$Sm. The detectors positioned to the left and right of the incoming beam are shown in the left and right panels respectively. The beam direction is indicated with yellow arrows. . . . . 31
4.8 A schematic diagram of the electronics for the K600 focal plane detector system. 33
4.9 A schematic diagram of the BaGeL electronics in Exp1. . . . . 34

4.10 A schematic diagram of the BaGeL electronics in Exp2. . . . . 35

5.1 Variation in Focal plane X position with run entries before and after offset implementation for chained $^{24}$Mg data in Exp2. . . . . 38
5.2 PID spectra shown for $^{24}$Mg, $^{144}$Sm and $^{154}$Sm in the top, middle and bottom panels respectively. . . . . 40
5.3 TDC reference times for the various TDC channels of the VDC wires for Exp2, showing the effect of implementing the cable offset to align the trailing edge of the drift time distributions . . . . . 42
5.4 The Look-up table (LUT) for the X wireplane used in Exp2 . . . . . 43
5.5 Schematic diagram of a typical trajectory associated with a charged particle passing through a wire-plane, resulting in a V type structure. . . . . 44
5.6 Schematic diagram of an event track triggering a "W" type structure . . . . 44
5.7 Schematic diagram of an event track triggering a "Z" type structure . . . . . 45
5.8 Logic flow in the ray-tracing procedure for determining which drift distance is allocated when multi-hits are fired for a triggered wire. . . . . 46
5.9 Relative particle Time of Flight vs Focal plane position zoomed in on the 250mm (left) and 615 mm (right) $^{24}$Mg target peaks highlighting the slanting in peaks that affect the position resolution. . . . . 48
5.10 Line-shaping correction parameter extraction as implemented on the 6.432 MeV state around 615 mm. . . . . 49
5.11 ToF vs Focal plane position after implementing the line-shaping correction. . 49
5.12 Schematic of the kinematics of a nuclear reaction . . . . . 50
5.13 Focal Plane X position for $^{24}$Mg data indicating the peaks used in the calibration. . . . . 52
5.14 Rigidity calibration curves fitted with a $3^{rd}$ order polynomial function for each experiment as indicated . . . . . 54
5.15 Calibrated Excitation energy spectra for $^{24}$Mg targets of (a) 0.7mg/cm$^3$ and (b) 3.3 mg/cm$^3$ thickness. . . . . 54
5.16 Decay scheme for the 6.432 MeV excited state in $^{24}$Mg. The relative intensities for the gamma decays are indicated in the brackets below the corresponding gamma energy. . . . . 56
5.17 Calibrated gamma decay spectrum for all clovers summed with a selection on the 6.432 MeV excited state in $^{24}$Mg. . . . . 56
5.18 The time spectrum for an individual HPGe detector from each experiment, measured relative to the radio frequency (RF) of the SSC . . . . . 58

5.19 Matrix of Gamma Time for each Clover detector segment during Exp2. . . . 59
5.20 Matrix showing the variation in Gamma time for full Clover array with run entries in the chained $^{24}$Mg data from Exp2. . . . . 59
5.21 Comparison of the Clover Addback mode vs singles mode $\gamma$-decay spectra from the 6.432 MeV excited state in $^{24}$Mg. . . . . 60
5.22 The $\alpha$-$\gamma$ coincidence matrix obtained for $^{24}$Mg data measured in Exp1. A good correlation between the $\alpha$ excitation energies ($E_x$) measured by the K600 focal plane detectors and their corresponding $\gamma$-decay ($E_\gamma$) measured by the BageL Clover detectors can be observed. The black diagonal band indicates $\gamma$-decays to the ground state, while the magenta band indicates decays to the $1_{st}$ excited state at 1.368 MeV. . . . . 63
5.23 Projections of the $\gamma$-ray spectra (left panel) and excitation-energy spectra (right panel) from the $^{24}$Mg$(\alpha, \alpha'\gamma)$ data, without any gating condition (top), gated on ground state transitions (middle) and gated on transitions to the $1^{st}$ excited state (bottom). . . . . 64
5.24 The $\alpha$-$\gamma$ coincidence matrix obtained for $^{144}$Sm data measured in Exp2. The $\alpha$ excitation energies ($E_x$) measured by the K600 focal plane detectors are shown on the x-axis and their corresponding $\gamma$-decay ($E_\gamma$) measured by the BageL Clover detectors are shown on the y-axis. The black diagonal band indicates $\gamma$-decays to the ground state, while the magenta band indicates decays to the $1_{st}$ excited state at 1.66 MeV. . . . . 65
5.25 The $\alpha$-$\gamma$ coincidence matrix obtained for $^{154}$Sm data measured in Exp2. The $\alpha$ excitation energies ($E_x$) measured by the K600 focal plane detectors are shown on the x-axis and their corresponding $\gamma$-decay ($E_\gamma$) measured by the BageL Clover detectors are shown on the y-axis. The black diagonal band indicates $\gamma$-decays to the ground state, while the magenta band indicates decays to the $1_{st}$ excited state at 81.98 keV. . . . . 65
5.26 Plot of the time at which measured $\gamma$-particles arrived at the clover detectors with respect to the RF of the SSC . The selected off-prompt used for generating the random co-incidence background matrix is indicated by the black dashed lines. . . . . 67
5.27 Background matrix with the gated band region indicated in black dashed lines 67
5.28 $^{144}$Sm ground state decay counts spectra with background. . . . . 68
5.29 $^{154}$Sm ground state decay counts spectra with background. . . . . 68
5.30 Comparison of counts corrected with efficiencies for detectors at $\theta = 90^\circ$ and $\theta = 135^\circ$ in Exp1 . . . . . 71

5.31 Comparison of counts corrected with efficiencies for detectors at $\theta = 90°$ and $\theta = 155°$ in Exp2 . . . . . 72
5.32 Multipolarity assessment for individual states in $^{144}$Sm . . . . . 72
5.33 Multipolarity assessment for the broad range of states in $^{144}$Sm . . . . . 73
5.34 Multipolarity assessment for the broad range of states in $^{154}$Sm . . . . . 73
5.35 Multipolarity assessment for states identified in $^{24}$Mg . . . . . 74
5.36 Multipolarity assessment of contaminant peaks . . . . . 75

6.1 $^{144}$Sm co-incidence matrix and direct decay projection . . . . . 77
6.2 $^{154}$Sm co-incidence matrix and direct decay projection . . . . . 78
6.3 $^{144}$Sm Vs $^{154}$Sm Cross-sections . . . . . 79
6.4 RQTBA predicted proton and neutron transition densities for the dipole state at 6.88 MeV in $^{144}$Sm . . . . . 82
6.5 Comparison between measured and calculated cross sections for $^{144}$Sm . . . . 82
6.6 Comparison between the experimental extracted and theoretical calculated summed cross-sections for $^{144}$Sm. . . . . 83
6.7 Deformed HFB+QRPA predicted proton and neutron transition densities for the K=0 and K=1 dipole states at 7.49 MeV and 7.33 MeV respectively in $^{154}$Sm . . . . . 84
6.8 Comparison between measured and calculated cross sections for $^{154}$Sm . . . . 85
6.9 Comparison between the experimental extracted and theoretical calculated summed cross-sections for $^{154}$Sm . . . . . 86
6.10 Comparison of PDR states observed $^{144}$Sm measured using the $(\alpha, \alpha'\gamma)$ reaction channel in this study vs the $(\gamma, \gamma')$ reaction channel measured in [56] . . . . . 88
6.11 Electric dipole cross-section obtained in $^{154}$Sm(p,p') experiments at RCNP [12] . . . . . 90

# List of Tables

4.1 Table summarising technical details of BaGeL for $^{154}$Sm experiments . . . . 31
4.2 Table summarising technical details of BaGeL for $^{144}$Sm experiments . . . . 32

5.1 Summary of parameters used for the rigidity calibration in Exp1 . . . . . 53
5.2 Summary of parameters used for the rigidity calibration in Exp2 . . . . . 53

# Chapter 1

# Introduction

The atomic nucleus is a fascinatingly complex system. Whilst one would expect such a system with many degrees of freedom to behave in a chaotic and disorderly manner when subjected to an external stress, instead it is able to self organise into simple modes of collective motion. The modes of collective motion that manifest in the form of vibrations are of particular interest to the field of nuclear structure physics as studying their properties can provide better insight into the bulk properties and the non-equilibrium dynamics of nuclei.

In this thesis, particular attention is drawn to the Electric dipole (E1) response observed in atomic nuclei. The E1 strength is almost entirely exhausted by the Giant Dipole Resonance (GDR), located in the energy range of 10-20 MeV. A small contribution to the strength however, comes from a number of low-lying $1^-$ states concentrated around the neutron-separation threshold. These states are frequently denoted as the Pygmy Dipole Resonance (PDR). The typical E1 dipole response observed for spherical nuclei is illustrated in Fig.1.1.

Within the hydrodynamic model, the PDR has been interpreted as an oscillation of excess neutrons against a proton-neutron saturated core [1, 2]. Its connection to the neutron skin, therefore, makes investigations of the PDR particularly important. The neutron-skin thickness has been linked to several parameters that influence the Equation of State (EOS), including the nuclear polarizability [3, 4] as well as the symmetry energy [5]. In addition, since the PDR falls in the region of the neutron separation energy, it has an influence on the r-process particularly in the synthesis of heavier nuclei [6] and also has an impact on the

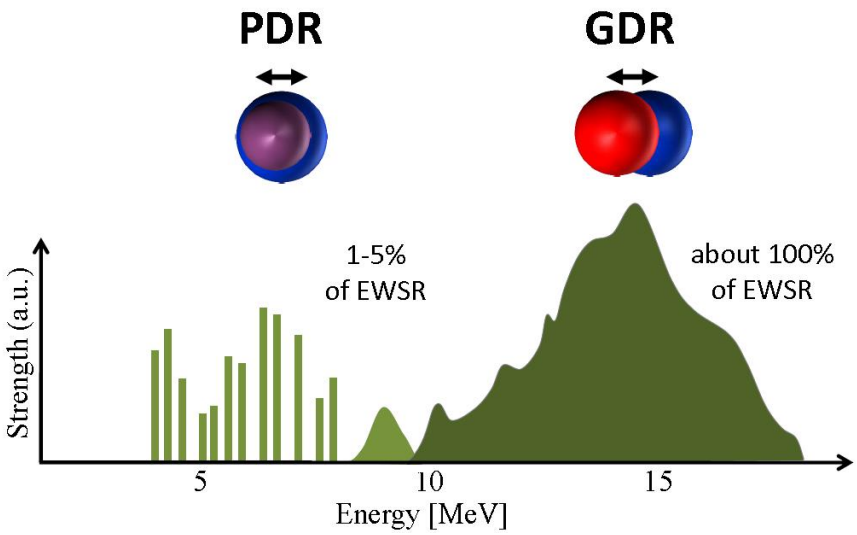


Figure 1.1: An illustrative depiction of the Electric dipole (E1) excitations typically observed for spherical nuclei.

gamma strength function at the particle threshold [7]. Studies that contribute to an accurate understanding of the PDR strength and which aid towards building a microscopic picture of the underlying structure behind this low-lying strength are therefore highly desirable.

The PDR has been studied over a range of nuclei, spanning several mass regions across the nuclear chart. Complementary studies comparing the use of hadronic probes such as $\alpha$-particles and $^{17}$O with that of $\gamma$-ray probes, revealed a structural splitting of the PDR. These findings imply that a higher-lying subset of states (populated better with $\gamma$-ray probes) display more isovector (IV) characteristics, while the lower-lying states (populated by both probe types) have a strong isoscalar (IS) component. Although previous studies have provided a wealth of information on the PDR, they have been mostly concentrated on spherical nuclei and only very recently have studies turned focus to deformed nuclei.

In the case of the GDR, the role of deformation has been studied in Sm and Nd isotope chains using both $\gamma$-ray and $\alpha$-particle probes. These studies revealed a splitting in the response whereby a lower-energy component of the GDR became more prominent with increasing deformation, giving the appearance of a double-hump structure [8, 9, 10]. This splitting has been attributed to the different contributions arising from the K=0 and K=1 quantum numbers as defined along and perpendicular to the nuclear deformation axis.

Preliminary (p,p') studies on $^{154}$Sm performed at the Research Center for Nuclear Physics (RCNP) [11, 12], showed potential evidence for a splitting in the PDR response similar to the K-splitting observed in the GDR. This conclusion however, was drawn based on the consideration that the energy difference between the two peaks found is compatible with the deformation of the nucleus ground state.

Theoretical studies considering relativistic quasiparticle random phase approximation calculations based on a deformed Hatree-Fock-Bogoliubov (HFB) model suggests a predominance of K=0 strength in the lower part of the response rather than being equally distributed, while the higher-energy part of the strength shows both K=0 and K=1 components [13]. Additionally these calculations predict an isovector and isoscalar response where the isospin mixed character of these states show a suppressed response in the isoscalar channel at high energies, similar to that observed in spherical nuclei.

This thesis sets out to investigate the isoscalar PDR response in deformed nuclei for the first time. Comparative experiments were performed at iThemba LABS in South Africa, on the spherical $^{144}$Sm and prolate deformed $^{154}$Sm using the $(\alpha, \alpha'\gamma)$ reaction channel. $^{144}$Sm and $^{154}$Sm occur on opposing extremes in the chain of isotopes that undergo a transition in shape-phase from vibrators to rotors, characterized by a soft potential in the beta degree of freedom [14]. These experiments were the first to couple together the K600 magnetic spectrometer in the zero-degree mode with the BaGeL (Ball of Germanium and LaBr3:Ce detectors) array.

The layout of the thesis is as follows:

Chapter 2 provides a brief review of theoretical and experimental studies dedicated to the PDR, highlighting the well established properties and open questions regarding this dipole mode. A focus is placed on details pertaining to the PDR in deformed nuclei.

Chapter 3 provides a description of the theoretical considerations necessary to interpret the reactions investigated in this thesis. The cross sections based on theoretical models are shown.

In Chapter 4, the reader is introduced to the experimental techniques and equipment used to perform the $(\alpha\,\alpha'\gamma)$ scattering measurements at iThemba LABS.

Chapter 5 contains a descriptive detailing of the various data reduction processes used to extract the experimental cross-sections. A multipolarity assessment to confirm the E1 nature of the measured states in terms of the particle-gamma angular correlations is also shown.

In Chapter 6, the cross-section results obtained from the experiment for the isoscalar component of the PDR in the two Sm isotopes is presented. The results are discussed in comparison with the theoretical predictions shown in Chapter 3, as well as in comparison to data obtained from other studies which utilised complementary probes to investigate the PDR region of these Sm isotopes.

The thesis draws to a close in Chapter 7, where conclusions from the present study and future plans are discussed.

# Chapter 2

# Review of the PDR

A large effort toward studying the PDR both experimentally and theoretically has taken place since the first signature of this low lying dipole strength was observed. From the theoretical perspective, the PDR has been investigated using both macroscopic models and microscopic model representations. The review papers of Refs [15, 16] give a comprehensive description of the various models that have been used, including describing their successes, shortcomings and limitations. Experimentally, the PDR has been studied within several mass regions of the nuclear chart. A predominant portion of these studies probed the PDR region using the $(\gamma, \gamma')$ reaction channel, however the multi-messenger approach utilizing complimentary probes became well established in the last decade. An extensive review of the experimental effort towards studying the PDR is given in refs. [17, 18]. In this chapter, the main properties of the PDR inferred from the reviews are highlighted, while particular attention is given to the PDR in deformed nuclei.

## 2.1 Macroscopic description

One of the first macroscopic interpretations by Mohan et al. [1], modelled the PDR states within a hydrodynamic approach similar to the Steinwedel and Jensen [19] model that showed success in interpreting the GDR for heavy mass nuclei. In these models, the nucleus is described as a liquid drop consisting of compressible proton and neutron fluids which can undergo collective density fluctuations about their equilibrium density. For oscillations where the protons and neutrons move in phase, the mode is described as isoscalar (IS),

whilst for out-of-phase motion the mode is called isovector (IV). The oscillatory motion can be described by considering the effect of bulk properties such as polarisation, pressure and flow velocity, with the condition imposed that the total density should remain constant within the nuclear radius.

In the case of the IVGDR, the result is a compressional density oscillation of the proton fluid against the neutron fluid. For describing the PDR, a 3-fluid model was first considered which described the protons, neutrons occupying the same orbitals in a core and excess neutrons each as individual compressible fluids. In this model, two independent dipole modes arise, which for the case of $^{208}$Pb results in a dipole resonance at 13.3 MeV and one at 4.4 MeV. These coincide with the GDR and PDR regions respectively. In order to reduce the complexities of describing the restoring force when considering 3 fluids, instead another 2 fluid model was suggested which treated the combination of protons and neutrons occupying the same levels as a core fluid oscillating out-of-phase with a fluid of excess neutrons. This has been the most commonly used for describing the PDR from a macroscopic viewpoint.

A similar macroscopic model by Bastrukov et al. [20], model the PDR excitation as an elastodynamic excitation whereby the nucleus, considered to be a sphere containing an elastic continuous medium consists of a core with uniformly distributed nuclear and electric charge densities surrounded by a layer. The PDR excitation in this case arises from the oscillation of the layer against the core which is induced by the elastic restoring force. The total electromagnetic strength, estimated from the squared dipole moment of the charge-current density, as well as the estimated energy for the dipole mode showed fairly reasonable agreement with experimental data. However the nature of the dipole mode being only of isoscalar character is inherently implied with this model.

## 2.2 Microscopic description

While macroscopic models give physical insight into the gross features and bulk properties of the various nuclear excitation modes, a much more accurate and in-depth understanding of these phenomena can be obtained when considering how the microscopic nature

of the nucleus gives rise to these behaviours. These models are based on the mean field and energy-density functional theories and have been able to successfully predict important characteristics of the giant resonances such as their energy, strength and the damping mechanisms responsible for their measured widths. They have also been successful at reproducing the low-lying PDR strength and its increase in relation to increasing the neutron excess.

Examples of microscopic models which have been able to successfully reproduce the PDR strength include the Hartree-Fock-Bogoliubov (HFB) approach with Skyrme or Gogny effective nuclear interactions in spherical and closed shell nuclei, the HFB plus Quasi-particle RPA (QRPA) in open shell spherical and deformed nuclei, relativistic mean-field models like relativistic RPA and Quasi-particle RPA. Figure 2.1 shows predictions of the isovector and isoscalar dipole strength distributions obtained for the electromagnetic and isoscalar responses in several isotopes of Ca, Ni, Zr and Sn from ref [18]. These calculations were obtained using a discrete self-consistent Hartree-Fock plus RPA code with an SGII skyrme interaction [21]. This figure highlights the development of the low lying PDR strength with increasing neutron number in both the isoscalar and isovector channels for nuclei spanning different mass regions.

The main principle behind these models is to construct a self consistent mean field describing the potential generated by all the nucleons in a nucleus to form a basis for the ground state wave equations. Excitations can then be built up from elementary 1p-1h (or quasi particle) configurations which correspond to as an example, the promotion of a particle above the fermi surface leaving a resulting hole in the level below. From the residual interaction, state mixing of all p-h configurations occurs. States of the same angular momentum which add coherently, give rise to a collective state. In some models, coupling to more complex configurations like 2p-2h, 3p-3h are included which reproduce certain features observed in experiments better.

Other theoretical approaches based on the particle-vibration coupling model take into account the strong coupling of nucleons to nuclear surface oscillations associated with the collective excitation. In the quasi particle-phonon model (QPM), phonons are constructed

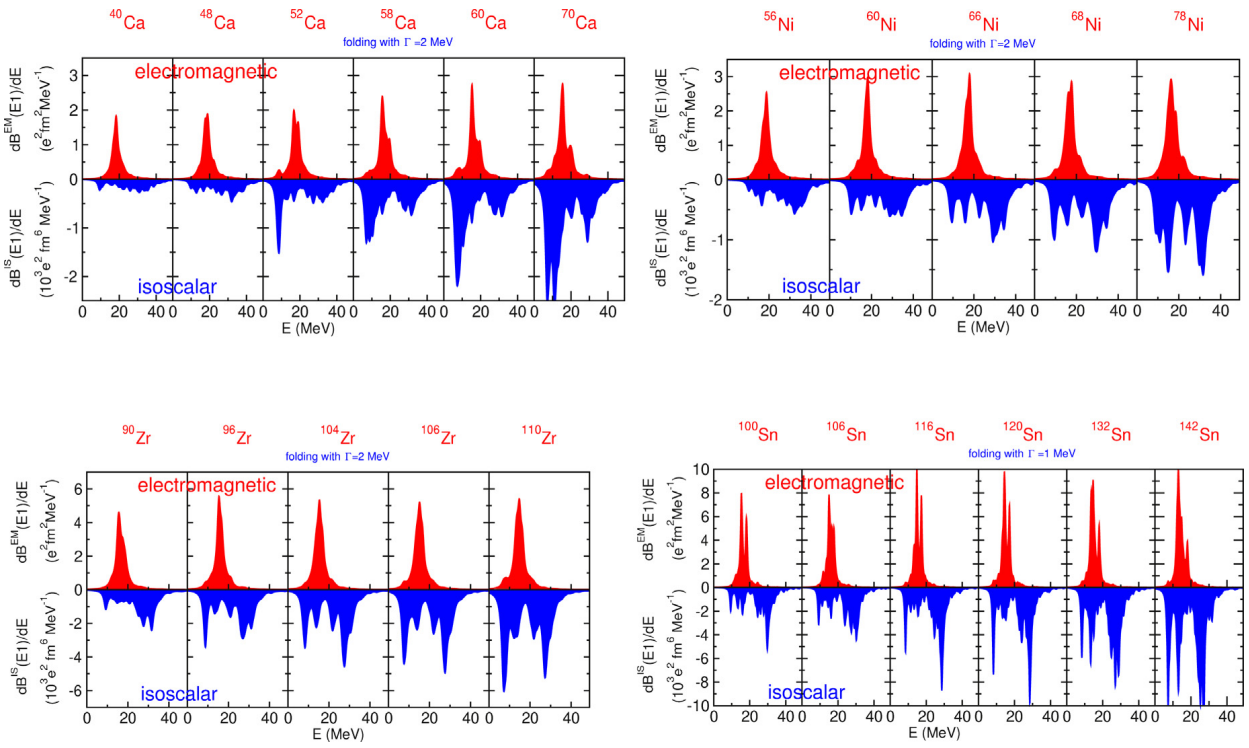


Figure 2.1: The isovector and isoscalar dipole strength distribution obtained from HF plus QRPA with SGII interaction model calculations [21] for isotopes of Ca, Ni, Zr and Sn as presented in ref.[18]. The results are smoothed using a Lorentzian of width 1-2 MeV. The electromagnetic responses are shown in the upper panels in red and the isoscalar responses are shown in blue.

from the solutions of the QRPA and the coupling to up to three phonons are included. In the Relativistic Quasi-particle Time-Blocking Approximations (RQTBA), the quasi particle-phonon coupling is also taken into account. These models have been the most successful at reproducing the fragmentation of the low lying dipole states observed in experiments due to their inclusion of 1 phonon states coupling to higher configurations.

The effect of including higher order couplings to QPM predictions, calculated in ref [22] for $^{136}$Xe, is shown in Fig.2.2. The results show more fragmentation when the coupling with up to two-phonon (middle panel), and up to three-phonon (bottom panel) configurations are included. Although the centroid shifts to lower energies, the overall strength summed over the fragmented region is almost unchanged.

One of the main features which define the microscopic interpretation of the PDR, arise from observing the shape and relative displacement of the proton and neutron transition

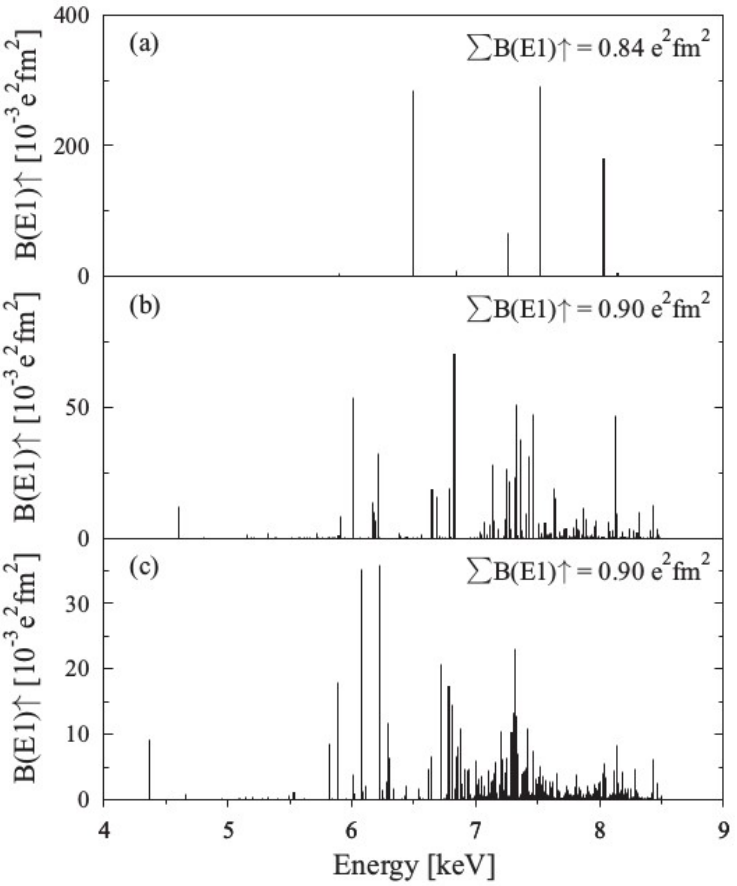


Figure 2.2: QPM calculations of the reduced transition probabilities B(E1) for $^{136}$Xe comparing different phonon coupling configurations taken from ref.[22]. Panel (a) shows the results for when only one-phonon states are taken into account, (b) when coupling up to two-phonons are included and (c) when coupling up to three-phonons are included.

densities, which significantly differ from those of the IVGDR and ISGDR. The transition densities are fundamental in describing the excitation process for a given state. For states in the IVGDR, the proton and neutron transition densities are out of phase, resulting in an almost pure isovector mode that is in agreement with the macroscopic picture predicted for this mode. For states in the ISGDR, the proton and neutron transition densities are in phase both inside the nucleus and at the nuclear surface, resulting in an isoscalar mode which reflects the behaviour of a bulk compressional mode. In the case of the PDR state however, the proton and neutron transition densities are in phase on the inside of the nucleus whilst at the surface, neutrons provide the predominant contribution. This results in a very

mixed isospin character, where the isoscalar and isovector transition densities resemble the same shape and strength at the surface.

An example of these features is shown in Fig.2.3 for the the dipole response in $^{68}$Ni. The transition densities were calculated in ref [16] using a HF+RPA with a SGII Skyrme interaction [23, 24]. The strength functions were calculated using a convolution of the corresponding reduced transition probability with a Lorenzian of 1 MeV width. In the left part of the figure, the isoscalar and isovector strength functions for $^{68}$Ni are shown, with the three regions corresponding to the PDR, IVGDR and ISGDR modes highlighted. On the right part of the figure, the transition densities calculated for three states belonging to each of the highlighted modes is shown. The upper panels (a-c) show the proton and neutron transition densities while the resulting isoscalar and isovector transition densities are shown on the bottom panels (d-f). The transition densities for states from the IVGDR and ISGDR regions clearly show distinct isovector and isoscalar behaviour respectively. The state for the PDR region however shows isospin mixed behaviour. While the various model calculations differ in certain aspects like the strength distribution, fragmentation or collectivity of the PDR, they all predict this same characteristic shape of the transition densities for this low lying dipole mode.

## 2.3 Experimental studies of the PDR

On the experimental front, first experiments for investigating the PDR utilized the photon scattering method of Nuclear Resonance Fluorescence (NRF) to great effect and make up the bulk of available PDR data spanning nuclei over the whole mass region. The mixed isospin nature of the states enabled the use of both electromagnetic and hadronic probes to investigate these states. Experiments utilizing $\alpha$ probes in coincidence with $\gamma$ decay later showcased an unexpected result regarding the isospin characteristics of the PDR. This sparked the necessity to use complimentary probes in further investigations and the multi-messenger approach came to be. Comparative investigations with further hadronic probes like protons and $^{17}$O were soon performed. An extensive review of the experimental effort

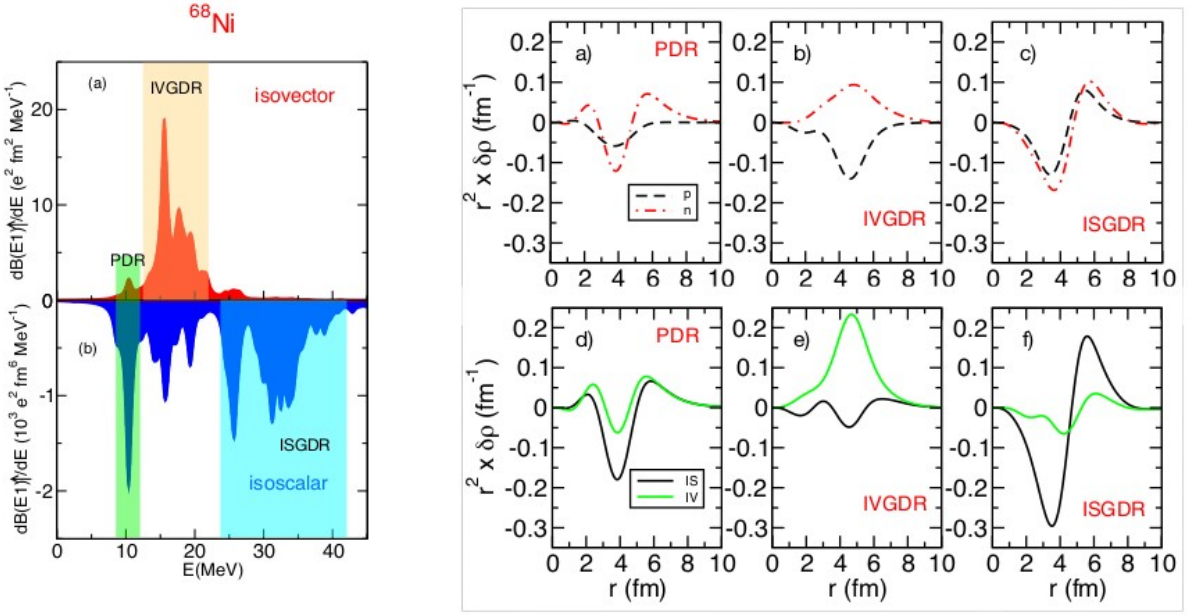


Figure 2.3: Results of the dipole response obtained in a HF+RPA calculation with a SGII interaction for the $^{68}$Ni nucleus. In the left part, the isovector (top frame) and isoscalar (bottom frame) (multiplied by $-1$) strength functions calculated by convoluting the corresponding reduced transition probability with a Lorenzian of 1 MeV width are shown. The regions for the PDR, IVGDR and ISGDR excitation modes is indicated. In the left part, the proton and neutron transition densities (upper frames) and isoscalar and isovector transition densities (lower frames) are shown, for the dipole states at energies 10.8 MeV (PDR), 15.6 MeV (IVGDR) and 31.6 MeV (ISGDR). Images adapted from [16].

towards studying the PDR is given in refs. [17, 18]. For the purpose of this thesis, the main properties of the PDR established from these studies are summarised below.

Thus far, the PDR has been identified as a collection of dipole states lying at an energy well below the IVGDR, exhausting a small percent of the Energy Weighted Sum Rule. They can be found in both stable and unstable nuclei containing a neutron excess at energies surrounding the neutron emission threshold. They can be excited by both isoscalar and isovector probes due to their strong isospin mixed behavior. Below the neutron separation energy, the PDR states are separated in two parts, a low energy component of dipole states which are excited by both electromagnetic and nuclear probes and a higher energy component populated only by the isovector interaction. This characteristic, referred to as PDR

(or isospin) splitting has been observed in all nuclei investigated using the multimessenger approach. There are still uncertainties regarding the interplay between the isoscalar and isovector responses, especially in the region above the neutron separation threshold where an entangling with the IVGDR tail contributes.

In earlier studies of the PDR, it was assumed that these dipole states predominantly de-excited via direct decay to the ground state. However, recent studies conducted with the High Intensity $\gamma$-ray Source (HI$\gamma$S) at the Duke Free Electron Laser Laboratory at Duke University revealed that these assumptions may not hold true. In these experiments, high intensity quasi-monoenergetic photon beams obtained using Laser Compton Backscattering (LCB) are used to excite dipole states. With the LCB method, low-energy laser photons are Compton scattered off electrons accelerated to ultra-relativistic energies within storage rings, thereby producing fully polarised photon beams with an energy spread of 3-5%.

The coincident $\gamma$-decays are then measured using the high-resolution and high-efficiency $\gamma^3$ setup. The photo-absorption cross section is indirectly measured from the contribution of transitions depopulating the excited state by direct decays as well as by cascade decays via the first low-lying states. The strength for transitions that decay via high-lying states can not be detected although statistical calculations predict that these account for a small percentage of the total cross-section.

The photoabsorption cross-sections obtained with HI$\gamma$S experiments on Te isotopes [25] are shown in Fig. 2.4. The two top panels show the contribution to the total elastic cross section derived from unresolved transitions. This fraction is related to the fragmentation of the E1 strength where coupling to complex configurations becomes more relevant. In general, an increasing trend with the excitation energy is found. Furthermore, the contribution from cascade decays also increases with excitation energy, as seen in the lower panels of Fig. 2.4. The higher energy states in the PDR region appear to have a more complex nature and as a result, the branching ratio to the ground state appears to be decreasing in favour of higher lying "doorway states".

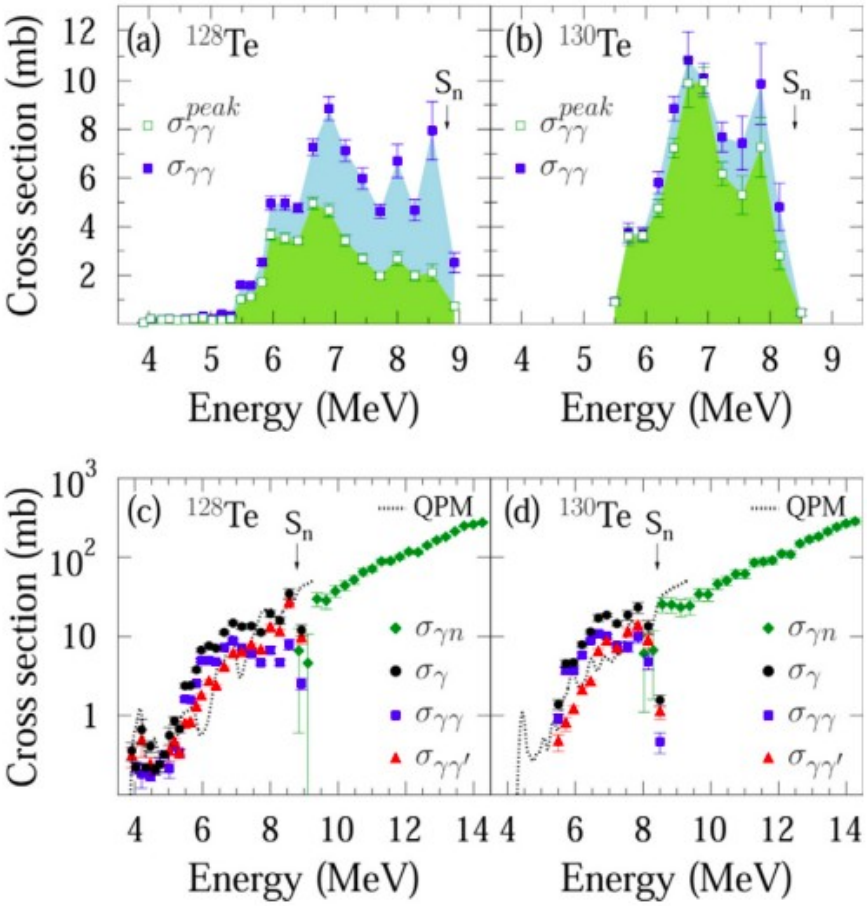


Figure 2.4: Average cross sections measured in $^{128}$Te and $^{130}$Te with quasi-monochromatic photons. Panels (a) and (b) depict the total elastic cross section (blue squares) highlighting the contribution of the strength in peaks with green open squares. Panels (c) and (d) shows the photoabsorption cross sections dividing the contributions into total elastic (blue squares), inelastic (red triangles) component. The total cross section below particle emission threshold is shown with black circles and the one obtained from $(\gamma, n)$ measurement is shown with green diamonds. Images obtained from [25].

## 2.4 The PDR with deformation

Experimental studies of the PDR in strongly deformed nuclei are only recently starting to be performed and a clear picture of the role that deformation plays on this low lying dipole

mode is yet to be established. In the IVGDR, a splitting of the response into a double-humped structure is observed for most deformed nuclei. The splitting has been linked to the different frequencies of the longitudinal (K = 0) and transversal (K = 1) vibrations with respect to the symmetry axis.

The response of the deformed nucleus $^{76}$Se above 4 MeV was studied using a quasi-monochromatic gamma beam at the HI$\gamma\gamma$S facility [26]. The E1 strength obtained did not show any clear evidence of a splitting distribution in this nucleus. However, from the theoretical interpretations obtained using a Time Dependent Hartree Fock (TDHF) model, the picture of the PDR as the isospin saturated core vibrating against the neutron skin, was not validated. This is likely to be related to the lack of neutron excess in this nucleus. A strong remark was made by the authors highlighting the importance to account for the contribution of the branching to low lying excited states in the estimation of the total dipole strength.

In another study, the summed B(E1) measured between 6 and 8 MeV for the Xe and Mo isotopic chains [27] was measured by trying to correlate the strength with the neutron excess ratios and the quadrupole deformation parameter $\beta_2$. The general trend observed is an increase of the strength with $N/Z$ ratio for both Mo and Xe isotopes while a decrease with deformation is seen in the Xe chain. Overall in this study it appeared that the deformation did not have any considerable effect on the total strength found in these neutron-rich nuclei.

A different method that can be used to identify the K-quantum number associated with a transition is to use the predictions of the Alaga rules [28] for which the decay branching ratios of excited states to the ground state band depends on the K-quantum numbers of the excited states

$$Ratio = \frac{B(E1; 1^- \longrightarrow 2_1^+)}{B(E1; 1^- \longrightarrow 0_1^+)} = \begin{cases} 0.5 for K=1 \\ \\ 2.0 for K=0 \end{cases} \tag{2.1}$$

Although this rule has proved to be useful for low-energy states, it still has to be determine whether it holds at higher excitation regions. It may provide a plausible way in which to deduce information on the K-spitting. Measuring the ratio between the branching to the ground state and to the first excited state for the pygmy states is challenging due to the close proximity of the first $2^+$ state to the ground state for strongly deformed nuclei. For

instance, in the case of studying the PDR in $^{164}$Dy [29], it was difficult to distinguish the decay to the ground state from the decay to the $2_1^+$ state due to their close energies. Thus, an estimation of the branching ratio was obtained using the mean azimuthal asymmetries of the transitions. The PDR region showed a reduction from the expected value, indicating a mixing between the decays to the $2_1^+$ state and the ground state. This suggests that no evidence for a splitting of the PDR built on the ground-state band was visible in $^{164}$Dy.

Another rare-earth nucleus, $^{156}$Gd [30], also showed similar results. Even though some attempts were made to gain information on deformation in the PDR, the results extracted from these experiments are unfortunately inconclusive regarding the role that deformation plays. These studies emphasize the need for a smaller energy spread of the photon beam to achieve a clean separation of the decays to the ground state and the first excited state. A future LCB facility under construction in Romania, the Extreme Light Infrastructure-Nuclear Physics (ELI-NP) is anticipated to provide extremely intense monoenergetic photon beams where an energy spread of less than 1% is possible.

# Chapter 3

# Theoretical considerations

In this Chapter, the theoretical considerations necessary to interpret the reactions investigated in this thesis are presented. The cross sections calculated for $^{144}$Sm and $^{154}$Sm based on theoretical models are shown. In addition, calculations for the $\alpha - \gamma$ angular correlation resulting from the inelastic scattering reaction is presented. The angular correlation pattern is required for extracting the experimental cross-section and for assessing the multipolarities of the extracted states.

## 3.1 Cross-section calculations

The use of methods such as the Distorted Wave Born Approximation (DWBA) or Coupled-channels (CC) in the description of nuclear scattering is well established in direct reaction theory [31]. In conjunction with these full quantal calculations, the use of semiclassical approximations provide a nice way to calculate the cross-sections for inelastic $\alpha$ scattering as it allows for a description of the nuclear reaction process where the most important ingredients can be easily identified. The model makes the assumption that colliding nuclei move along a classical trajectory defined by the real part of the optical potential, whilst the internal degrees of freedom are described quantum mechanically. The excitation of one of the partners of the collision is then due to the mean field of the other. The following descriptions for the semiclassical model calculations are summarised from [16].

For the inelastic scattering of a pair of nuclei a and A, considering only target excitations, the Hamiltonian can be written as

$$H_A = H_A^0 + W(t), \tag{3.1}$$

where $H_A^0$ is the internal hamiltonian of the target and the external field $W$ describes the excitation of nucleus A due to the mean field $U_a$ of nucleus a, whose matrix elements depend on time through the relative co-ordinate $\mathbf{R}(t)$:

$$W(t) = \sum_{ij} \langle i|U_a(\mathbf{R}(t))|j\rangle a_i^\dagger a_j + h.c. \tag{3.2}$$

The sums over the single particle states, denoted by i and j , run over both the particle and hole states. By solving the Schrodinger equation in the space spanned by the eigenstates of the internal Hamiltonian $|\Phi_\alpha\rangle$, the final population for each of the states can be calculated non-perturbatively. The time-dependent state, $|\Psi(t)\rangle$, of the target nucleus can be expressed as

$$|\Psi(t)\rangle = \sum_\alpha X_\alpha(t) e^{-iE_\alpha t} |\Phi_\alpha\rangle, \tag{3.3}$$

where the ground state is included in the sum as the term $\alpha = 0$. By substituting $|\Psi(t)\rangle$ in the Schrodinger equation, coupled-channel equations for the amplitude $X_\alpha$(t) is obtained.

$$\dot{X}_\alpha(t) = -\sum \alpha' e^{i(E_\alpha - E_{\alpha'})t} \langle \Phi_\alpha|W(t)|\Phi_{\alpha'}\rangle X_{\alpha'}(t) \tag{3.4}$$

These semiclassical coupled channel equations are equivalent to the Schrodinger equation and their solution for each excited state $\alpha$ gives the amplitudes $X_\alpha(b,t)$. The dependence on the impact parameter b arises due to the fact that the classical trajectories have to be solved for each impact parameter. From their solutions, the probability of exciting the internal state $|\Phi_{\alpha'}\rangle$ can be constructed as

$$P_\alpha(b) = |X_\alpha(t = +\infty)|^2 \tag{3.5}$$

for each impact parameter b. Finally, by integrating $P_\alpha$ over the range of impact parameters corresponding to the experimental scattering angle range, the total cross section is obtained.

$$\sigma_\alpha = 2\pi \int_{b_m in}^{b_m ax} P_\alpha(b) T(b) b db \tag{3.6}$$

The transmission coefficient $T(b)$ takes into account processes not explicitly included in the model space which take flux away from the elastic channel. It is usually taken as a depletion factor that falls to zero as the overlap between the two nuclei increases. A standard practice is to construct it from an integral along the classical trajectory as

$$T(b) = exp\left\{-\frac{2}{\hbar}\int_{-\infty}^{+\infty} V_I(R(t'))dt'\right\}, \tag{3.7}$$

where $V_I$ is the imaginary part of the optical potential associated to the studied reaction. When the imaginary part is not available from the experimental data, it is assumed as half the magnitude of the real part.

The range of impact parameters over which the $P_\alpha$ is integrated is determined from the deflection function for the reaction system as measured in the experiment. For these studies, this was done for $\alpha$+$^{144}$Sm at $E_\alpha = 120MeV$ and $\alpha$+$^{154}$Sm at $E_\alpha = 120MeV$, and the solid opening angle of $0 - 2^\circ$ was considered. The deflections functions for the two reactions are shown in the Fig.3.1 and Fig.3.2.

The real part of the optical potential, which together with the Coulomb interaction determines the classical trajectory, is constructed with the double-folding procedure [32]. The same procedure has been adopted to compute the radial form factor which are the fundamental part of the transition matrix elements $\langle\Phi_\alpha|W(t)|\Phi_{\alpha'}\rangle$. They are obtained by double-folding of the transition densities obtained from microscopic model calculations performed for the two Samarium isotopes. For both folding procedures, the nucleon-nucleon interaction M3Y-Reid type[30] was used.

For $^{144}$Sm, transition densities were obtained using the Relativistic Quasiparticle Time

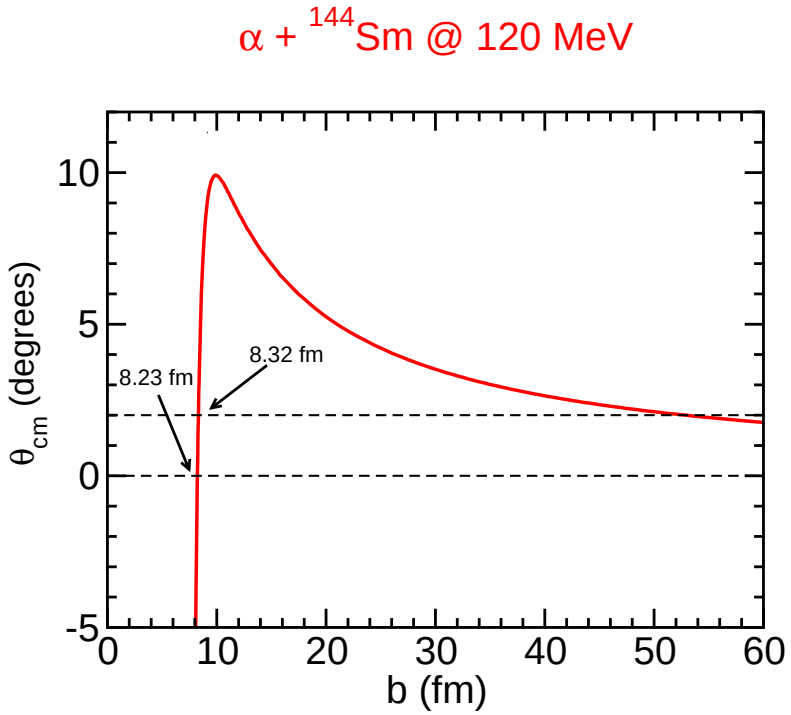


Figure 3.1: Deflection function for the system $\alpha$+$^{144}$Sm at $E_\alpha = 120$ MeV. The horizontal lines indicate the experimental $\alpha$-scattering angle range.

Blocking Approximation (RQTBA) [33], while for $^{154}$Sm, transition densities were obtained using a deformed Hartree-Fock Bogoliobov coupled to quasiparticle random-phase approximation (HFB+QRPA)[13]. The results for the cross-sections are shown in Chapter 6, where they are compared to the measured cross-sections investigated in this thesis.

## 3.2 Angular Correlations

In order to determine the singles cross-section from coincidence experiments, one needs to have a prediction of the angular correlation $W(\Omega_\gamma)$ between the inelastically scattered $\alpha$-particle and the coincident decaying $\gamma$-particle. The relation between the double-differential cross-section and the single $\alpha$-scattering cross section is given by

$$\frac{d\sigma}{d\Omega_\alpha} = 4\pi \frac{\Gamma}{\Gamma_f} \frac{1}{W(\Omega_\gamma)} \frac{d^2\sigma}{d\Omega_\alpha d\Omega_\gamma} \tag{3.8}$$

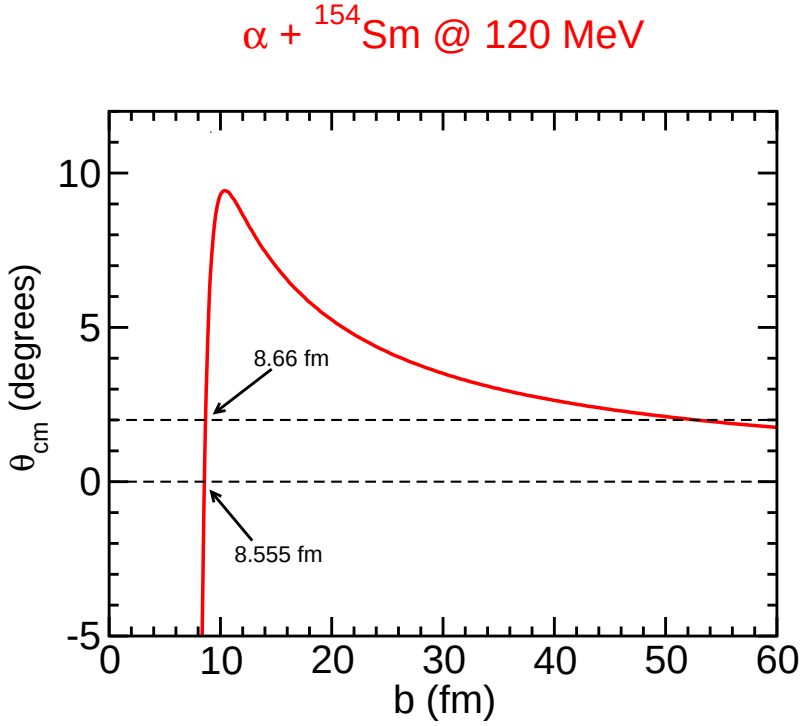


Figure 3.2: Deflection function for the system $\alpha$+$^{154}$Sm at $E_\alpha = 120$ MeV. The horizontal lines indicate the experimental $\alpha$-scattering angle range.

where the $\frac{\Gamma}{\Gamma_f}$ is the branching ratio to the final state and $W(\Omega_\gamma)$ is the $\alpha - \gamma$ angular correlation. The angular distribution of the emitted $\gamma$-rays results from the polarization of the nucleus in the nuclear reaction, which in turn depends on the scattering angle of the $\alpha$-particle. $W(\Omega_\gamma)$ is therefore also dependent on the $\alpha$ scattering angle, and is in general non-isotropic.

For the excitation of an even-even nucleus by $\alpha$-particles to a state with angular momentum J, followed by $\gamma$-decay to a $0^+$ state, the angular correlation can be calculated from the m-state population amplitudes [34] $P_m^J$

$$W(\theta,\phi) = \sum_\sigma \left| \sum_m (-1)^m P_m^J e^{-im\phi} d^J_{m\sigma}(\theta) \right|^2, \tag{3.9}$$

where $d^J_{m\sigma}(\theta)$ is a rotation matrix. The polar ($\theta$) and azimuthal ($\phi$) angles are defined

relative to the x-axis in the direction of the beam and the quantization axis perpendicular to the reaction plane. The m-state amplitudes can be obtained in DWBA by

$$P_m^J = \frac{T_{\alpha'\alpha}^{Jm}}{\sqrt{\sum_m |T_{\alpha'\alpha}^{Jm}|^2}} \approx \frac{T_{\alpha'\alpha}^{Jm}}{\sqrt{(\frac{d\sigma}{d\Sigma})_J}} \tag{3.10}$$

To calculate the angular correlation, the program code ANGCOR [35, 36] was used. In the code, one needs to define the dynamics of the reaction used to populate the state of interest, the spin and parity involved as well as the mode by which it decays. The form of the decay is calculated from the initial spin substate (m-state) distribution. For $\alpha$-$\gamma$ correlations, the calculation is done following the formulation described by Rybicki et al. [37], which follows the phase conventions of Rose and Brink [38].

To obtain the m-state distribution, the DWBA calculation using the coupled-channels code CHUCK3 [39] was used. The optical model parameters needed by CHUCK3 to describe the scattering reaction were taken using the global parameterization of Nolte [40] . CHUCK3 includes only a first-order approximation of the isoscalar form factor to describe collective excitation. In the case of dipole transitions, this corresponds to centre-of-mass motion and thus higher order terms of the form factors are needed. The form factors as defined by Harakeh and Dieperink [41] were calculated as inputs for CHUCK3 using the code FORMF available at [36].

Due to the strong dependence of the angular correlations on the solid angles of the detectors, the respective geometries have to be accounted for. In the case of the HPGe detectors, ANGCOR directly incorporates this factor as calculated from the geometrical attenuation coefficients specified in the input which were determined according to the descriptions in ref. [42]. The solid angle of the K600 was then accounted for by averaging the angular distributions obtained from ANGCOR over the K600 angular acceptance of $\pm 2^\circ$.

The procedure summarised above and the necessary input files for each step is described in full detail in [43]. The final averaged angular correlations obtained for $^{144}$Sm, $^{154}$Sm, $^{24}$Mg and $^{16}$O using this method are shown in Fig.3.3. The dipole, quadrupole and octapole angular correlations are shown in green, pink and blue respectively. The use of these calculated

angular correlation patterns in the extraction of the double differential cross-section and for confirming the dipole character of the PDR states under study will be revisited in Chapter 5.

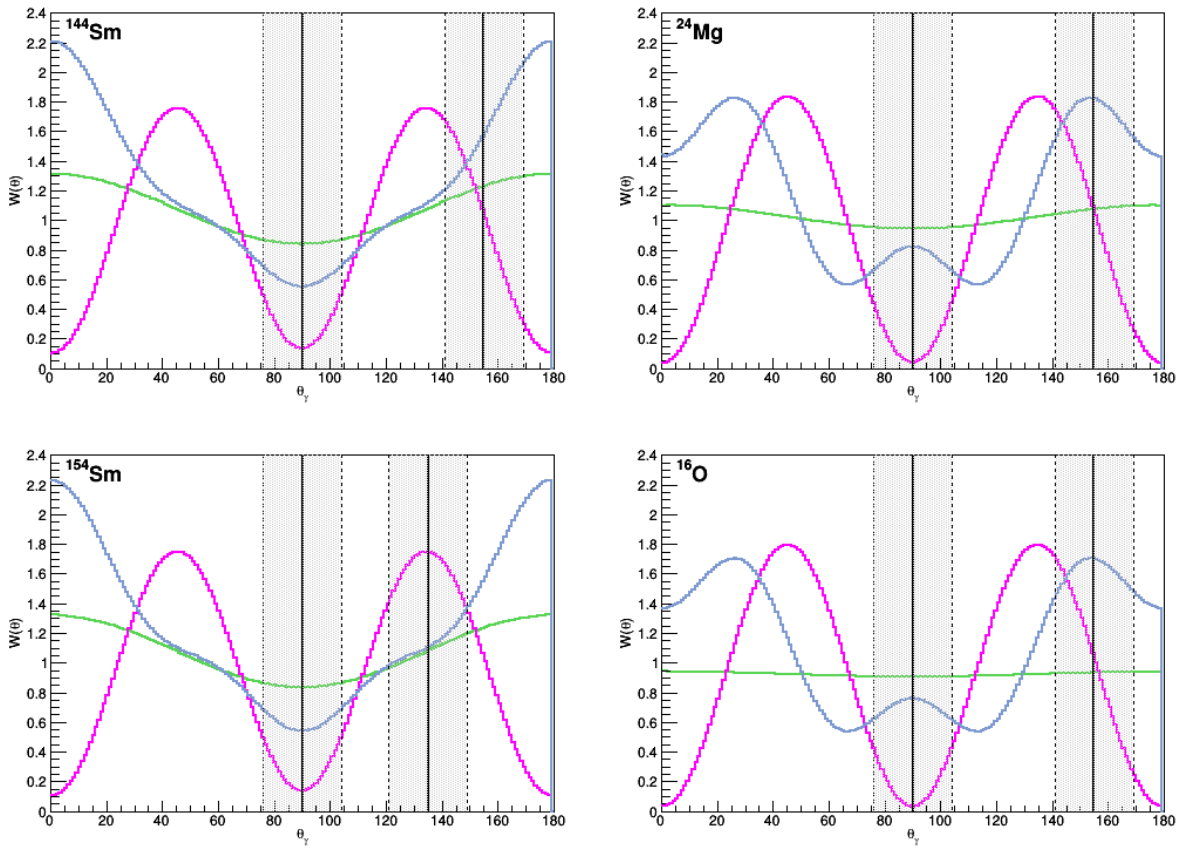


Figure 3.3: Angular correlations obtained from ANGCOR after averaging over the opening angle of the K600 spectrometer for $^{144}$Sm, $^{154}$Sm, $^{24}$Mg and $^{16}$O. Green, pink and blue correspond to dipole, quadrupole and octapole modes respectively

# Chapter 4

# Experimental Techniques and Equipment

The $(\alpha, \alpha'\gamma)$ experiments on $^{154}$Sm and $^{144}$Sm were performed at iThemba Laboratory for Accelerator Based Sciences (iThemba LABS), in South Africa over individual experimental campaigns for each isotope. In both experiments, the Seperated Sector Cyclotron (SSC) provided a beam of alpha particles accelerated between 117 and 120 MeV. The K600 magnetic spectrometer and its focal plane detection systems were used for the $\alpha$-particle detection whilst the BaGeL array (Ball of Germanium and LaBr detectors) was used for the subsequent $\gamma$-rays. In this chapter, an overview of the experimental equipment and techniques used are provided.

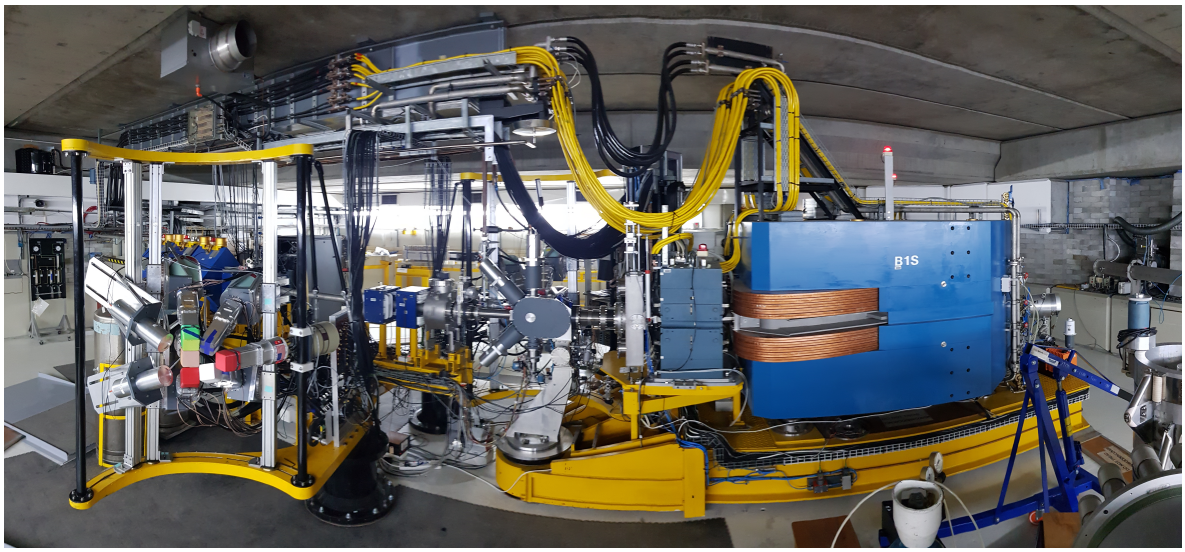


Figure 4.1: Photograph of the experimental set-up in the K600 vault at iThemba LABS

## 4.1 iThemba LABS accelerator facilities

The Separated Sector Cyclotron (SSC) is the primary accelerator at iThemba LABS used along with other ancillary facilities to conduct nuclear research. The SSC consists of four C-shaped sector magnets each with a sector angle of 34°. A layout of the accelerator infrastructure and beamlines is shown in Fig. 4.2.

The facility has two injector cyclotrons where beams are produced and pre-accelerated to sufficient energies before entering the SSC. The K=8 Light-ion Solid-Pole Injector Cyclotron 1 (SPC1) has an internal Penning Ionisation Gauge (PIG) ion source and can accelerate particles from protons to heavy ions with a mass-to-charge ration of 0.25. The K=10 Light-ion Solid-Pole Injector Cyclotron 2 (SPC2) has 3 possible external sources; a polarised ion source and two electron cyclotron resonance (ECR) ion sources. Beams from the external sources are transported to SPC2 via a transfer beamline and axially injected using a spiral reflector. The accelerated beams from both SPC1 and SPC2 are extracted using an Electrostatic Extraction Channel (EEC) and two magnetic extraction Channels (MEC1 and MEC2). The ECR source and SPC2 were used for the experiments conducted for this thesis.

After extraction from SPC2 and further acceleration in the SSC, a pulsed beam with energies of 117.88 MeV and 120.6 MeV were achieved in the experiments for $^{154}$Sm and $^{144}$Sm data taking respectively. The radio-frequency(RF) of the cyclotron in each case was 33.5 MHz and 33.9 MHz, resulting in a time difference of ~30 ns between consecutive beam bunches. The beam was then guided through the high-energy beamlines (X, P and S lines) which are equipped with sets of quadrupole and dipole magnets and slits for optimisation, to the K600 Magnetic Spectrometer.

In order to optimise the energy resolution of the spectrometer, the beam was dispersion matched to the focusing conditions of the spectrometer. Due to the positioning of the 0°-beamdump, regular dispersion matching would be tedious to perform and a faint beam technique was used instead [45]. In this technique, the initial beam from the ion source is attenuated using copper meshes, resulting in a reduction of intensity by a factor of up to

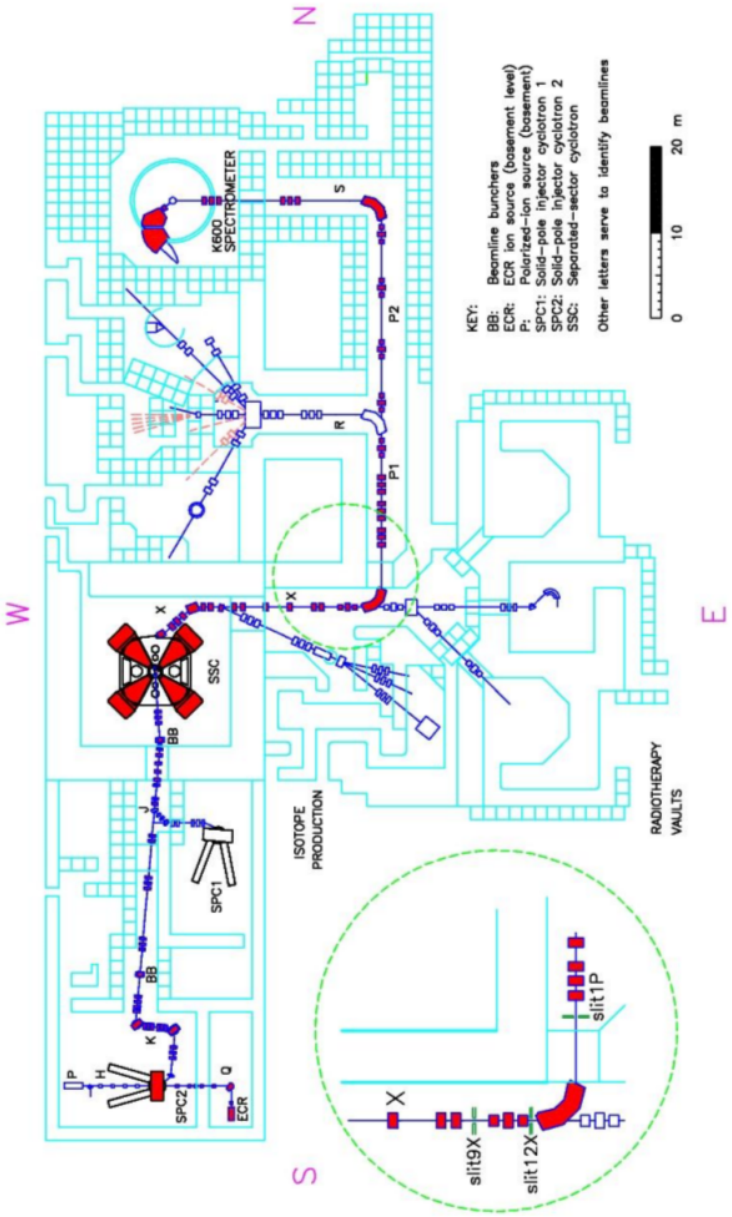


Figure 4.2: A schematic layout of the accelerator and ancillary facilities at iThemba LABS [0].

$10^6$ without affecting the profile of the beam. The magnet settings of the spectrometer are then scaled such that the beam passes through the focal plane detectors where the degree of dispersion can be assessed. The beamline elements can then be optimised in order to minimise the size of the beam image observed and thus achieve lateral dispersion matching.

## 4.2 The K600 magnetic spectrometer

The K600 Magnetic Spectrometer is a Quadrupole-Dipole-Dipole (QDD) type spectrometer that was used to detect the scattered $\alpha$-particles. Figure 4.3 shows a schematic layout of the spectrometer. A quadrupole magnet (Q) at the entrance of the spectrometer enables vertical focusing at the focal plane. The two horizontally-bending dipole magnets (D1 and D2) allow the momentum dispersion to be adjusted by varying the ratio of the two dipole magnets.

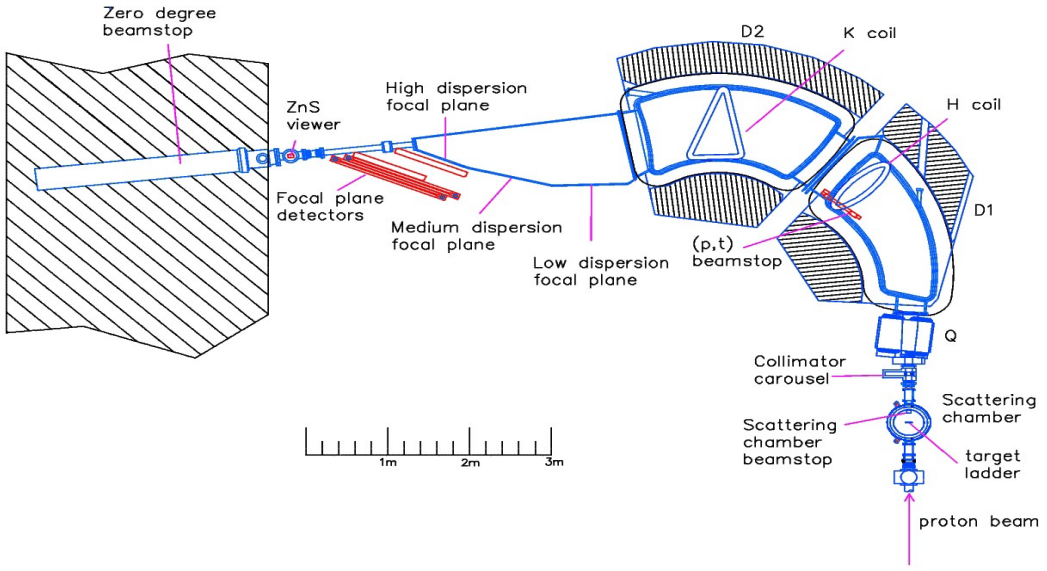


Figure 4.3: Schematic layout of the K600 magnetic spectrometer. Scattered particles enter the spectrometer via the scattering chamber and are focused by the magnets on the high dispersion focal plane where they are measured by the Focal Plane Detection System (FPDS).

Within each dipole, there is a pole-face current winding coil, the K and H trim coils respectively. The K-coil (in D2) has a dipole and quadrupole focusing component, and is used to adjust for first-order kinematic variations of momentum with the horizontal scattering angle (x|$\theta$). The H-coil (in D1) has a dipole and hexapole component, and is used to correct for second-order (x|$\theta^2$) aberrations. The terms (x|$\theta$) and (x|$\theta^2$) represent the sensitivity of the focal plane position ($x_{fp}$) to the scattering angle ($\theta_{scat}$) of the reaction products [46].

The particle beam delivered from the accelerator enters the scattering chamber which contains a target ladder capable of holding up to six targets. The inelastically scattered particles which are scattered off the target enter the spectrometer and are collimated by one of the collimators installed in front of the quadrupole magnet. The diameter of the collimator thus defines the solid angle acceptance of the spectrometer. The particles are then focused on the high dispersion focal plane of the spectrometer, where a position sensitive detector system is positioned. The unscattered beam is transported through the 0°-beamline to the 0°-beamstop embedded in the concrete wall of the experimental area.

## 4.3 The Focal Plane detector system

At the focal plane, a focal plane detector system (FPDS) is in place to determine the energy and scattering angle of the incident particles. The FPDS can accommodate for two multi-wire drift chambers and two plastic scintillation (paddle) detectors. In the experiments conducted, one vertical drift chamber (VDC) with a UX type wire configuration and a single paddle detector were used at the high dispersion focal plane.

### 4.3.1 Multiwire Drift Chamber

The UX type VDC was designed in order to provide a more accurate position discrimination particularly for 0° measurements. The chamber contains a set of wire planes; the X signal-wires positioned perpendicular to and the U signal-wires angled at 50° to the scattering plane respectively. The wire-planes are sandwiched between three cathode planes composed of 20 $\mu$m thick aluminium foil, with an 8 mm spacing between each adjacent wire and cathode plane.

The wire-planes consist of alternating signal wires and field shaping wires, spaced 4 mm apart which are composed of gold-plated tungsten. The signal-wires are 20 $\mu$m in diameter while the field shaping wires are 50 $\mu$m in diameter. In the X wire-plane, there are 199 field shaping wires and 198 signal wires. In the U wire-plane, there are 144 field shaping wires and 143 signal wires. At the ends of both wire-planes are guard wires made from Ni-Cr

(80%/20%) with a diameter of 125$\mu$m. For each wire-plane, the signal and field wires are soldered onto a circuit board.

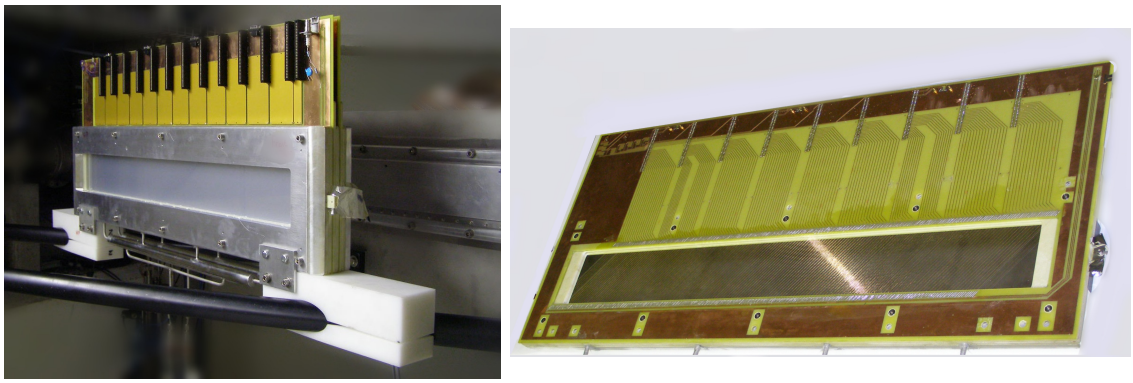

Figure 4.4: Photograph of the UX type MWDC as mounted near the focal plane (left) and the U-type wireplane (right) where the wires are inclined at 50°.

Flanking the outer cathode planes, are two Mylar planes of 25 $\mu$m thickness which isolate the inner chamber from atmosphere. The chamber is filled with a gas mixture containing Ar (90%) and $CO_2$ (10%) and sealed. A high voltage of $-$ 3.5 kV was applied to the cathode planes, while $-$ 500 V was applied to the field shaping wires.

As an $\alpha$ particle passes through the VDC, it ionizes a track along its path. Since the VDC is positioned perpendicular to the spectrometers bending plane, its trajectory will traverse several adjacent drift cells before exiting the VDC. An example of such an event is shown in figure 4.5. The free electrons produced from the ionization drift along the field lines to the closest anode wire where charge multiplication takes place and the signal is registered. The drift time between the primary point of ionization and the point where this charge cascade occurs for a given drift cell is then measured. Since the electric fields are set such that the drift velocity is constant, the corresponding drift distance can be determined [47]. A ray-tracing procedure is thus implemented in which the wire "hits" corresponding to a particular event and their relevant drift distances are determined in order to accurately gauge the intersection point and angle of the particles trajectory with the wire plane. A description of the ray-tracing procedure is given in section 5.1.2.

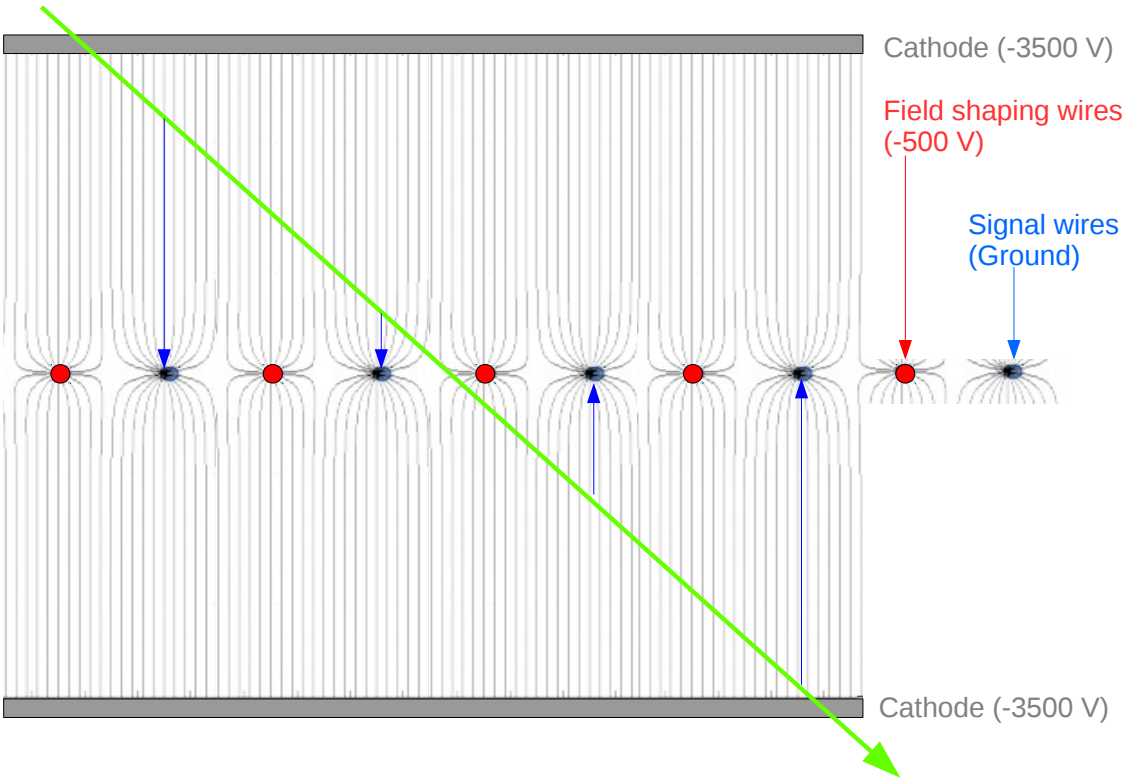


Figure 4.5: Example of the drift lines associated with a typical particle track travelling through the VDC.

### 4.3.2 Paddle detector

The paddle detector consists of a Bicron BC408 plastic scintillator ( 122 cm x 10.2 cm) connected on either ends to 90° twisted pair adiabatic lightguides which are read out by Hamamatsu R329-02 Photomultiplier tubes. The paddle detector serves primarily to provide a fast timing trigger signal for the Data Aquisition (DAQ) system and is also used for particle identification.

## 4.4 The BaGeL array

The BaGeL array (**Ba**ll of **Ge**rmanium and **L**aBr:$Ce_3$ detectors) was used to measure the $\gamma$-rays resulting from the de-excitation of the states populated by the inelastic scattering reaction. The array was designed for the first experiments ever performed at iThemba

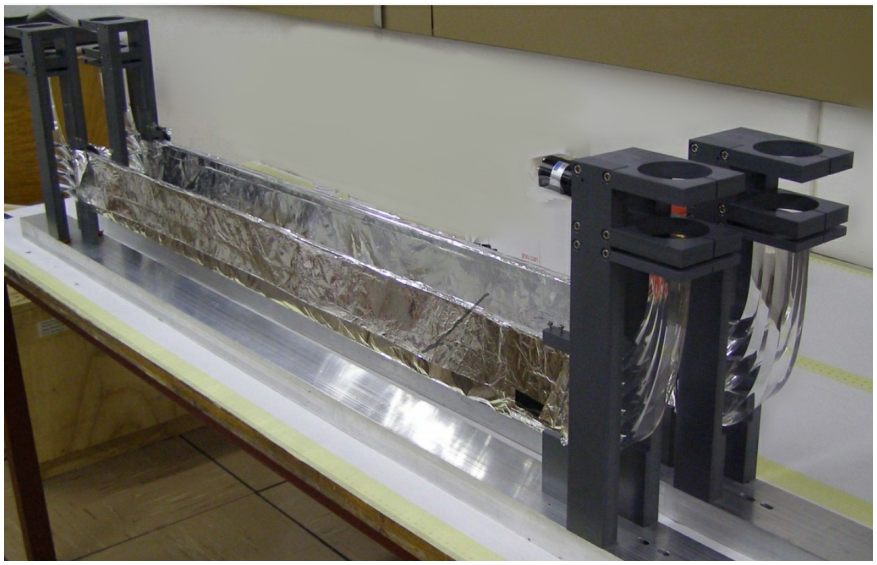

Figure 4.6: Photograph of a set of paddle detectors with the scintillators wrapped in foil. The PMT's are not mounted here.

LABS which coupled a gamma detector array with the K600 magnetic spectrometer. In the $^{154}$Sm experiments (Exp1), 8 High Purity Germanium detectors (HPGe) and 2 Large volume LaBr:$Ce_3$ detectors (borrowed from Oslo University) were used. In the $^{144}$Sm experiments (Exp2), BaGeL was comprised of 12 HPGe and 5 LaBr:$Ce_3$ detectors, obtained as part of the African LaBr:$Ce_3$ array (ALBA) project of iThemba LABS.

The detectors were mounted on an oyster-clamp type structure and positioned at backward scattering angles as close to the target chamber as possible. An oyster-clamp mounting structure was used so that the gamma detectors could be moved away from the scattering chamber during beam tuning and moved back in place during data taking without compromising their positions. This was necessary in order to prevent damage from the large amount of background induced by the beam when impinging on the viewer used for tuning. The oyster-clamp also accommodated for the cooling system of the HPGe and the required pipes and wiring in an orderly manner so that mishaps could be avoided when opening and closing the structure.

On the incident faces of the HPGe detectors, thin lead and copper absorbers were placed to shield them against low-energy $\gamma$ and X rays (~3-5 mm total shielding thickness). In Exp1,

the absorbers were taped on, whilst in Exp2, fitted covers housing the absorbers were 3-D printed to clip onto the HPGe detectors.

A photograph of BaGeL mounted around an open scattering chamber during the $^{144}$Sm experiment is shown in figure 4.7. Technical details and position information for each detector are summarised in table 4.1 and 4.2 for each experiment respectively.

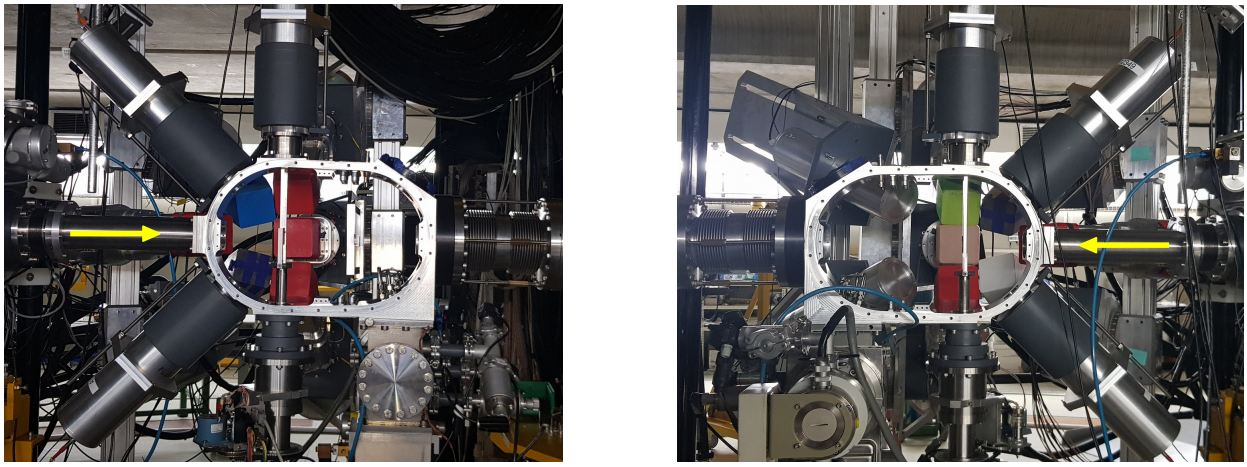

Figure 4.7: Photographs of BaGeL taken during experiments on $^{144}$Sm. The detectors positioned to the left and right of the incoming beam are shown in the left and right panels respectively. The beam direction is indicated with yellow arrows.

Table 4.1: Table summarising technical details of BaGeL for $^{154}$Sm experiments

| Detector Label | Detector Model ref. | Distance from target (cm) | $\theta$ | $\phi$ |
|---|---|---|---|---|
| L1 | Canberra 41 | 16.3 | 125.3° | 45° |
| L2 | Canberra 39 | 16.6 | 135° | 0° |
| L3 | Canberra 38 | 16.7 | 90° | 0° |
| L4 | Canberra 36 | 16.9 | 90° | 35° |
| R1 | Canberra 63 | 16.6 | 90° | 180° |
| R2 | Canberra 37 | 15.9 | 135° | 180° |
| R3 | Canberra 40 | 16.6 | 125.3° | 135° |
| R4 | Canberra 35 | 16.5 | 90° | 145° |

Table 4.2: Table summarising technical details of BaGeL for $^{144}$Sm experiments

| Detector Label | Detector Model ref. | Distance from target (cm) | $\theta$ | $\phi$ |
|---|---|---|---|---|
| L1 | Canberra 39 | 18.5 | 90° | 300° |
| L2 | Ortec 2 | 18.5 | 90° | 0° |
| L3 | Canberra 38 | 18.5 | 90° | 330° |
| L4 | Canberra 63 | 18.5 | 120° | 25° |
| L5 | Canberra 61 | 18.5 | 120° | 335° |
| L6 | Ortec 3 | 18.0 | 155° | 0° |
| R1 | Canberra 35 | 18.5 | 90° | 149° |
| R2 | Ortec 1 | 18.5 | 90° | 180° |
| R3 | Canberra 36 | 18.5 | 90° | 211° |
| R4 | Canberra 37 | 18.5 | 120° | 155° |
| R5 | Canberra 40 | 18.5 | 120° | 205° |
| R6 | Ortec 4 | 18.0 | 155° | 180° |

## 4.5 Signal Processing and DAQ

### 4.5.1 Electronics

All the electronics modules used within the experiments comply to NIM and VME standards. A schematic diagram of the electronics for the K600 FPDS is shown in Fig. 4.8. For the VDC's at the K600 focal plane, 16 channel P-TM 005 cards obtained from Technoland pre-amplify and discriminate the drift time signals from the wire-planes which were read out by CAEN V1190 Time to digital converters (TDC). The signals from the PMT's at the paddle detector were read out by CAEN V792 charge to digital converters (QDC). In addition, logic outputs from a constant fraction discriminator (CFD) were used to create the trigger signal for the DAQ.

A schematic diagram of the electronics for BaGeL is shown in Fig. 4.9 for Exp1 and Fig. 4.10 for Exp2. Each segment of the HPGe Clover detectors were connected to a charge-sensitive pre-amplifier which converts the collected charge deposited within a crystal to a voltage signal corresponding in proportionality to the deposited energy from an incident particle. Two outputs were generated from the pre-amplifier in order to record both an energy and a timing pulse. For the energy, the signal was digitized using a 32 Channel analogue to digital converter (ADC). In the first set of experiments on $^{154}$Sm, CAEN V792

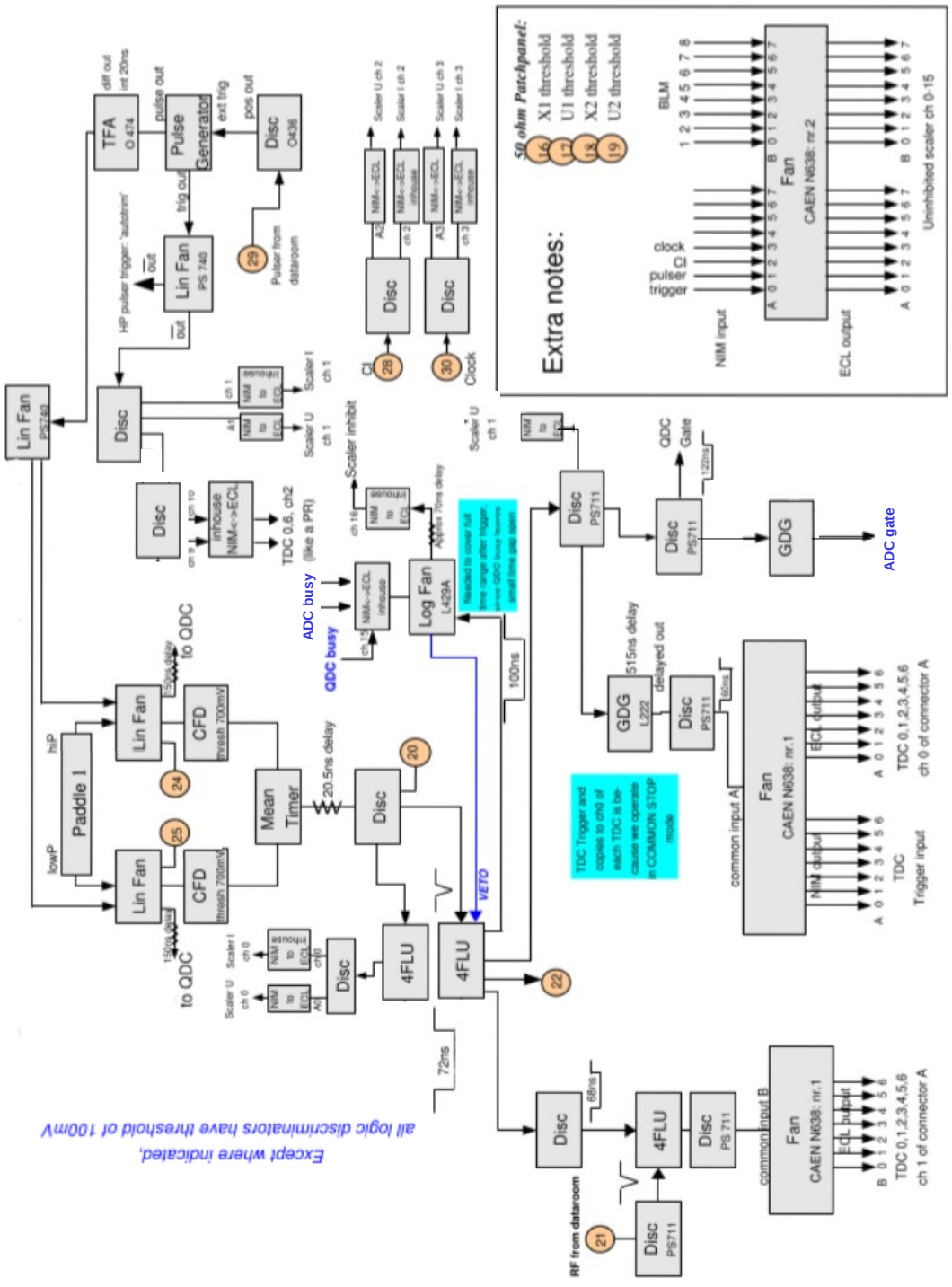


Figure 4.8: A schematic diagram of the electronics for the K600 focal plane detector system.

ADC's and CAEN V1190 TDC's were used. In the second experimental campaign ($^{144}$Sm data taking), the Mesytec MSCF-16 modules were used which have both the signal timing and voltage signal digitization capabilities.

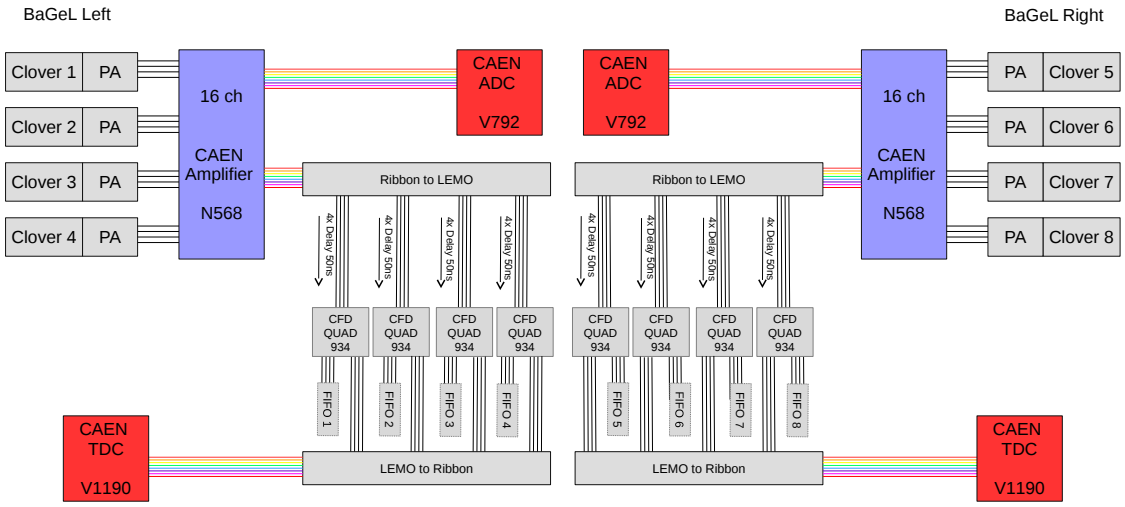


Figure 4.9: A schematic diagram of the BaGeL electronics in Exp1.

### 4.5.2 DAQ system

The K600 Data Acquisition System incorporates the Maximum Integrated Data Acquisition System (MIDAS) [48] software to process and store the data digitized by the VME electronics described above. The data is acquired on an event-by-event basis. The MIDAS software features allow for transport of data between multiple computers, thus online analysis and system monitoring are made more convenient.

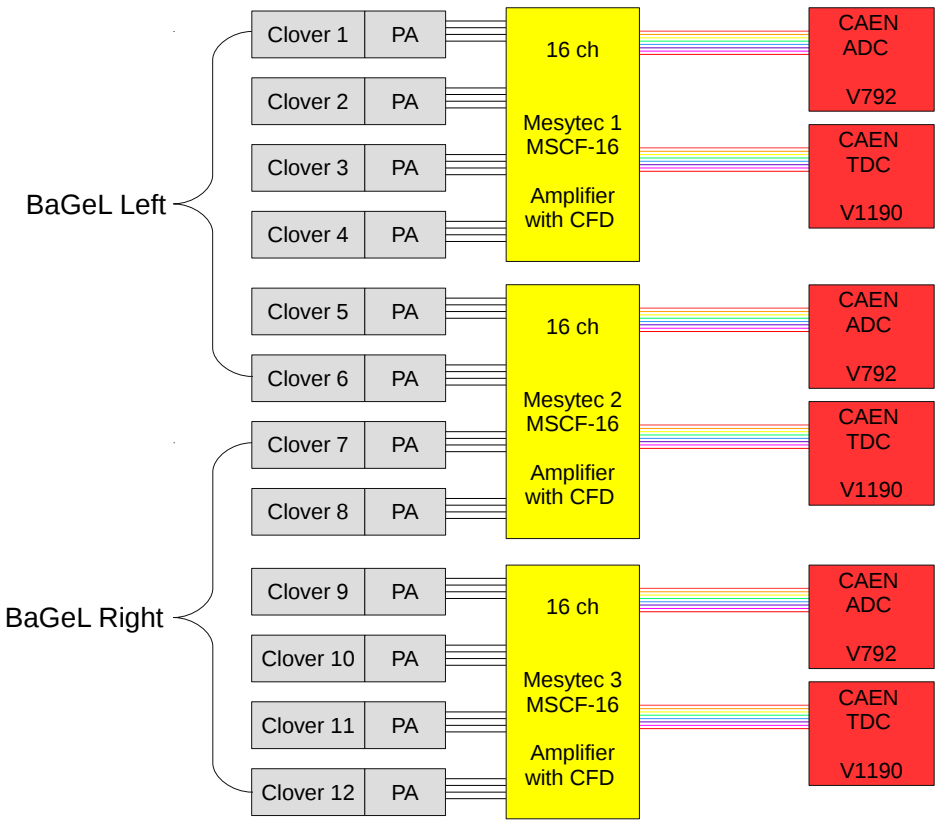


Figure 4.10: A schematic diagram of the BaGeL electronics in Exp2.

# Chapter 5

# Data Analysis

In this Chapter, the data analysis procedures for extracting the experimental cross-sections are presented. During the experiments, data was collected for runs alternating between the $^{24}$Mg calibration target with the $^{154}$Sm or $^{144}$Sm targets for each respective experiment. The raw data for each run is stored in an event-by-event format in a midas file created by the MIDAS Data Acquisition system.

These files were then analysed offline using the K600analyser C++ code [49] developed at iThemba LABS. The code translates the raw MIDAS files into ROOT [50] files, with various subroutines to treat the different variables that are then stored as "branches" within a type of relational database called a "TTree".

In the first part of the chapter, the offline analysis pertaining to the data collected from the K600 focal-plane detectors is discussed. Thereafter, the data analysis of the gamma ray decay data measured with BaGeL is presented. As in Chapter 4, the experimental period pertaining to the $^{154}$Sm data acquisition will be referred to as Exp1 whilst that pertaining to the $^{144}$Sm data acquisition will be referred to as Exp2.

## 5.1 K600 Focal-Plane Data reduction

The main components for the reduction of the focal-plane data entail:

1. Selecting the events of interest through performing particle identification.

2. Creating a look-up table which correlates the drift-distances to drift-times in the VDC

which are used to accurately determine the position that the $\alpha$-particle passes through at the focal plane.

3. Implementing a line-shaping correction to further adjust the kinematic aberrations and to improve on the resolution of the measured peaks.

4. Calibrating the position spectrum to excitation energy.

In addition to the above mentioned steps, offset corrections are implemented for variations in the particle time-of-flight (TOF), X-position, Y-position and paddle pulse height signals that occur between runs in order to ensure that a common cut selection can be implemented across all the data. Variations in the TOF occur when adjustments to the SSC RF are implemented in order to keep the beam intensity optimized over the duration of data collection. The beam intensity is affected when environmental factors like temperature changes cause the SSC magnets to drift over time.

Fluctuations in the beam energy as well as minor adjustments to the magnet settings result in slight variations to the focal plane position for a given excitation peak, while small changes in the paddle signals can be influenced by the performance of the PMT's over time. The offsets for the above mentioned variables were computed for each run of $^{24}$Mg, in which the level density between peaks is much smaller and thus distinct peaks can be identified. The offsets of the closest $^{24}$Mg runs were then matched to the corresponding Sm runs.

Figure 5.1 shows the variation in focal plane X-position with experiment entries for the chained run data set of $^{24}$Mg during the full beam period in Exp2 before and after implementing the offsets. Each bin corresponds to 100 000 entries, with the average 30 minute data run containing around 750 000 entries. The variations in 5.1a are caused by minor changes to the K600 magnetic fields when beam tuning was required in order to compensate for issues such as the beam buncher tripping, a power failure and the amplifier to the ion source tripping to name a few examples. As seen in 5.1b, applying the offsets accounts for these variations, and along with the line-shaping corrections described in section 5.1.4, vastly improves the resolution. This also ensures that a common rigidity calibration can be applied to calculate the excitation energy.

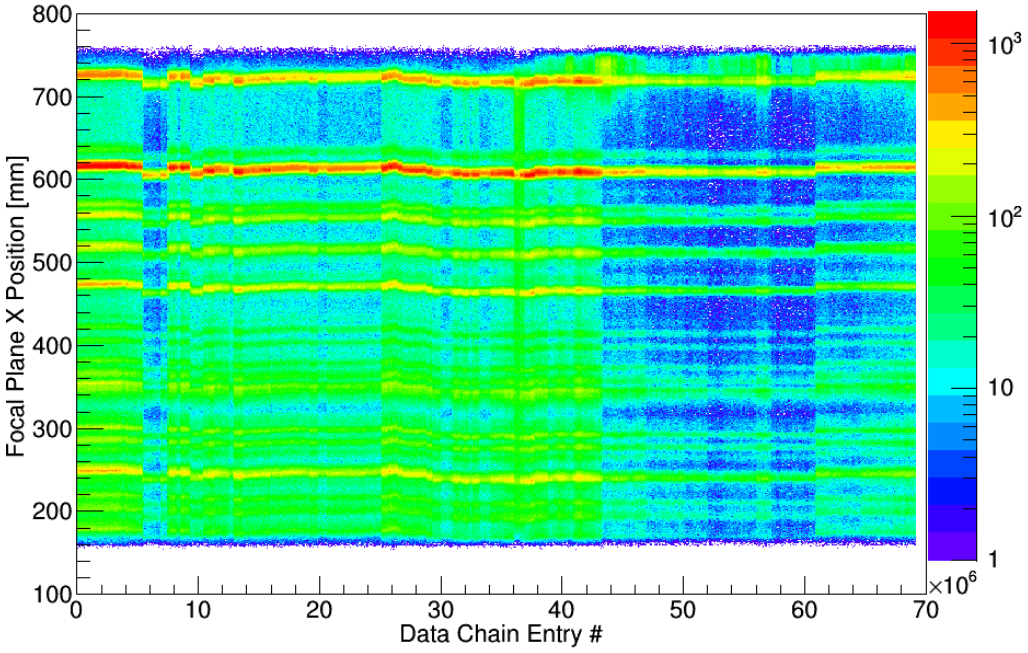


(a) Before offset implementation

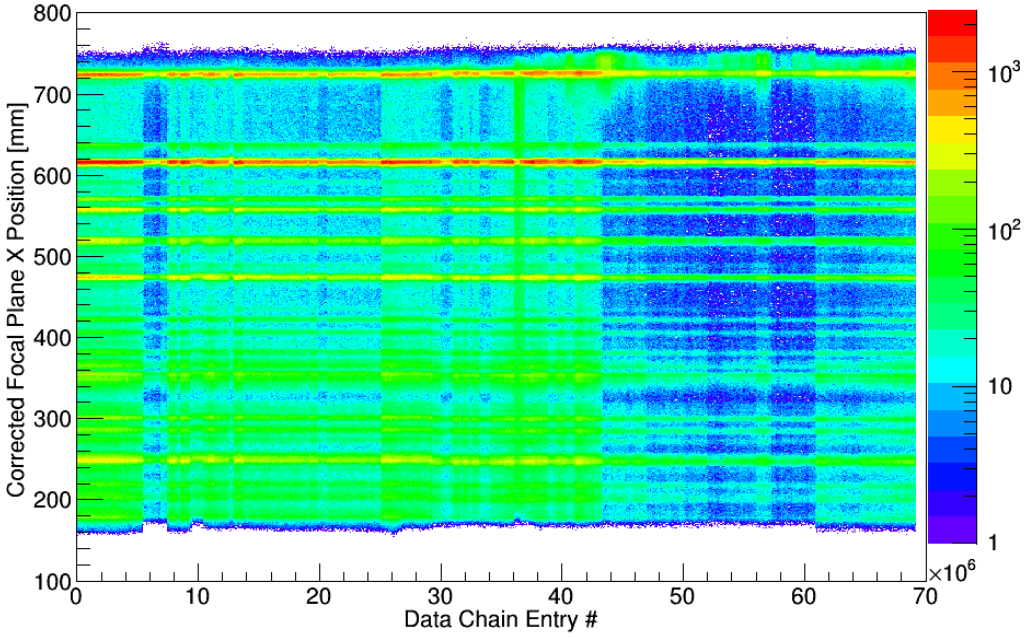


(b) After offset implementation

Figure 5.1: Variation in Focal plane X position with run entries before and after offset implementation for chained $^{24}$Mg data in Exp2.

### 5.1.1 Particle identification

The excited nucleus resulting from the nuclear reaction may decay via several decay mechanisms. In order to select only the events corresponding to the inelastically scattered $\alpha$s, particle identification is performed by assessing the interaction of the particle as it passes through the detector system.

A particle of charge $q$, mass $m$ and velocity $\vec{v}$, is subjected to a Lorent'z force exerted by the magnetic field $\vec{B}$ of the spectrometer, described in equation 5.1. The magnetic rigidity gives a measure of the "bending" effect to the particles motion as a result of this magnetic field $\vec{B}$. It is defined non-relativistically in equation 5.2, where $\rho$ is the radius of curvature of the particle through the spectrometer and $p$ is its corresponding momentum. A particle with higher momentum or smaller charge will thus have a larger resistance to being deflected by a given $B$ field.

$$\frac{d\vec{v}}{dt} = \frac{q}{\gamma m} x \vec{B} \tag{5.1}$$

$$R = B\rho = \frac{p}{q} \tag{5.2}$$

The magnetic rigidity thereby influences the position at which the particle passes through the focal plane, as well as the distance $d$ that it travels along its path from the scattering chamber to the focal plane detectors. The time-of-flight correlating to this pathway, $ToF = \frac{d}{v}$, is measured in the experiment as the relative time elapsed between a coincident paddle signal and the RF signal of the SSC. The TOF of the particle, the amount of energy it deposits in the scintillator of the paddle detector and its position at the focal plane can therefore be used to identify it.

PID spectra for the $^{24}$Mg, $^{144}$Sm and $^{154}$Sm run data, as well as empty target runs for each experiment are shown in figure 5.2.

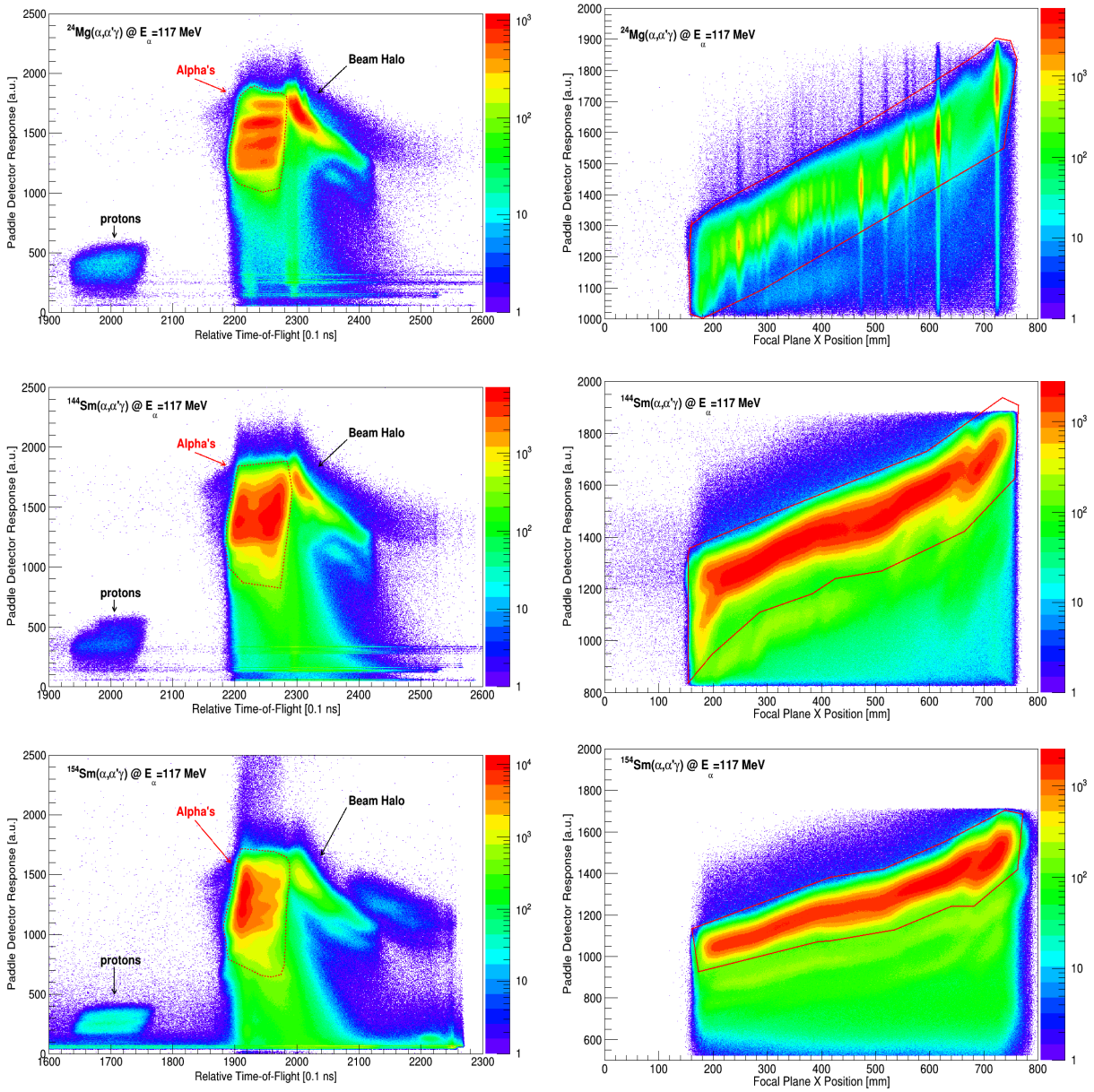


Figure 5.2: PID spectra shown for $^{24}$Mg, $^{144}$Sm and $^{154}$Sm in the top, middle and bottom panels respectively.

The left panels show the paddle detector response as a function of relative TOF from which the various particle contributions are identified.

A clear distinction between the $\alpha$ and proton loci can be observed. The beam halo sits just to the top right of the $\alpha$ region of interest. In some runs, the beam halo drifted into this

region resulting in a larger background corresponding to the low energy side of the focal plane (~650-780 mm).

The right panels show the paddle detector response as a function of the Focal-plane X-position (with the PID cut to the left already implemented). A further graphical cut is applied, as indicated by the red line, in order to further optimise the data selection.

### 5.1.2 VDC position tracking

As described in Section 4.3.1, the position at which a particle passes through the focal plane can be determined using the drift-time characteristics of the detector. The drift distance $y$, between the signal wire and the point along the particles track at which it crossed a particular drift-cell, can be calculated from:

$$y(t) = \left(\frac{dN}{dt}\right)^{-1} \int_{t_0}^{t} \frac{dN}{dt'}\, dt' \tag{5.3}$$

where $\frac{dN}{dt}$ is the spatial distribution of drift-times, $t_0$ is the time at which the particle arrives in the drift-cell, and $t$ is the time at which the pulse registers at the anode [47].

In order to obtain the characteristic distribution $\frac{dN}{dt}$, a "white spectrum" is used, whereby the focal plane is homogeneously illuminated with particles resulting in uniformly distributed particle tracks. The average timing response of each signal wire is thus measured. Since the drift-time distribution is proportional to the drift velocity $\omega(t)$, a look-up table (LUT) is generated which correlates drift-times to drift-distances using equation 5.4.

$$y(t) = \int_{t_0}^{t} \omega(t')\, dt' \propto \int_{t_0}^{t} \frac{dN}{dt'}\, dt' \tag{5.4}$$

A white-spectrum is generally obtained by adjusting the K600 magnets so that particles in the beam continuum can be used to homogeneously illuminate the focal plane. In the case of 0° measurements however, this is not as straightforward to do without causing extremely high rates in the focal plane detectors.

Instead, one can use scattered particles from the samarium targets to sufficiently illuminate the focal plane homogeneously, owing to the high level density of excited Sm states. Thus a Sm data run gated for $\alpha$ particle selection was used to generate the LUTs for each experiment.

Since the LUT generated is a global parameter that applies to a full wire plane in general, time delays that vary between the different signal wires must be accounted for before generating the LUT. These delays predominantly arise due to the varying lengths in the cables between the pre-amplifiers and the TDC module. Thus, cable length offsets are implemented such that the trailing edge of the drift time signals for each wire channel are aligned. Figure 5.3 shows the effect of implementing these cable offsets.

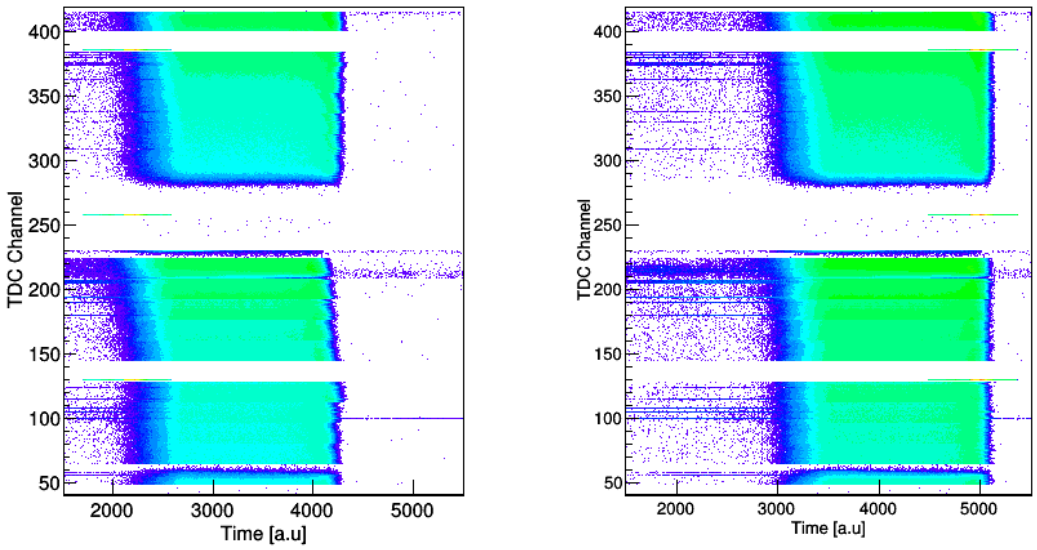


(a) Before offset implementation (b) After offset implementation

Figure 5.3: TDC reference times for the various TDC channels of the VDC wires for Exp2, showing the effect of implementing the cable offset to align the trailing edge of the drift time distributions

Figure 5.4 shows the LUT generated for the X wire-plane used in Exp2. Within the experiment, the drift times for each wire plane are measured relative to the trigger signal received from the paddle detector. Hence, in the LUT, the shorter drift time correlates to a longer drift distance.

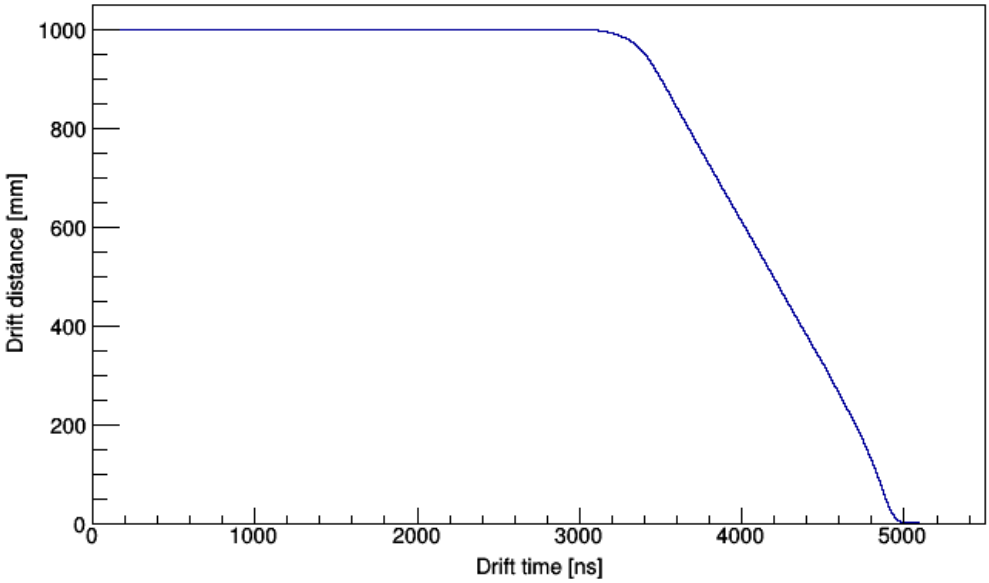


Figure 5.4: The Look-up table (LUT) for the X wireplane used in Exp2

Once the drift lengths for all the associated wire cells triggered by a particle traversing a wire-plane are determined, a ray-tracing subroutine is implemented to reconstruct its trajectory and determine the precise point at which the particle crossed the wire-plane.

A schematic of a particle traversing through a wire-plane and depositing energy across various drift cells along its track is shown in the upper part of figure 5.5. The separation distance $s$ between each signal wire is indicated, as well as the drift length $y_{wire\#}$ between the point of energy deposition and the respective signal wire for each triggered cell. The lower part of figure 5.5 shows the corresponding drift length vs drift cell number spectrum for the set of triggered signal wires. This spectrum ideally should exhibit a "V" type structure due to the inability to deduce information on which side of the wire was actually triggered from drift time alone.

Occasionally, "W" and "Z" type structures, as shown in figure 5.6 and figure 5.7, may also occur. Whether these arise due to spurious electronic behaviour or actual physical events is still under question. Part of the ray-tracing procedure therefore functions to remove the uncorrelated events in these "W" and "Z" type structures, in order to reconstruct "V" type event tracks.

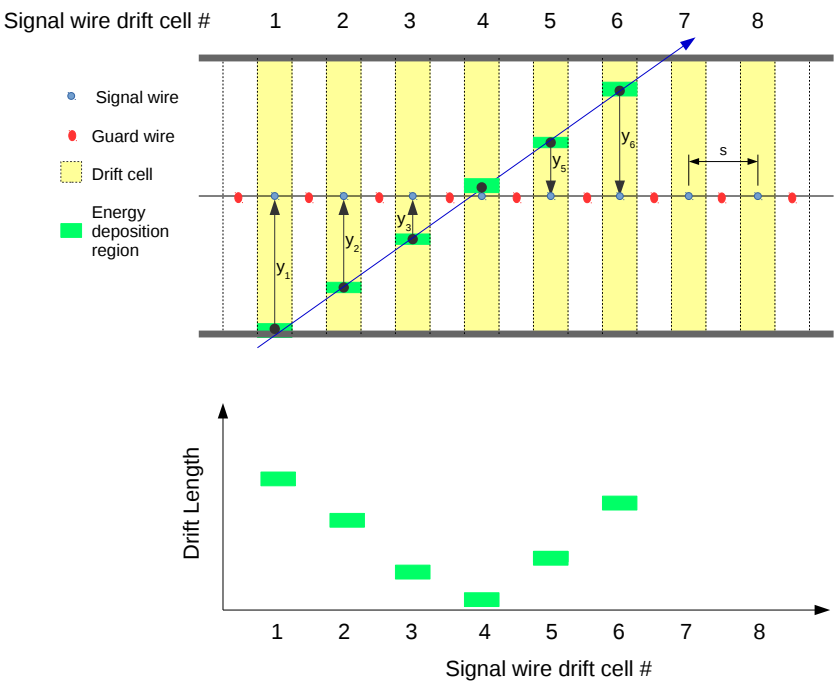


Figure 5.5: Schematic diagram of a typical trajectory associated with a charged particle passing through a wire-plane, resulting in a V type structure.

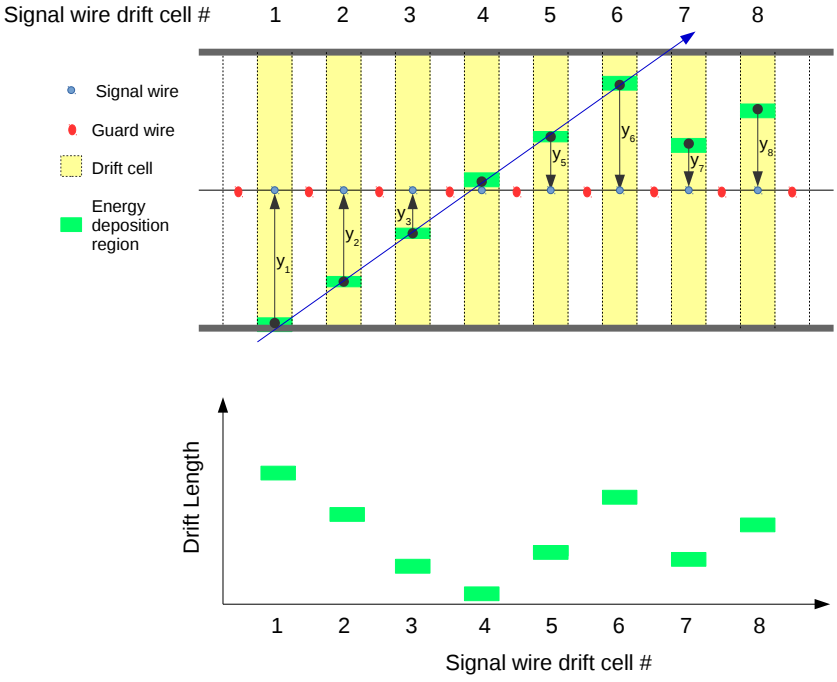


Figure 5.6: Schematic diagram of an event track triggering a "W" type structure

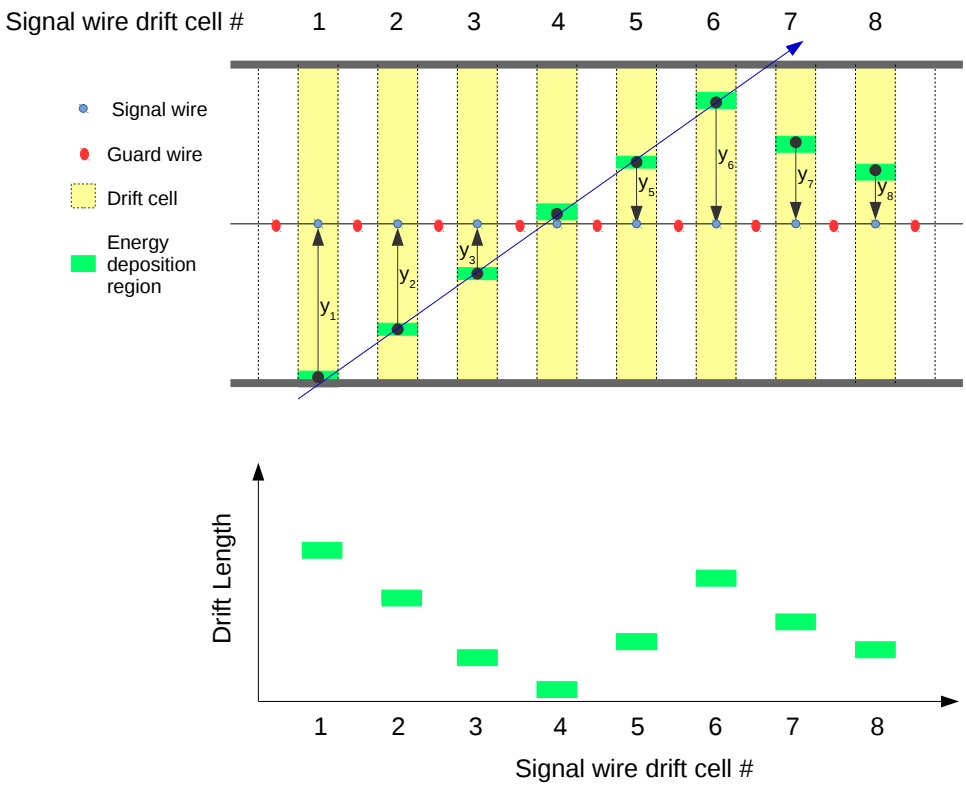


Figure 5.7: Schematic diagram of an event track triggering a "Z" type structure

The ray-tracing subroutines work as follows:

(1) It identifies the first and last wires for the set of adjacent triggered wires corresponding to a "V" type track. It further identifies the wire with the shortest drift distance in order to gauge the point of inversion.

(2) In the instance where multi-hits occur in a particular drift cell, a logic flow following the conditions highlighted in figure 5.8 is followed in order to choose the drift-distance most likely to correlate to the true particle track.

This wire is then excluded from the fitting procedure described later, as for the case where a particle travels very close to the signal wire, the energy cascade resulting from the ionisation does not accurately reflect the true drift distance. This has been observed to affect the fitting procedure such that a poorer position resolution is obtained when included.

It is assumed that the trajectory is a straight line within the VDC and thus the slope of

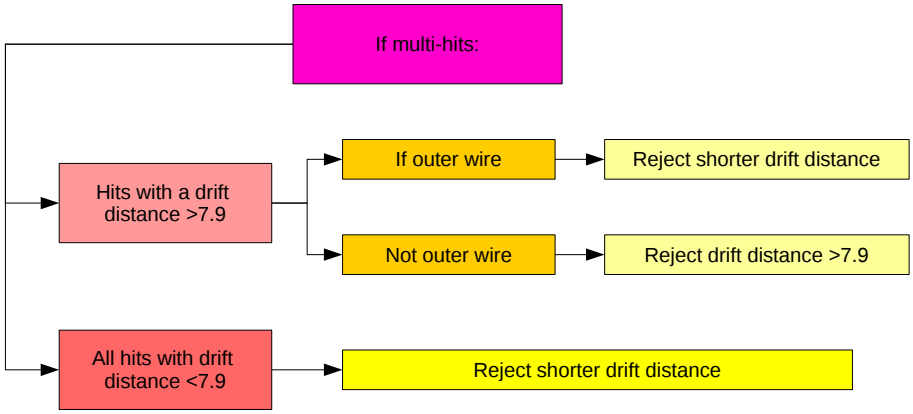


Figure 5.8: Logic flow in the ray-tracing procedure for determining which drift distance is allocated when multi-hits are fired for a triggered wire.

the track is constant. The slope $S$ of the track can be calculated using the drift distances $y_{wire\#}$ for any of the adjacent wire pairs that have been "hit" using:

$$S_{i,i+1} = \frac{y_{i+1} - y_i}{s} \tag{5.5}$$

A linear least squares fit over the various slopes computed is then used to interpolate where the particle track intersects with the focal plane. In the case of the U-wire plane, the inclination of the wires at $50^{o}$ allows to obtain both horizontal and vertical focal plane positions.

Assuming a constant slope, the difference in slopes $D = S_{1,2} - S_{i,i+1}$, for wire hits on either side of the track should ideally be 0. However, statistical fluctuations lead to a distribution centered about 0. The standard deviation $\sigma_D$ of this distribution is then be used to estimate the intrinsic cell accuracy $\sigma_c$ for the VDC and the cell position accuracy $\sigma_x$ as derived in [45] by:

$$\sigma_x = \frac{\sigma_c}{\sqrt{n}} = \frac{\sigma_D}{2\sqrt{n}} \tag{5.6}$$

where $n$ is the number of wires used to determine the position at which the track intersects the focal plane.

### 5.1.3 VDC efficiency

The operational efficiency ($\epsilon$) of the VDCs gives an indication to its ability to detect charged particles. It is described by:

$$\epsilon = \epsilon_g \cdot \epsilon_i \tag{5.7}$$

where $\epsilon_g$ is the geometric efficiency and $\epsilon_i$ is the intrinsic efficiency.

The geometric efficiency is assumed to be 100%, since a previous measurement taken at iThemba LABS using a horizontal drift chamber (HDC) indicated that particles of a selected rigidity are well-focused in the vertical focal plane position.

The intrinsic efficiency is defined by

$$\epsilon_i = \frac{N_{accepted}}{N_{total}} \tag{5.8}$$

where $N_{total}$ is the total number of events recorded at the focal plane, for a selected rigidity, and $N_{accepted}$ is the number of valid events recorded. An event is considered valid based on if it meets the following criteria:

- the TOF and paddle signals should fall within gated regions
- the number of wires "hit" for an event should be between 3-6
- the reduced chi squared ($\chi^2$) of the least squares fit should be less than 1
- and, the drift time should fall within the gated region.

The operational efficiency of the combined XU type VDC is then taken as the product of the efficiencies for each individual wire-plane.

$$\epsilon_{UX} = \epsilon_U . \epsilon_X \tag{5.9}$$

For the $^{154}$Sm data runs, $\epsilon_{UX}$ was 76% and for the $^{144}$Sm data runs, $\epsilon_{UX}$ was 94%. Experimental factors that affect the efficiency of the VDC include the condition of the gas and the amount of high voltage applied to the respective wire-planes.

### 5.1.4 Line-shaping procedures

The position resolution for a given excitation of the residual nucleus, particularly for the 0° mode in which the angular acceptance for the spectrometer is ±2°, is mainly affected by two things. Particles emitted from the target at different reaction angles for the same excitation energy have different momenta and therefore arrive at the focal plane over a more spread out region. Secondly, optical aberrations in the beam profile also have an effect. While the K and H trim coils are used to minimise these effects, the residual effects can be corrected for by using a line-shaping procedure.

The effect mentioned above can be observed when looking at the TOF vs Focal-plane position for $^{24}$Mg data, where discrete states appear as slanted lines. Figure 5.9 shows the TOF vs X position for peaks around 250 mm (left) and 615 mm (right) which correspond to energies of ~14 MeV and the 6.4323 MeV 0+ state in $^{24}$Mg respectively. The influence of the kinematics is evident as states at lower energy (and hence at the higher focal-plane position) appear more slanted than those at higher energies.

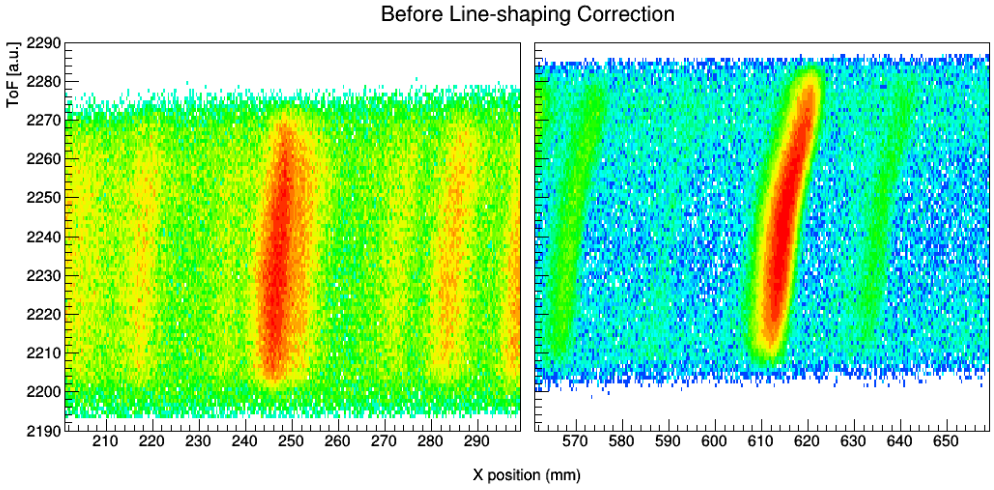


Figure 5.9: Relative particle Time of Flight vs Focal plane position zoomed in on the 250mm (left) and 615 mm (right) $^{24}$Mg target peaks highlighting the slanting in peaks that affect the position resolution.

The line-shaping correction is implemented by correcting the X-position with a 5$^{\text{th}}$ order polynomial function dependent on the TOF. This polynomial function is determined from

fitting the distribution of the X position about a mean X position for the 6.4323 MeV state, as a function of the ToF distribution about a mean ToF value. This is shown in figure 5.10. Furthermore, the correction is implemented in a linear manner such that the position at 250 mm has a 0 factor correction, while the position at 615 mm has a 1 factor correction. The line-shape corrected spectra are shown in figure 5.11.

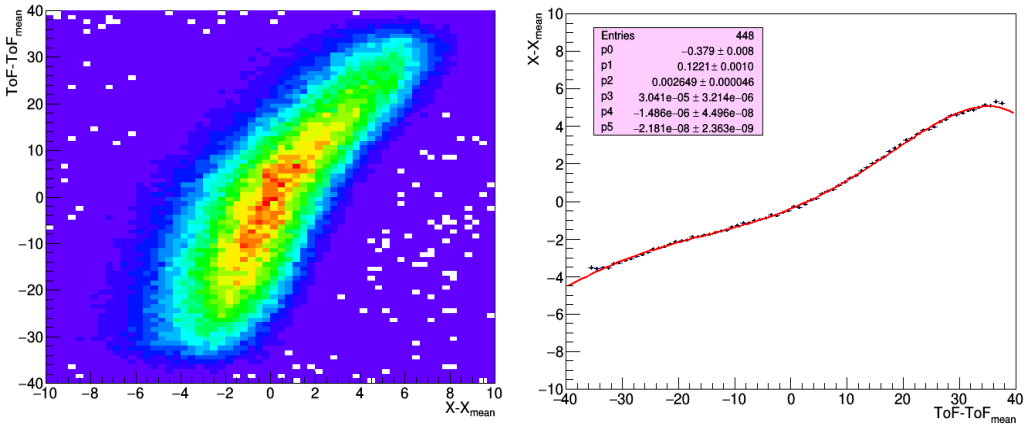


Figure 5.10: Line-shaping correction parameter extraction as implemented on the 6.432 MeV state around 615 mm.

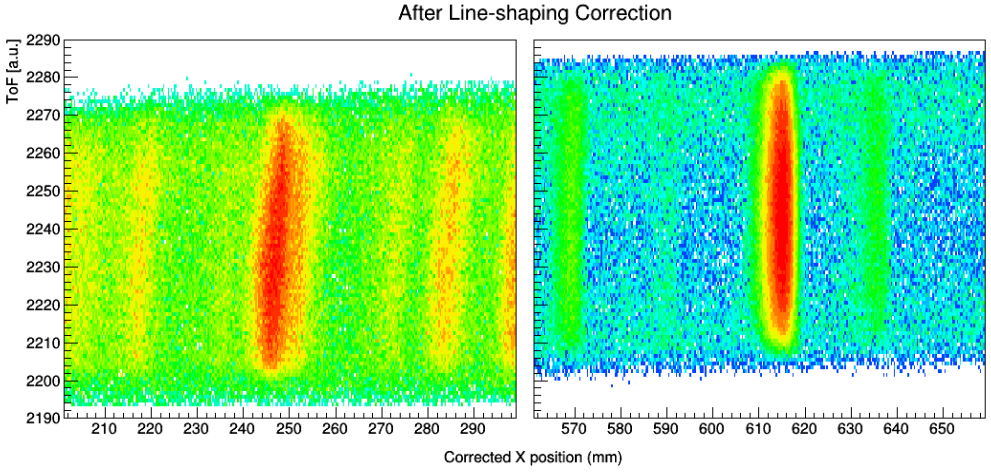


Figure 5.11: ToF vs Focal plane position after implementing the line-shaping correction.

### 5.1.5 Energy Calibration

Since the excitation level densities for the Samarium targets are so high, identifying specific excited states to use towards a direct energy calibration can not be performed. Therefore, the focal plane position spectrum was first calibrated with the particles rigidity using the product QB$\rho$ for known transitions in $^{24}$Mg. The corresponding excitation energy was then calculated for the relevant targets, using the 2-body kinematics equations detailed below:

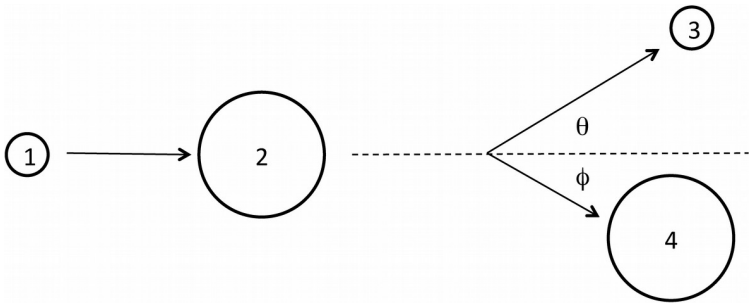


Figure 5.12: Schematic of the kinematics of a nuclear reaction

Energy conservation law:

$$E_1 + E_2 = E_3 + E_4 + E_x \tag{5.10}$$

Momentum conservation law:

$$\begin{aligned} p_1 &= p_3 \cos\theta + p_4 \cos\phi \\ 0 &= p_3 \sin\theta - p_4 \sin\phi \end{aligned} \tag{5.11}$$

note: $E = T + mc^2$, $E^2 = p^2c^2 + m^2c^4$ and $Q = (m_1 + m_2 - m_3 - m_4)c^2$.

Taking the square of equations 5.11

$$\begin{aligned} (p_1 - p_3 \cos\theta)^2 &= p_4^2 \cos^2\phi \\ p_3^2 \sin^2\theta &= p_4^2 \sin^2\phi \end{aligned}$$

and summing them, result in:

$$\begin{aligned} p_1^2 - 2p_1p_3\cos\theta + p_3^2\cos^2\theta + p_3^2\sin^2\theta &= p_4^2(\sin^2\phi + \cos^2\phi) \\ p_1^2 + p_3^2 - 2p_1p_3\cos\theta &= p_4^2 \end{aligned} \tag{5.12}$$

From equation 5.10

$$T_1 + m_1c^2 + m_2c^2 = T_3 + m_3c^2 + T_4 + m_4c^2 + E_x \tag{5.13}$$

$$\begin{aligned} E_x &= T_1 - T_3 - T_4 + m_1c^2 + m_2c^2 - m_3c^2 - m_4c^2 \\ E_x &= T_1 - T_3 - T_4 + Q \end{aligned} \tag{5.14}$$

$$\begin{aligned} T_1 &= T_{beam} \\ T_3 &= \sqrt{p_3^2c^2 + m_3^2c^4} - m_3c^2 \\ T_4 &= \sqrt{p_4^2c^2 + m_4^2c^4} - m_4c^2 \end{aligned} \tag{5.15}$$

using equation 5.12

$$T_4 = \sqrt{p_1^2c^2 + p_3^2c^2 - 2p_1p_3c^2\cos\theta + m_4^2c^4} - m_4c^2 \tag{5.16}$$

$$E_x = T_1 - \sqrt{p_3^2c^2 + m_3^2c^4} + m_3c^2 - \sqrt{p_1^2c^2 + p_3^2c^2 - 2p_1p_3c^2\cos\theta + m_4^2c^4} + m_4c^2 + Q \tag{5.17}$$

For the inelastic scatting case Q = 0, using natural units where c=1:

$$E_x = T_1 - \sqrt{p_3^2 + m_3^2} + m_3 - \sqrt{p_1^2 + p_3^2 - 2p_1p_3\cos\theta + m_4^2} + m_4 \tag{5.18}$$

The excitation peaks used for the calibration are identified in the final position spectrum for $^{24}$Mg targets shown in figure 5.13 for Exp1 - $^{154}$Sm data taking (top) and Exp2 - $^{144}$Sm data taking (bottom). In Exp1, a thin 0.7 mg/cm$^3$ $^{24}$Mg target was used while in Exp2 the $^{24}$Mg target was 3.307 mg/cm$^3$.

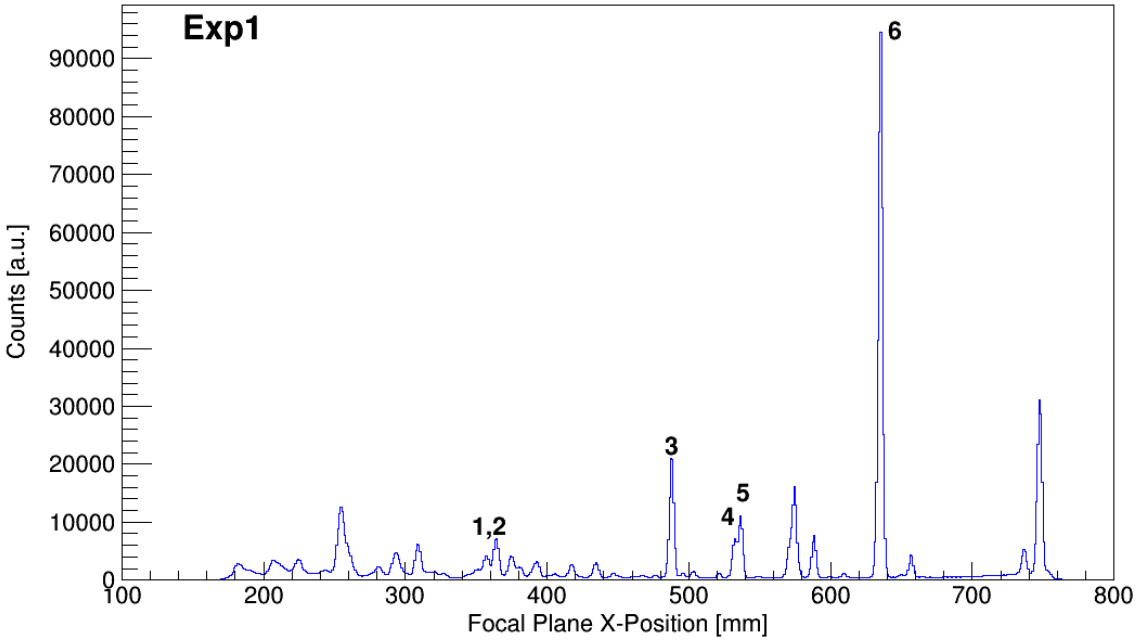


(a)

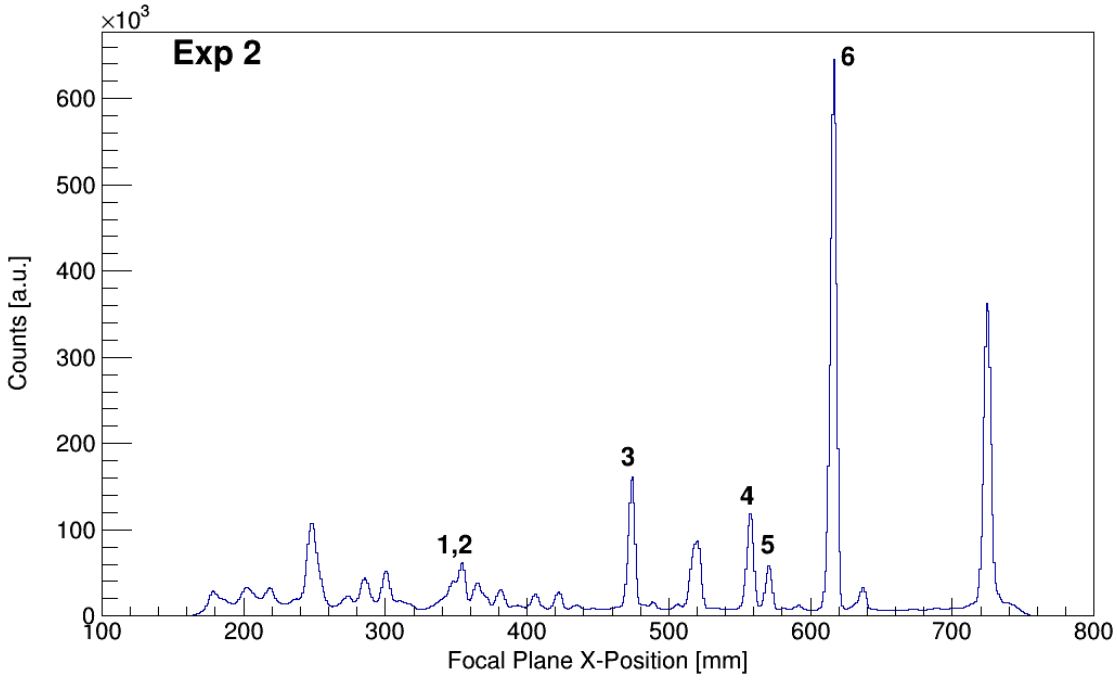


(b)

Figure 5.13: Focal Plane X position for $^{24}$Mg data indicating the peaks used in the calibration.

For the thicker target, the chance for a reaction projectile to interact with the target and undergo small energy losses increases. As result, each excitation peak gets distributed over a wider spread in energy. Hence, the peaks observed for the thin Mg target in Exp1 appear more distinct compared to those in Exp2. In addition, the collimator between the target chamber and spectrometer entrance in Exp2 was placed incorrectly, resulting in approximately 0.3 mm of its metal lip being positioned within the beam stream and hence causing some additional energy losses. As a result, these peaks have a low energy tail.

The calibration peaks in Exp1 were fitted with a Gaussian function, while the peaks in Exp2 were fitted with a Gaussian + Exponential function in order to determine the centroid position. The program JRelKin [51] was used to calculate the QB$\rho$ values corresponding to the excitation peaks used. The corresponding values for the two experiments are summarised in tables 5.1 and 5.2. The calibration points were then fitted with a 3$^{\text{rd}}$ order polynomial function. The calibration curves for the two experiments are shown in figure 5.14

Table 5.1: Summary of parameters used for the rigidity calibration in Exp1

| No. | $E(peak)[MeV]$ | J$\pi$ | X position $[mm]$ | QB$\rho$ $[ekGcm]$ |
|---|---|---|---|---|
| 1 | 11.8649 | 1- | 357.303 | 2985 |
| 2 | 11.7281 | 0+ | 364.002 | 2987 |
| 3 | 9.3054 | 0+ | 487.669 | 3022 |
| 4 | 8.4373 | 1- | 532.096 | 3034 |
| 5 | 8.3580 | 3- | 536.261 | 3035 |
| 6 | 6.4323 | 0+ | 634.878 | 3062 |

Table 5.2: Summary of parameters used for the rigidity calibration in Exp2

| No. | $E(peak)[MeV]$ | J$\pi$ | X position $[mm]$ | QB$\rho$ $[ekGcm]$ |
|---|---|---|---|---|
| 2 | 11.7281 | 0+ | 346.2 | 3023 |
| 3 | 9.3054 | 0+ | 466.6 | 3057 |
| 4 | 7.6165 | 3- | 550.6 | 3081 |
| 5 | 7.3490 | 2+ | 563.5 | 3085 |
| 6 | 6.4323 | 0+ | 609.3 | 3098 |

The calibrated excitation energy spectra are shown in figure 5.15. In Exp1, a resolution of 68 keV @ 6.43 MeV was achieved for the 0.7 mg/cm$^3$ $^{24}$Mg target. While in Exp2, a resolution of 102 keV @ 6.43 MeV was achieved for the 3.3 mg/cm$^3$ $^{24}$Mg target.

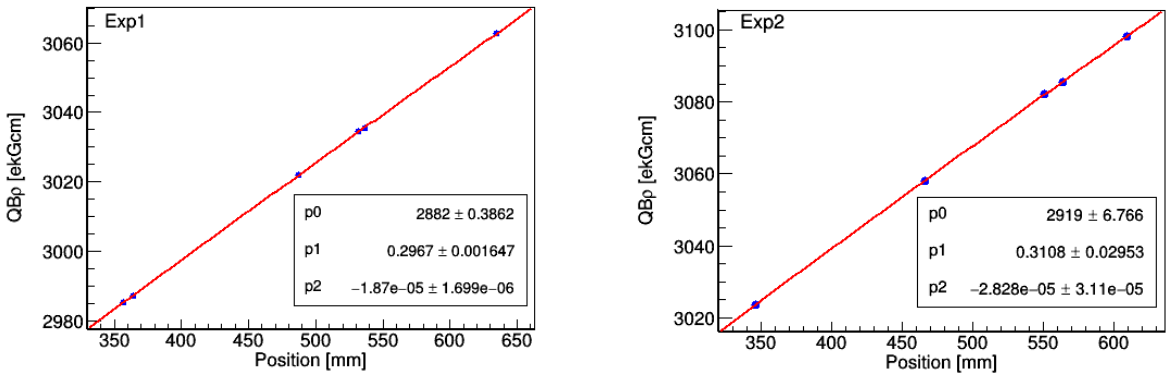


Figure 5.14: Rigidity calibration curves fitted with a $3^{rd}$ order polynomial function for each experiment as indicated

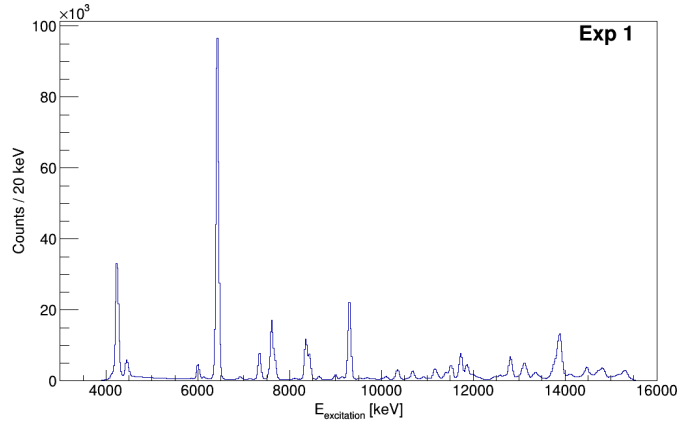


(a)

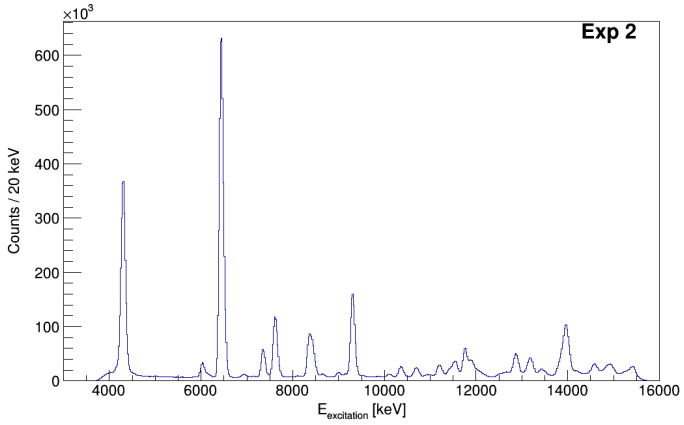


(b)

Figure 5.15: Calibrated Excitation energy spectra for $^{24}$Mg targets of (a) 0.7mg/cm$^3$ and (b) 3.3 mg/cm$^3$ thickness.

## 5.2 BaGeL - Clover Data reduction

The main components in the data reduction of the HPGe Clover detectors entail:

1. Calibrating the ADC channels to energy.
2. Selecting the events arriving in the prompt time peak.
3. Implementing an addback procedure between the four crystal segments.
4. Performing an efficiency calibration to determine the accuracy of the detector system.

Further descriptions for each of these are presented in the proceeding sections.

### 5.2.1 Energy Calibration

Preliminary energy calibrations were performed using the 667 keV gamma peak of $^{137}$Ce and the 1.1732 MeV and 1.3325 MeV peaks of $^{60}$Co radioactive sources. The radioactive sources were positioned on the target ladder in the scattering chamber, and data was collected before, during and after the beam data acquisition periods.

The preliminary calibration was used for identifying the rough placement of gamma peaks in the $^{24}$Mg in-beam data. A final calibration was then performed using the gamma decays corresponding to the 6.432 MeV excitation in $^{24}$Mg. A decay scheme for this excitation is shown in fig.5.16.

The 5.063, 2.193 and 1.368 MeV peaks were used, as well as the 1$^{st}$ and 2$^{nd}$ escape peaks resulting from pair production of the 5.063 MeV decay as it interacts with the detector (4.552 and 4.041 MeV respectively). The calibration was performed for each clover segment individually. A straight line was fitted through the calibration points. The final calibrated spectrum of the 6.432 MeV $^{24}$Mg excited state decays for all the clovers (in Exp2) summed together is shown in fig.5.17 below. A resolution (FWHM) of 17.2 and 20.6 keV were achieved for Exp1 and Exp2 respectively.

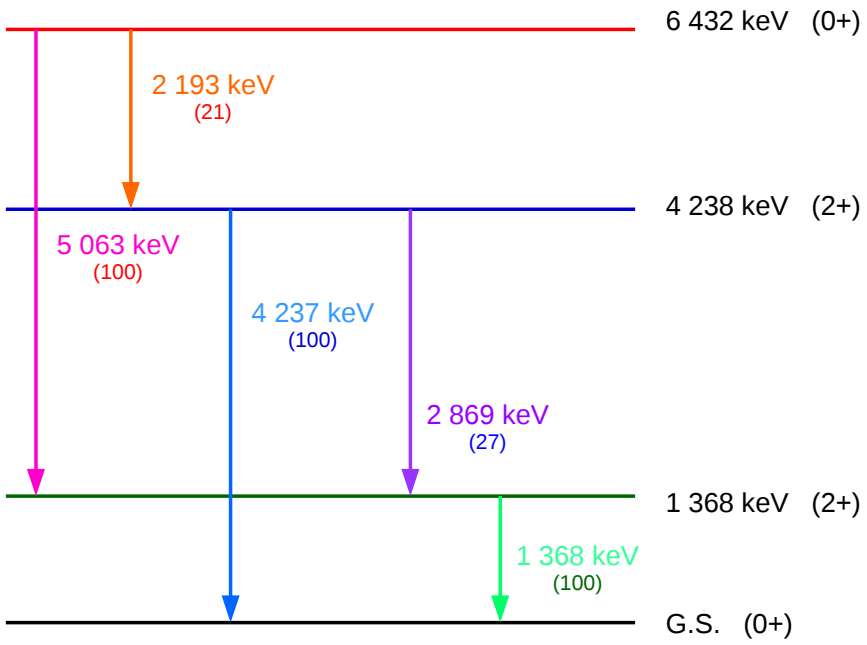


Figure 5.16: Decay scheme for the 6.432 MeV excited state in $^{24}$Mg. The relative intensities for the gamma decays are indicated in the brackets below the corresponding gamma energy.

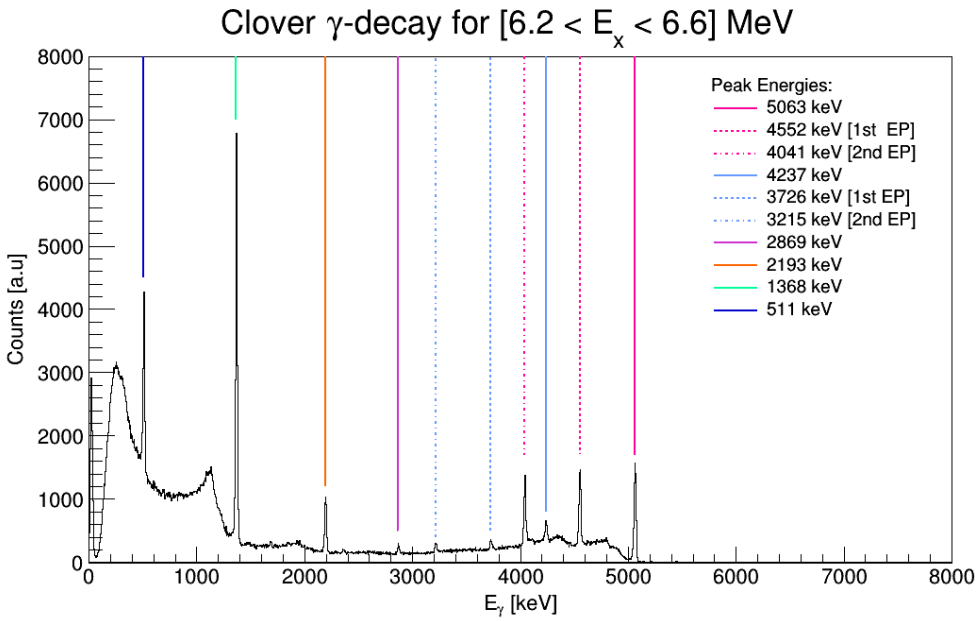


Figure 5.17: Calibrated gamma decay spectrum for all clovers summed with a selection on the 6.432 MeV excited state in $^{24}$Mg.

### 5.2.2 Gamma Time Selection

The gamma-time gets recorded for events occurring within a 2 $\mu$s window, once a signal from the paddle detector is triggered. This window encompasses events both forward and back in time, since gamma's arrive at the BaGeL detectors before the co-incident alpha's reach the paddle detector. Since real coincidence events occur with a specific time difference, a prompt peak stands out prominently. Random coincidences on the other hand can occur at any time within the opening window and appear as periodic peaks corresponding in time to the subsequent beam bunches generated by the SSC.

Figure 5.18 shows the gamma-time spectrum relative to the RF signal of the SSC for an individual Clover detector used in each experimental campaign respectively. An offset was implemented to shift the prompt peak so that it is centered around 0 ns for each clover segment, in order to account for variations due to different cable lengths and readout delays. The offset was determined from the centroid of the prompt peak as fitted with a 2-sigma Gaussian function.

In order to reduce the number of background events in the gamma-decay spectra, a selection criteria was imposed on the gamma-time thereby selecting only events which occur in the prompt peak. The timing resolution achieved for measurements on $^{144}$Sm and $^{154}$Sm were 25 ns and 17 ns respectively. The use of the MCF-16 mesytec module for the amplification of the data in the $^{144}$Sm experiments is responsible for the loss of resolution in comparison to when the CAEN V1190 TDC modules were used, since these modules are not optimized for use with HPGe detectors. The time between each beam burst entering the reaction chamber (~90 ns), can be noted from observing the time difference between two consecutive peaks in Fig.5.18. Thus in both experiments, the timing resolution was sufficient to separate the prompt peak from random coincidence peaks.

Figure 5.19 shows the matrix of gamma-time's for each clover segment after offset implementation from Exp2 showcasing a very small variation in the alignment of the prompt peak. Figure 5.20 shows the matrix of the summed gamma-time spectra of the full array versus run entries for the full chained data run set. The prompt-peak selection window is

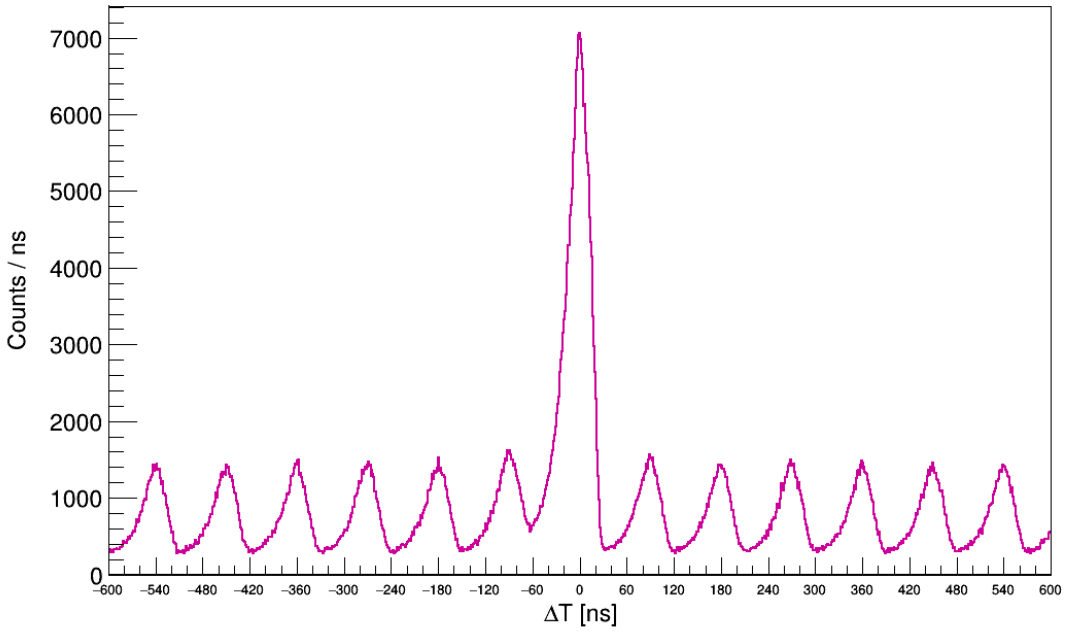


(a) $^{144}$Sm - Clover 7 data

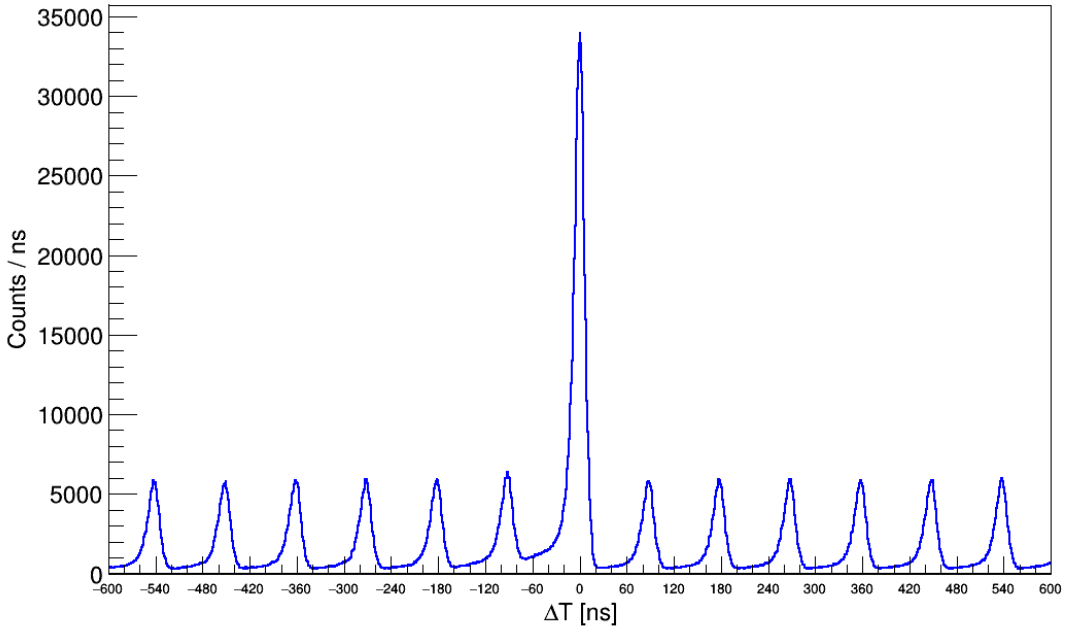


(b) $^{154}$Sm - Clover 4 data

Figure 5.18: The time spectrum for an individual HPGe detector from each experiment, measured relative to the radio frequency (RF) of the SSC

indicated by the dashed black lines. The Gamma-time prompt peak does not appear to vary over the course of the data acquisition period.

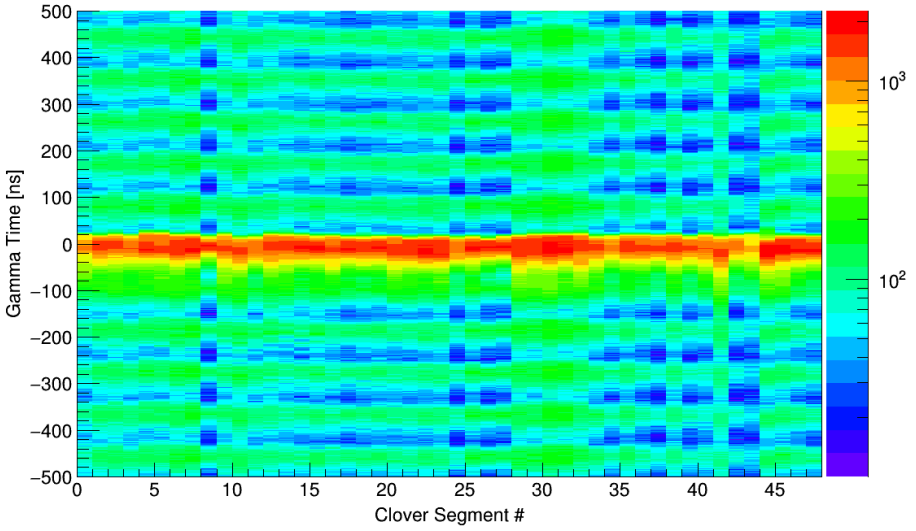


Figure 5.19: Matrix of Gamma Time for each Clover detector segment during Exp2.

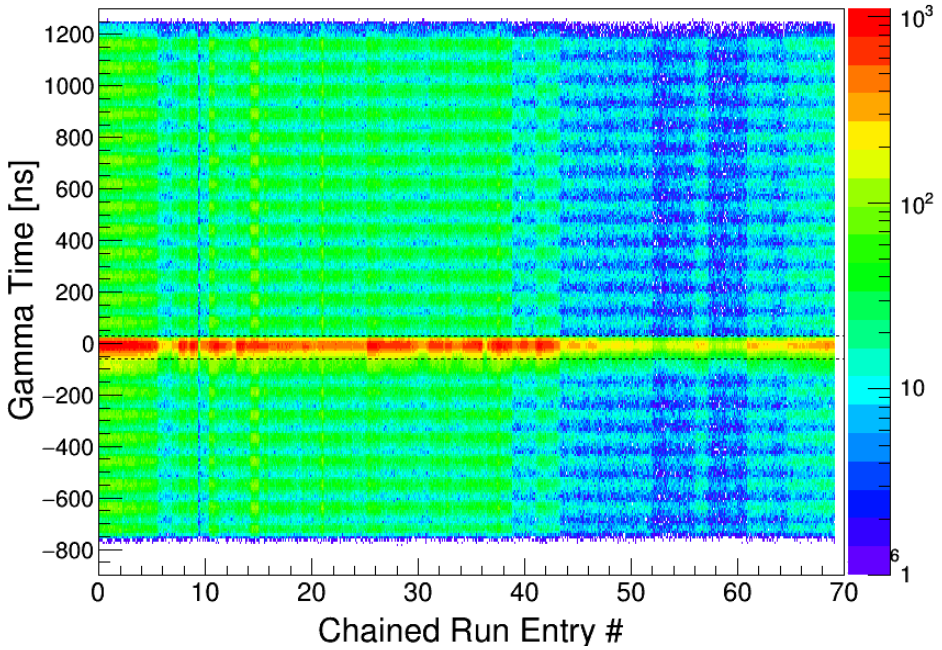


Figure 5.20: Matrix showing the variation in Gamma time for full Clover array with run entries in the chained $^{24}$Mg data from Exp2.

### 5.2.3 Addback

Each individual HPGe clover is composed of 4 crystal segments packed in close proximity to each other. The full energy of a gamma ray can thus be deposited in one or more of the segments. In the singles mode, the energy deposited in a single segment only is considered. In the addback mode, the full energy peak can be reconstructed by summing the energies deposited in the multiple segments that fired for a given event.

A comparison between the singles and addback events for the gamma-decay spectra from the 6.432 MeV excited state in $^{24}$Mg is shown in figure 5.21.

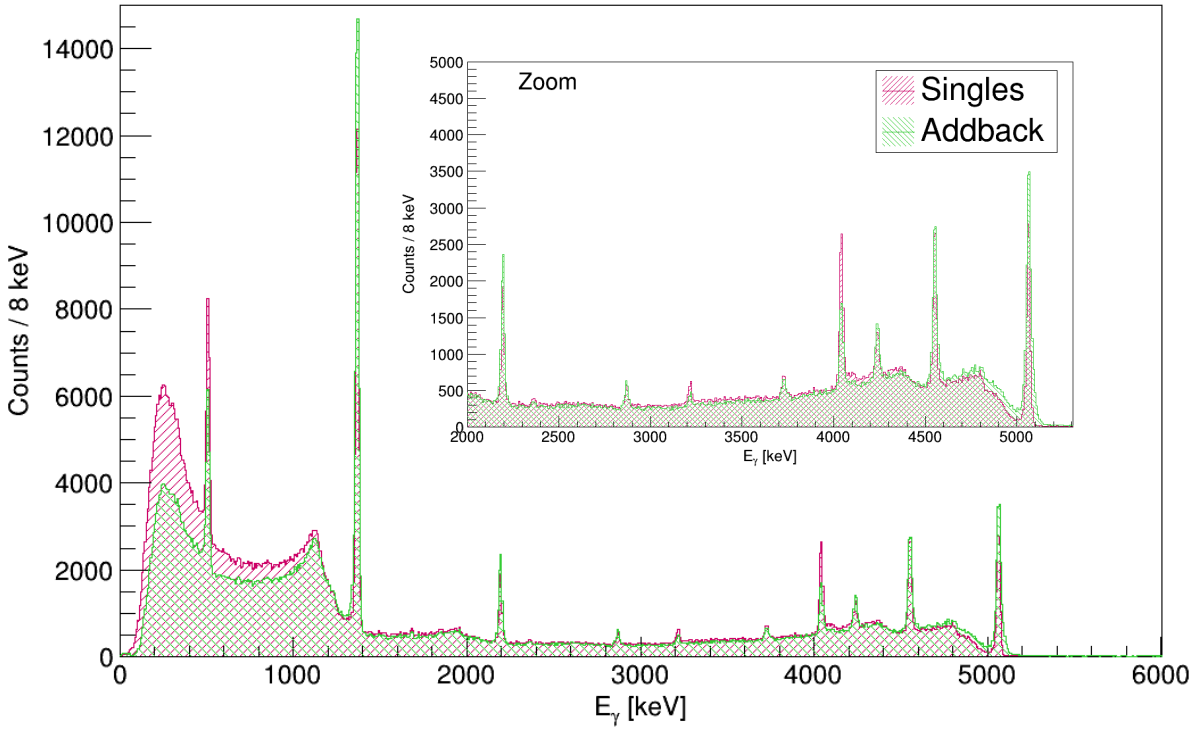


Figure 5.21: Comparison of the Clover Addback mode vs singles mode $\gamma$-decay spectra from the 6.432 MeV excited state in $^{24}$Mg.

A significant reduction of low energy gamma's is observed, while the full energy photopeaks at 1368 keV, 2193 keV and 5063 keV all increase in counts. Furthermore, the recovery of the 5063 keV peak from pair production effects can also be observed as the counts at 511 keV and the 2$^{nd}$ escape peak at 4041 keV get reduced. The counts in the 1$^{st}$ escape peak at

4552 keV also increase for the case where only one of the electron pairs passes through the detector while the other escapes detection.

The addback factor is defined as the ratio between the efficiency in addback mode vs the efficiency in singles mode. An addback factor of 1.6 was achieved for the peak at 5.063 MeV, indicating that the number of counts in that photopeak increased by 60%. All gamma spectra extracted for the remaining parts of the analysis make use of the Clover detectors in addback mode.

### 5.2.4 Clover Efficiencies

The absolute photopeak efficiency of a detector is a measure of its likelihood to detect the full energy of an incident gamma-particle. It is defined by:

$$\epsilon_{abs} = \epsilon_{geo}.\epsilon_{int} \tag{5.19}$$

where $\epsilon_{geo}$ is the geometric probability for the photon being emitted in the direction of a particular crystal and $\epsilon_{int}$ is the intrinsic probability that the full energy is deposited in that crystal.

Efficiency calibration measurements were taken for each HPGe detector both prior to and after data taking for each experiment, using a $^{152}$Eu source. In order to ensure a consistent measure of $\epsilon_{geo}$, the source was placed at the target position in the scattering chamber. Calibration points up to 1.4 MeV could be obtained.

Additional efficiency points were computed using the 5.063, 2.193 and 1.368 MeV gamma decays corresponding to the 6.432 MeV excitation for in-beam $^{24}$Mg data, for which the branching ratio for these decays are well known. In Exp1, a good correlation between the $^{152}$Eu and $^{24}$Mg efficiencies were obtained. In Exp2 however, the $^{152}$Eu measured efficiencies were too low and it is suspected that an issue may have occurred with the OR trigger implemented between Clovers for the radio-active source measurements particularly relating to the mesytec read-out. Thus only the $^{24}$Mg in-beam efficiencies were considered.

In order to extrapolate the efficiencies for the full energy range of the gamma-detectors, Monte-Carlo simulations were performed using GEANT4 [52] which were then normalised to the measured efficiencies. The full geometry of the K600 spectrometer, its focal plane detection system and the BaGeL array were incorporated into the GEANT4 simulations using a CAD model import interface called CADMesh [53].

The efficiencies were experimentally deduced and simulated for the Clover detectors in both singles and addback modes. The absolute photo-peak efficiency at 1.3 MeV, for each individual detector in addback mode varied between 0.15%-0.21% in the $^{154}$Sm experiments and 0.1%-0.16% in the $^{144}$Sm experiments. The absolute photo-peak efficiency at 1.3 MeV for the full array was 1.49% and 1.32% for the respective experiments.

## 5.3 The Coincidence matrix

In the previous sections, the data reduction procedures necessary for extracting the excitation energies ($E_x$) and decay energies ($E_\gamma$) were described. By correlating the two sets of information, a coincidence matrix is obtained. The coincidence matrix for $^{24}$Mg data is shown in Fig. 5.22.

For the strongly excited energy states, the corresponding $\gamma$-decays can be observed as horizontal lines owing to the much better energy resolution of the HPGe-detectors in comparison to that of the K600. The solid diagonal bands indicated on the figure show transitions to specific states. The solid black band satisfies the condition $E_\gamma = E_x$, where direct decays to the ground state ($0^+$) occur. The solid magenta band indicates decays to the 1$^{\text{st}}$ excited state ($2^+$), satisfying the condition $E_\gamma + E_{2^+} = E_x$.

One can generate excitation energy spectra or $\gamma$-decay spectra for specific transitions by projecting onto the corresponding axis of the coincidence matrix while applying a gating condition which accommodates for the necessary energy resolutions. The upper and lower bounds of these gated selection bands are indicated by the dashed lines on the matrix in Fig. 5.22.

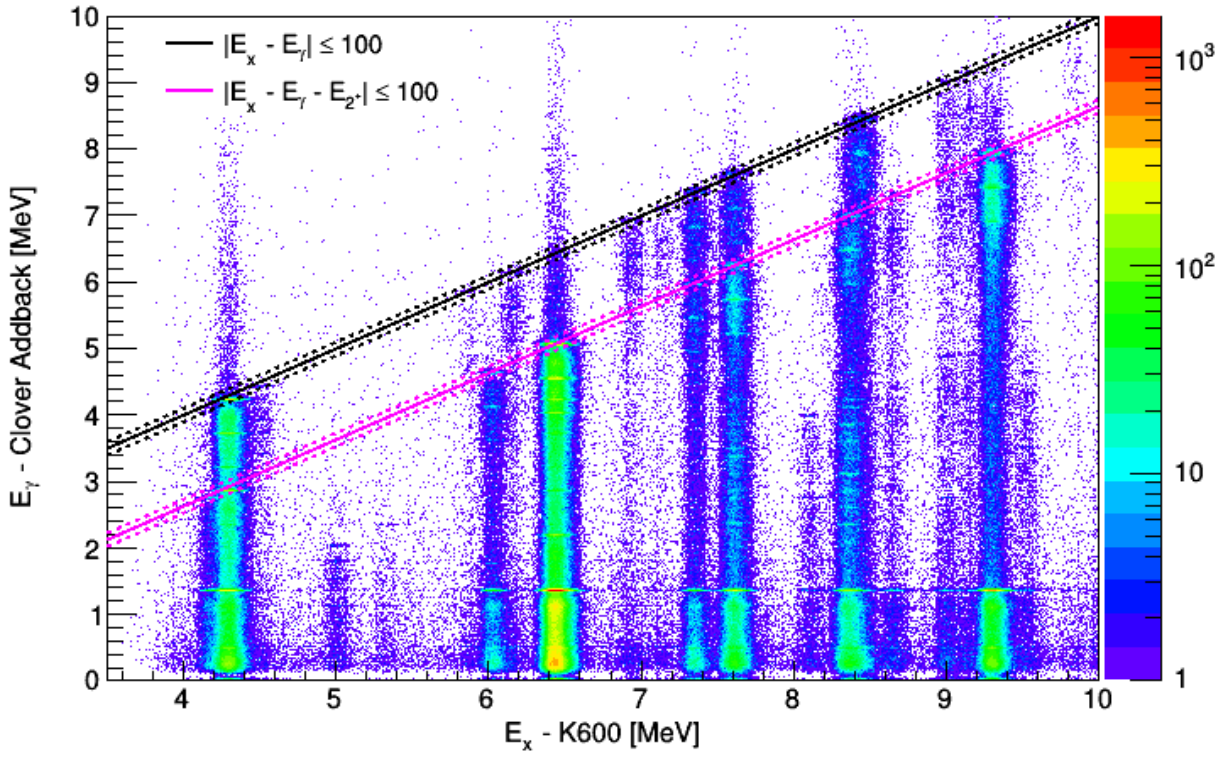


Figure 5.22: The $\alpha$-$\gamma$ coincidence matrix obtained for $^{24}$Mg data measured in Exp1. A good correlation between the $\alpha$ excitation energies ($E_x$) measured by the K600 focal plane detectors and their corresponding $\gamma$-decay ($E_\gamma$) measured by the BageL Clover detectors can be observed. The black diagonal band indicates $\gamma$-decays to the ground state, while the magenta band indicates decays to the $1_{st}$ excited state at 1.368 MeV.

Figure 5.23 shows the projections of $^{24}$Mg for the full matrix in the upper panels, the projections gated on the ground state in the middle panels and the projections gated on the first excited state in the lower panels. A large reduction in the background and better refinement of individual peaks is observed for each of the transition gated cases in comparison to the full projections.

From the total number of coincidence events in the matrix, 0.86% occur in the ground state band and 3.5% occur in the first excited state decay band. It should be noted that $^{24}$Mg is a self-conjugate nucleus where isoscalar dipole excitation's are not particularly favoured and there is a greater propensity for states to decay to the 1st excited state.

The coincidence matrix obtained for $^{144}$Sm$(\alpha, \alpha'\gamma)$ and $^{154}$Sm$(\alpha, \alpha'\gamma)$ are shown in Fig. 5.24

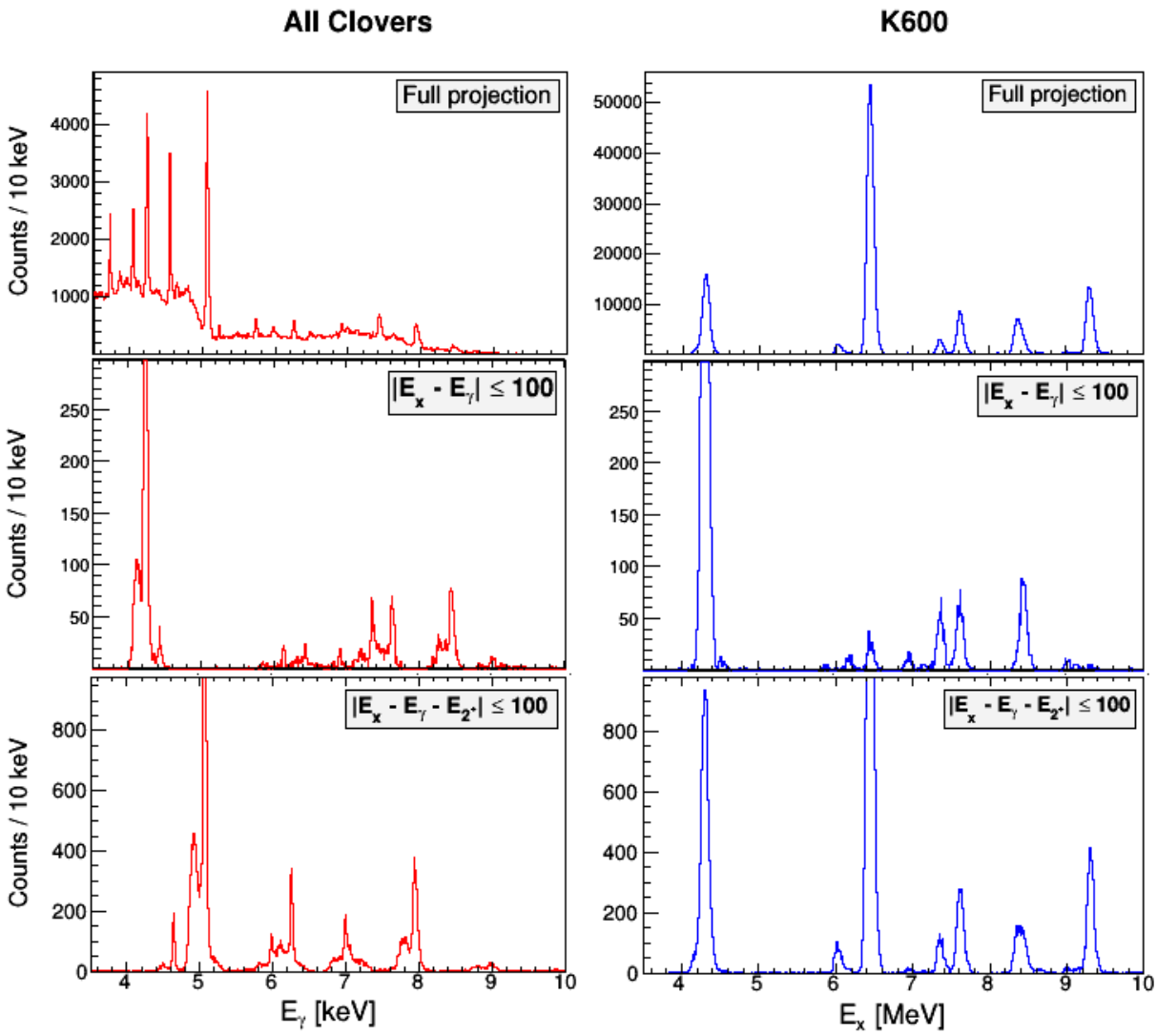


Figure 5.23: Projections of the $\gamma$-ray spectra (left panel) and excitation-energy spectra (right panel) from the $^{24}$Mg$(\alpha, \alpha'\gamma)$ data, without any gating condition (top), gated on ground state transitions (middle) and gated on transitions to the 1$^{st}$ excited state (bottom).

and Fig. 5.25 respectively. A distinct dip in events can be observed in both figures at excitation energies corresponding to the neutron separation energy ($S_n$) of each isotope. In $^{144}$Sm, the $S_n$ is known to occur at 10.519 MeV whilst for $^{144}$Sm it occurs at 7.966 MeV. For excitations above this threshold, the main decay mechanism is via neutron emission. The gamma decays measured thereafter correspond to excitation of the (N-1)Sm isotope.

The decay bands for transitions to the ground state and first excited state are indicated on the matrices. In $^{144}$Sm, the first excited state occurs at 1.660 MeV and a strong horizontal

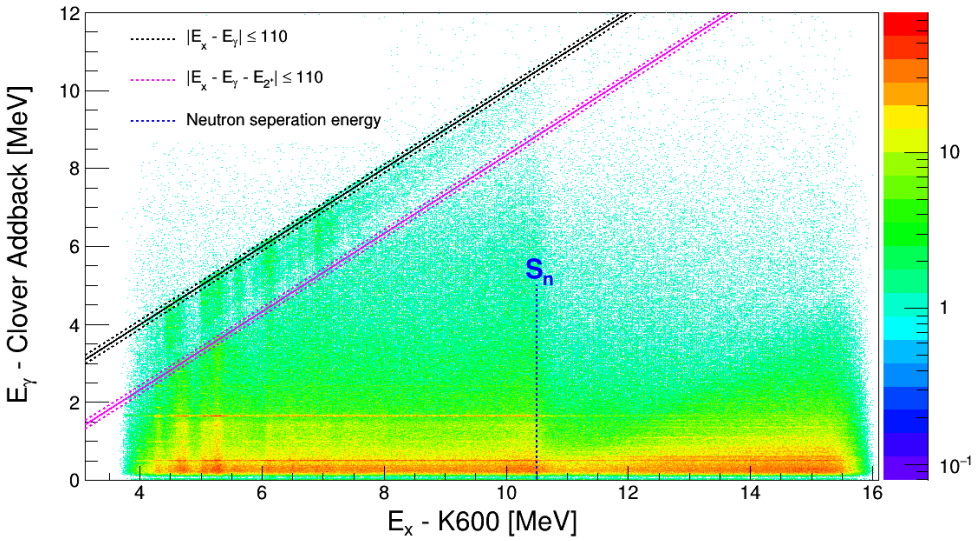


Figure 5.24: The $\alpha$-$\gamma$ coincidence matrix obtained for $^{144}$Sm data measured in Exp2. The $\alpha$ excitation energies ($E_x$) measured by the K600 focal plane detectors are shown on the x-axis and their corresponding $\gamma$-decay ($E_\gamma$) measured by the BageL Clover detectors are shown on the y-axis. The black diagonal band indicates $\gamma$-decays to the ground state, while the magenta band indicates decays to the $1_{st}$ excited state at 1.66 MeV.

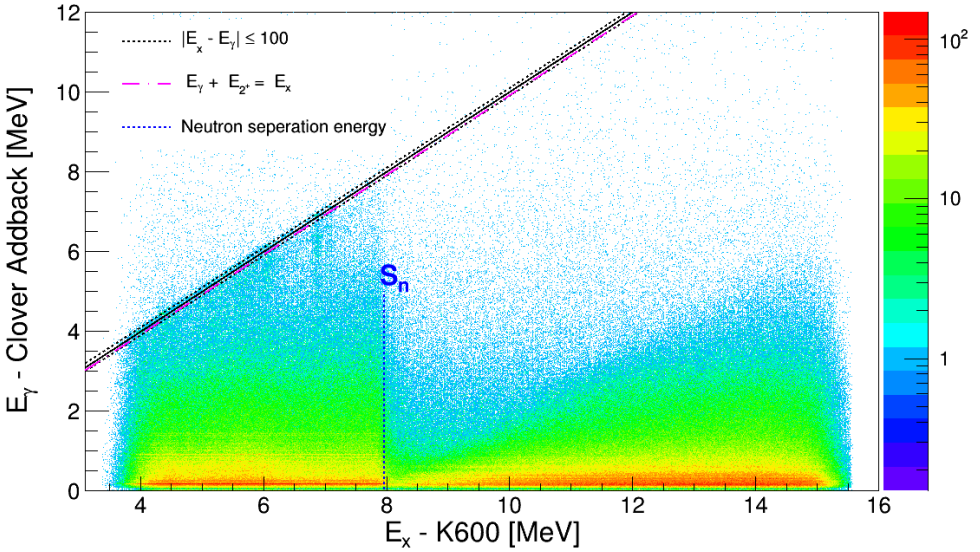


Figure 5.25: The $\alpha$-$\gamma$ coincidence matrix obtained for $^{154}$Sm data measured in Exp2. The $\alpha$ excitation energies ($E_x$) measured by the K600 focal plane detectors are shown on the x-axis and their corresponding $\gamma$-decay ($E_\gamma$) measured by the BageL Clover detectors are shown on the y-axis. The black diagonal band indicates $\gamma$-decays to the ground state, while the magenta band indicates decays to the $1_{st}$ excited state at 81.98 keV.

line of gamma decays at this energy is observed for a range of excitation energies. In $^{154}$Sm, the first excited state occurs at 81.981 keV. Due to the limitation in the resolution for detectors used, there is an overlap between the ground state and first excited state decay bands. Since dipole excitation's predominantly decay to the ground state, the $\gamma$-decay projections employing a gating condition was employed to study the direct decay of these states. In $^{144}$Sm, the width of the gate considered was 220 keV, whilst for the $^{154}$Sm data a 200 keV wide gate, as well as a broader 400 keV gate to fully include direct decays to the $1^{st}$ excited state were used.

## 5.4 Background subtraction

Through the technique of applying the diagonal gate cut on the coincidence matrix, a significant amount of background is eliminated. A small amount of random coincidence events however, can still occur within this gated region. In order to estimate the background due to these, the coincidence matrix obtained for a selection of events occurring within an off-prompt gamma time peak is considered.

The off-prompt time peak used to generate the background matrix is indicated in Fig. 5.26 and the matrix is shown in Fig.5.27. One can observe very few counts present, particularly in the region where the ground state decay cut is implemented. In addition, a consistent trend in the background along the excitation energy axis is observed. The background appears to be dominated by low energy $\gamma$-rays as expected.

To deduce the background for the ground state decay transitions for each samarium isotope, the gamma projections of their respective background matrices were taken using the same decay band cut selections as that used on the prompt time peak data. Figures 5.28 and 5.29 show the counts spectra of the ground state decay data with their corresponding backgrounds for $^{144}$Sm and $^{154}$Sm respectively. The background spectra were then directly subtracted from the relevant counts spectra in order to remove the background due to random coincidence events.

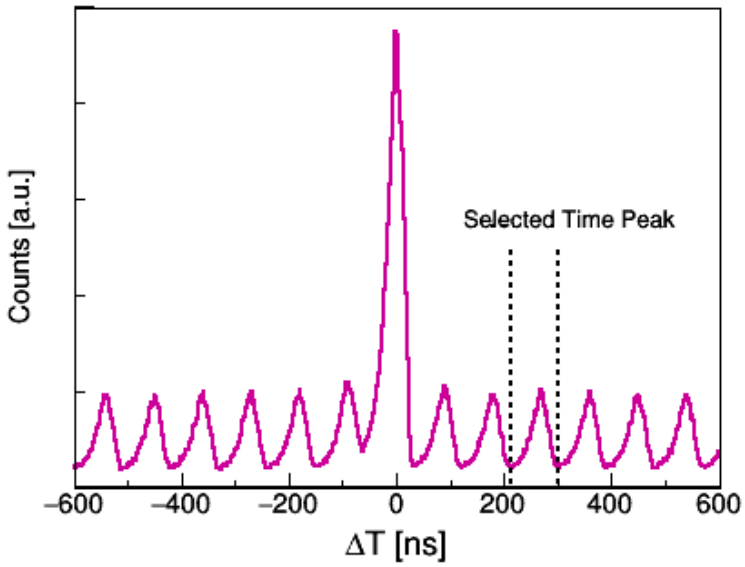


Figure 5.26: Plot of the time at which measured $\gamma$-particles arrived at the clover detectors with respect to the RF of the SSC . The selected off-prompt used for generating the random co-incidence background matrix is indicated by the black dashed lines.

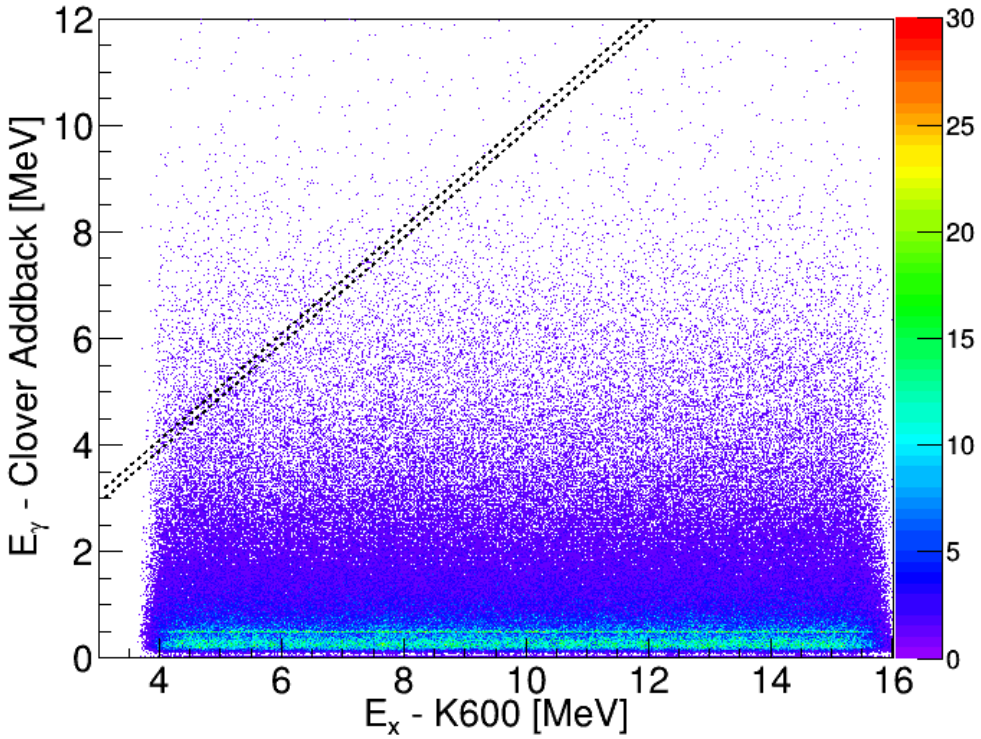


Figure 5.27: Background matrix with the gated band region indicated in black dashed lines

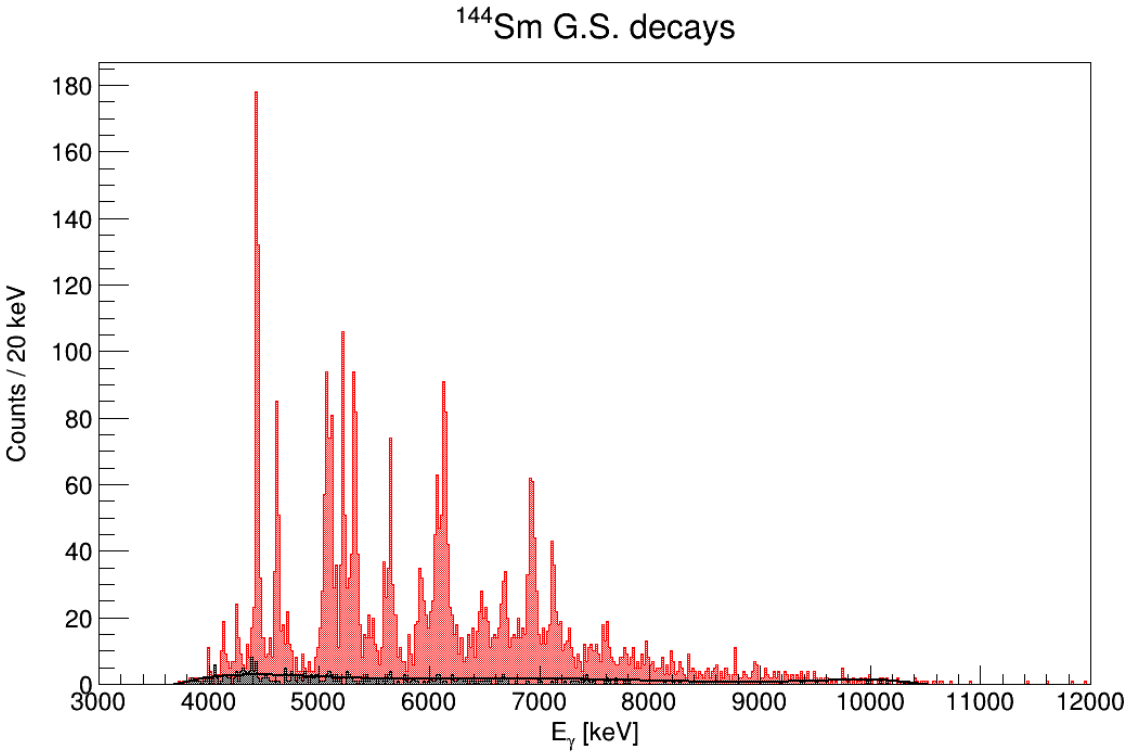


Figure 5.28: $^{144}$Sm ground state decay counts spectra with background.

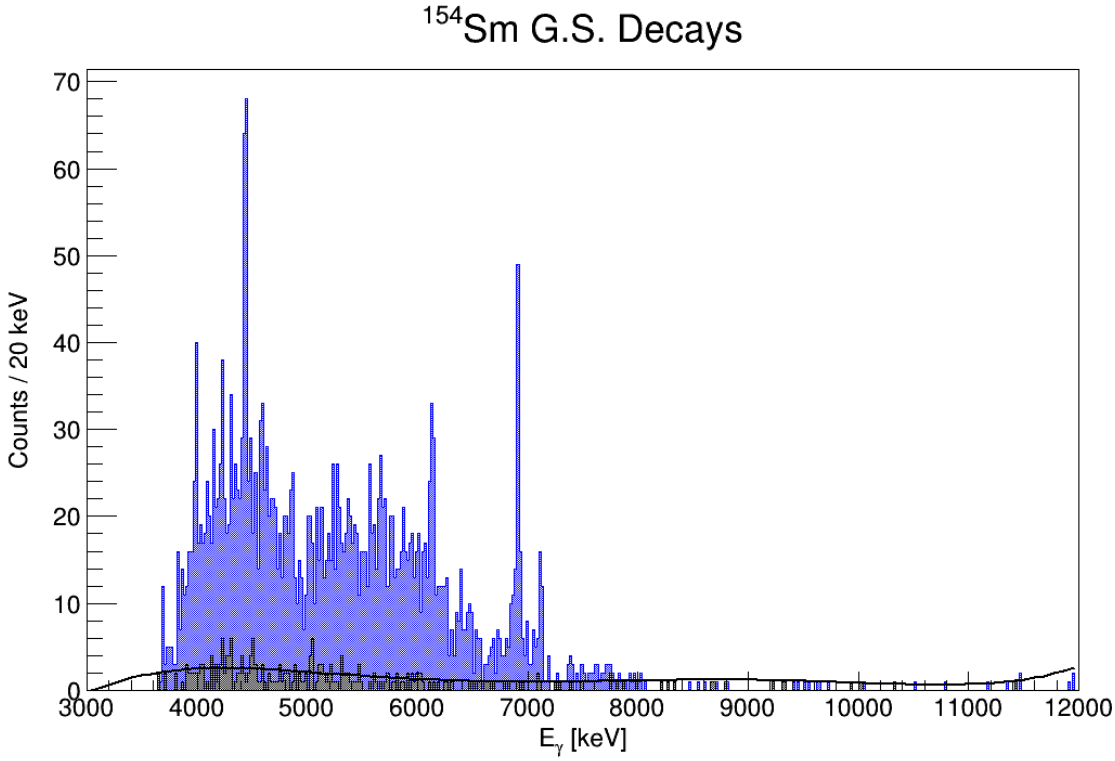


Figure 5.29: $^{154}$Sm ground state decay counts spectra with background.

## 5.5 Contaminant Subtraction

Peaks corresponding to $^{12}$C and $^{16}$O contaminants can be observed in both data sets. The oxygen contaminants arise since the targets undergo a certain amount of oxidation over time since when they were first prepared. In addition, trace amounts of lubricating gel are present in parts of the beam pipes and chambers that could lead to $^{12}$C contamination. The contaminant peaks were subtracted from the count spectra by fitting a gaussian + 1$^{\text{st}}$ order polynomial function over each peak and removing the counts falling within the gaussian area.

## 5.6 Cross Sections

The experimental cross section is determined from the background subtracted, ground state decay count spectra as detailed in this section. For a given excitation peak, the double differential cross section for the i$^{th}$ HPGe detector is determined using:

$$\frac{d^2\sigma}{d\Omega_\alpha d\Omega_\gamma} = \frac{A_i}{N_t N_\alpha \Delta\Omega_\alpha \Delta\Omega_{\gamma,i} \epsilon_{int,i}(E_\gamma) \epsilon_{K600} \Delta_{live}} \tag{5.20}$$

where $A_i$ = the area under the peak for detector i,
$N_t$ = number of target nuclei per unit area determined from the target thickness,
$N_\alpha$ = number of incident $\alpha$ particles determined from the charge integrated current,
$\Delta\Omega_\alpha$ = Opening angle of the K600 spectrometer,
$\Delta\Omega_{\gamma,i}$ = Opening angle of HPGe detector i,
$\epsilon_{int,i}(E_\gamma)$ = Energy dependent intrinsic efficiency of HPGe detector i,
$\epsilon_{K600}$ = Operational efficiency of the UX type VDC,
and $\Delta_{live}$ = Ratio of the live and measuring time events for the K600-BaGeL system.

All of the factors listed above and how they are obtained have been discussed in previous sections. The double-differential cross section is thus extracted from experimentally obtained

parameters only. The differential cross section is calculated from the double-differential cross section using:

$$\frac{d\sigma}{d\Omega_\alpha} = 4\pi \frac{\Gamma}{\Gamma_f} \frac{1}{W(\Omega_\gamma)} \frac{d^2\sigma}{d\Omega_\alpha d\Omega_\gamma} \tag{5.21}$$

$\frac{\Gamma}{\Gamma_f}$ is the branching ratio to the final state, assumed to be 1 for the purposes of this thesis as branching to excited states are not observed. Since small unobserved branchings could sum up to a considerable factor, this assumption provides only an upper limit for estimating the differential cross-section. $W(\Omega_\gamma)$ is the $\alpha$-$\gamma$ angular correlation which describes the angular distribution of the emitted $\gamma$-rays relative to the direction of the scattered $\alpha$ particle. A description of how the angular correlations are calculated was given in Chapter 3.

## 5.7 Multipolarity assessment

In order to asses the multipolarity of the states in the region of interest, the ratio in the counts between the in-plane detectors placed at different angles was compared to the calculated ratios deduced from the angular correlations computed in Chapter 3. The counts were corrected with the energy dependent efficiency functions ,$\epsilon_{int,i}(E_\gamma)$, of their respective detectors.

In Exp1, the angular comparison was performed between the 2 detectors at $\theta = 90°$ verses the 2 detectors at $\theta = 135°$. The projection with gate condition $|E_\gamma - E_x| = 200$ keV on the coincidence matrix, whereby decays to the the first excited state are fully included in the "ground state" decay band was employed. The efficiency corrected count spectra for the detectors at these angles are shown in Fig.5.30. Peaks corresponding to contaminants are labeled on the figure. The angular correlation computed in Chapter 3, for $^{154}$Sm is shown within the inset on the figure. The grey lines show the angular placement of the corresponding detectors, with the grey shaded areas indicating the full angular coverage of the detector faces. Distinct peaks among the $^{154}$Sm counts could not be identified due to the high state density, limiting detector resolution and limited statistics available.

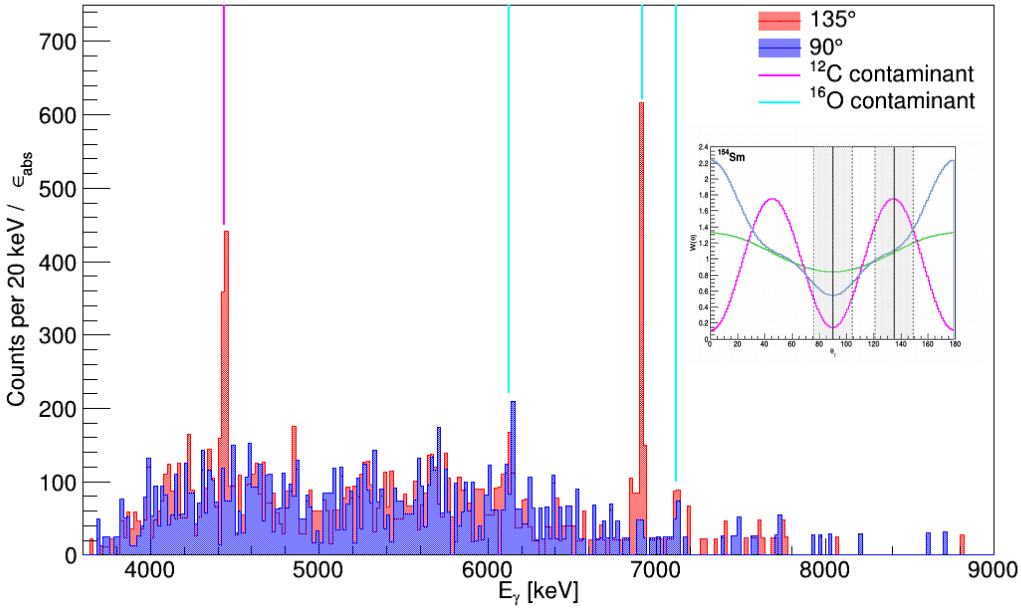


Figure 5.30: Comparison of counts corrected with efficiencies for detectors at $\theta = 90°$ and $\theta = 135°$ in Exp1

In Exp2, the angular comparison was performed between the 2 detectors at $\theta = 90°$ verses the 2 detectors at $\theta = 155°$. The projection with gate condition $|E_\gamma - E_x| = 110$ keV on the coincidence matrix, selecting transitions to the ground state was employed. The efficiency corrected count spectra for $^{144}$Sm, similar to Fig.5.30 for $^{154}$Sm, are shown in Fig.5.31, where peaks corresponding to contaminants are labeled and the angular correlation pattern is inset. Individual peaks that were distinct enough to compare the angular correlations for are indicated with an asterisk.

A ratio comparison between the counts at the two angles, for the 6 identified peaks in $^{144}$Sm are shown in Fig.5.32, while the ratio comparisons for counts integrated over the broad range of states for both $^{144}$Sm and $^{154}$Sm states are shown in Fig.5.33 and Fig.5.34 respectively.

The contribution to counts arising from the contaminants were excluded. The experimental error bars were computed accounting for the statistical error in the number of counts used for the integrated region before implementing the efficiency corrections. The central lines of the E1, E2 and E3 bands indicated on the figure show the mean expected ratio determined

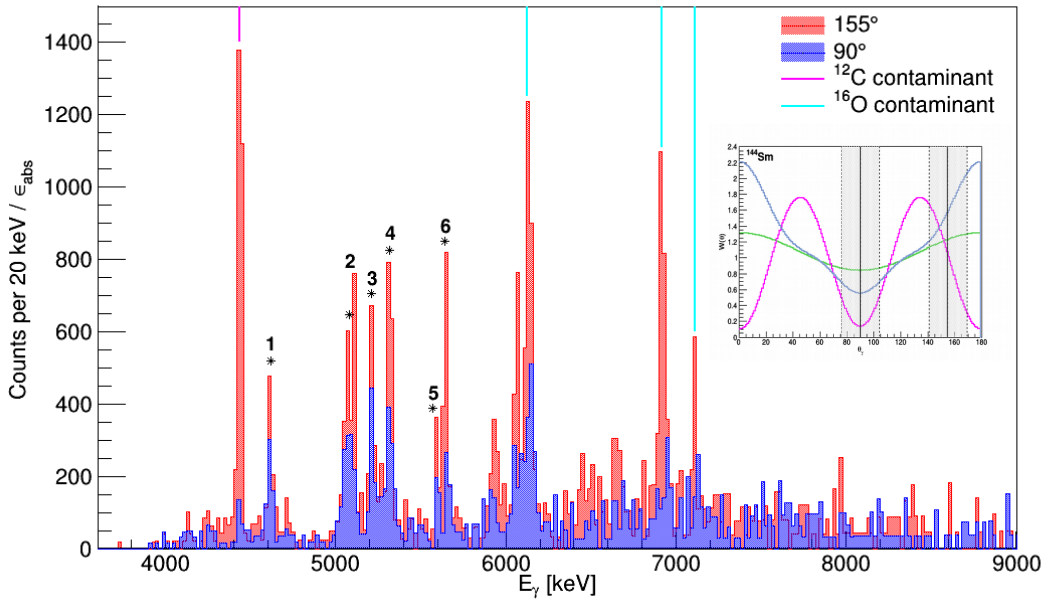


Figure 5.31: Comparison of counts corrected with efficiencies for detectors at $\theta = 90°$ and $\theta = 155°$ in Exp2

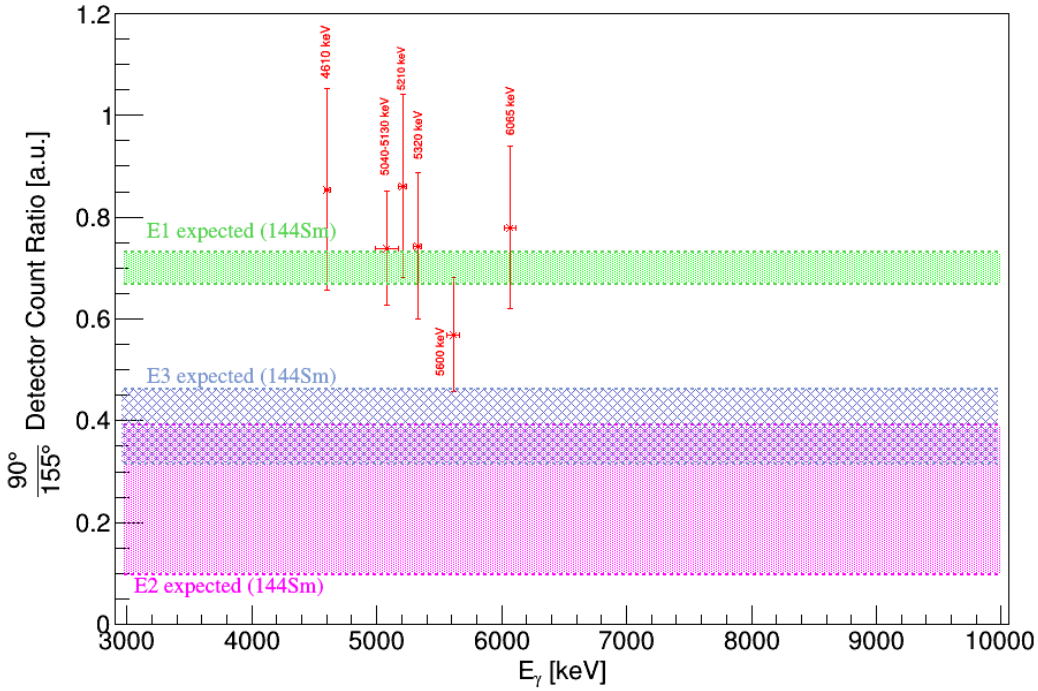


Figure 5.32: Multipolarity assessment for individual states in $^{144}$Sm

from the distribution of ratios for each angle increment over the full opening angle of the relevant Clover detectors. The upper and lower bounds of the bands come from the standard deviation in the distribution of ratio's.

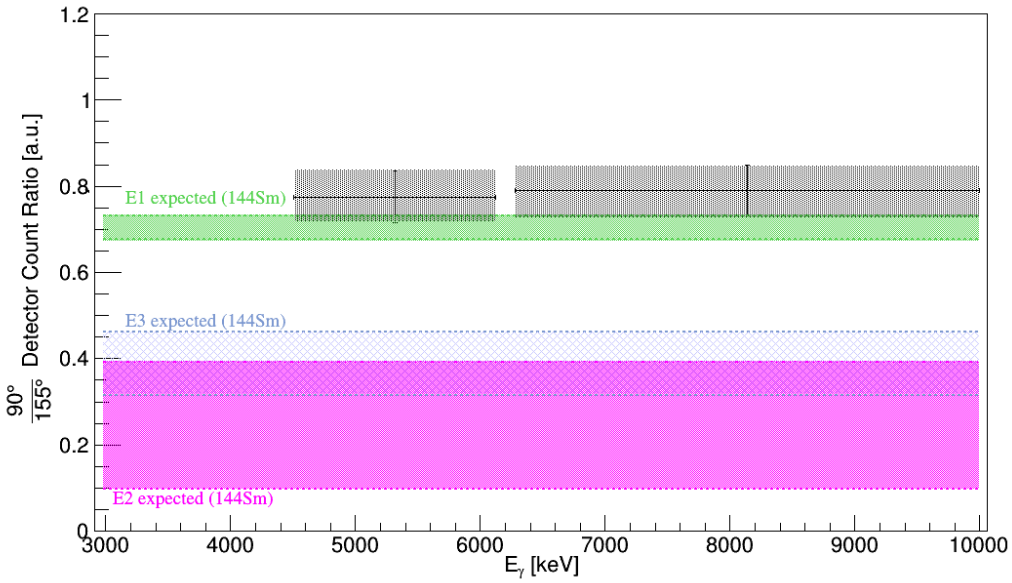


Figure 5.33: Multipolarity assessment for the broad range of states in $^{144}$Sm

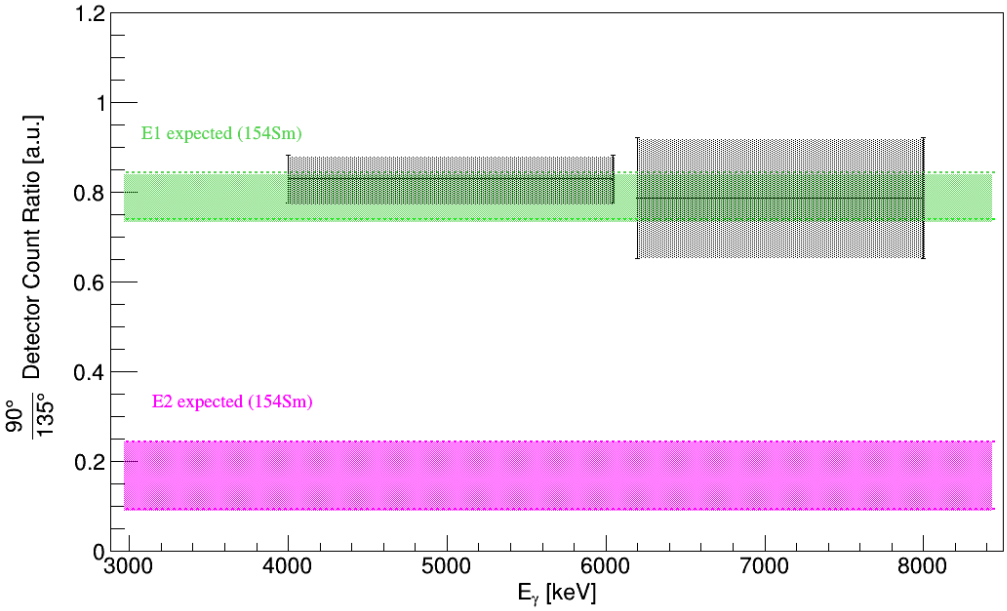


Figure 5.34: Multipolarity assessment for the broad range of states in $^{154}$Sm

The angular distribution ratios for both $^{144}$Sm and $^{154}$Sm indicate predominant E1 behaviour. In the case of $^{144}$Sm, the ratios sit slightly above the expected E1 band, however they are distinctly away from the E2 and E3 bands. In the energy region of interest, it is expected that contributions from transitions to the $2_1^+$ state should be small, whilst the contribution would increase with increasing energy. This could therefore account for why the ratio's appear more isotropic with increasing energy. A more isotropic behaviour would otherwise be indicative of E0 transitions, which would not be allowed for decays to a $0^+$ ground state.

To highlight the ability of this technique for deducing the multipolarity, known states in $^{24}$Mg, and the $^{12}$C and $^{16}$O contaminant peaks in the samarium spectra were assessed. The angular distribution ratios for states in $^{24}$Mg and the $^{12}$C and $^{16}$O contaminant peaks are shown in Fig.5.35 and Fig.5.36. These states show good correlation with their expected multipolarity behaviour. Thus it can be concluded that the states under investigation for the two Samarium isotopes show predominantly E1 behavior in the energy region of interest.

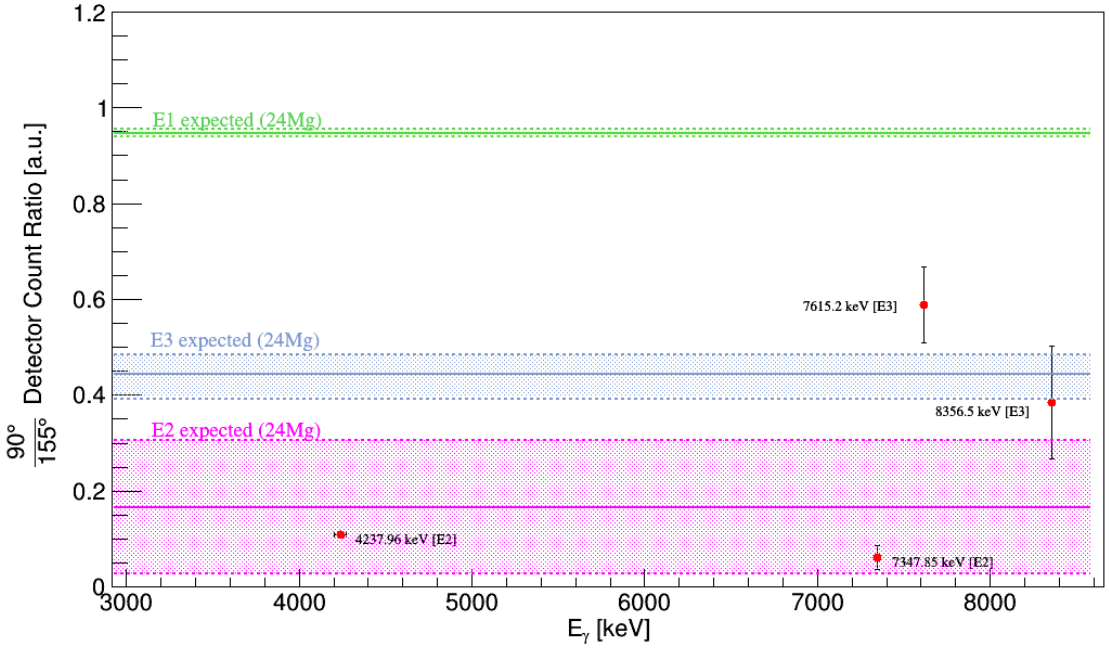


Figure 5.35: Multipolarity assessment for states identified in $^{24}$Mg

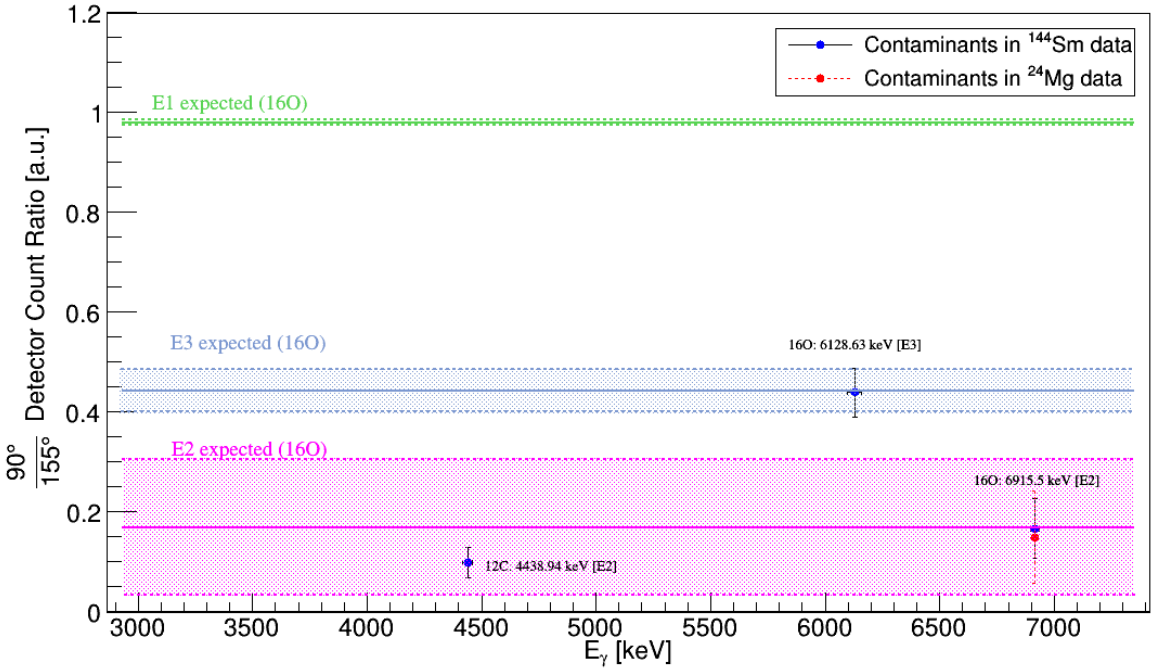


Figure 5.36: Multipolarity assessment of contaminant peaks

# Chapter 6

# Results and Discussion

The inelastic scattering experiments described in the previous two sections were performed for the purpose of comparing the cross section of $J^{\pi}=1^{-}$ excitations between $^{144}$Sm and $^{154}$Sm when probed with an isoscalar $\alpha-$particle. The aim was to compare the low-lying E1 isoscalar response between a spherical and deformed nucleus, to identify if a splitting behaviour similar to that seen in the GDR could be observed in the PDR.

The data analysis procedures for extracting the cross section were described in Chapter 5. A gate was applied to the coincidence matrix in order to select direct decays to the ground state. This was done because the PDR states of interest are characterised by a large branching to the ground state while states of higher multipolarity in the same excitation energy region tend to decay via intermediate excited states in the nuclei.

In this chapter, the experimental results of the extracted cross-sections are presented and discussed. A comparison between the spherical $^{144}$Sm and prolate deformed $^{154}$Sm is presented. Theoretical calculations performed to reproduce the isoscalar component of the PDR cross-section are compared to the experimentally obtained results. The results of each Samarium isotope are also compared to existing experimental data from $(\gamma, \gamma')$ and $(p, p')$ experiments.

## 6.1 Co-incidence matrix and extracted decay spectra

The coincidence matrix obtained from the $^{144}Sm(\alpha, \alpha'\gamma)$ experiments, zoomed into the area of interest for observing the PDR states is shown in the left panel of Fig. 6.1. The outer bounds of the gate selection, $|E_\gamma - E_x| \leq 110$ are indicated on the figure by the black lines. In the right panel is the projection of the $\gamma$-decays for the applied G.S. decay gate selection. The K600 full acceptance for the experiment as well as the neutron separation energy are indicated on the plot. Peaks that correspond to the $^{12}$C and $^{16}$O contaminants are also indicated. From the count spectra, a number of states concentrated in peaks can be observed for $^{144}$Sm, particularly in the lower energy region between 4.5-7 MeV where the PDR states are anticipated.

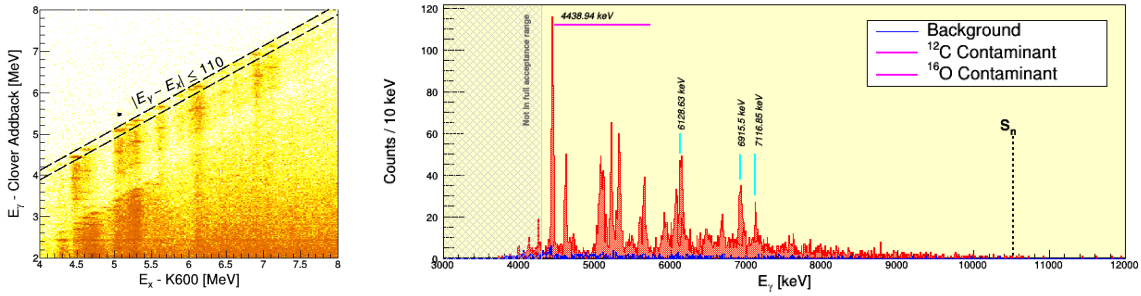


Figure 6.1: $^{144}$Sm co-incidence matrix and direct decay projection

The coincidence matrix obtained from the $^{154}$Sm$(\alpha, \alpha'\gamma)$ experiments, zoomed into the area of interest for observing the PDR states is shown in the left panel of Fig. 6.2. In the right panel, in green is the projection of the $\gamma$-decays for the applied G.S. decay gate selection, $|E_\gamma - E_x| \leq 100$. A projection with the broader cut that fully encompasses all the ground state decays and decays to the first excited state is shown in blue. The K600 full acceptance for the experiment as well as the neutron separation energy are indicated on the plot. Peaks that correspond to the $^{12}$C and $^{16}$O contaminants are also indicated.

The motivation for including fully the decays to the first excited for $^{154}$Sm arose due to the

inability to distinguish the two decay bands with the present energy resolution since the first excited state occurs at 81.981 keV. Furthermore, while the direct $\gamma$-decay to the ground state contributes to a bulk portion of the total PDR strength, a portion of these states can decay to other low-lying states. Nuclear resonance fluorescence experiments performed on $^{140}$Ce, using a linearly polarized quasi-monoenergetic photon beam at the High Intensity $\gamma-$ray Source [54], investigated the direct decay of dipole states to low-lying states. The results showed a 10% mixing of the PDR built on the first excited $2_1^+$ state. The multipolarity of the states in the broad decay cut selection were assessed and showed behaviour of E1 character.

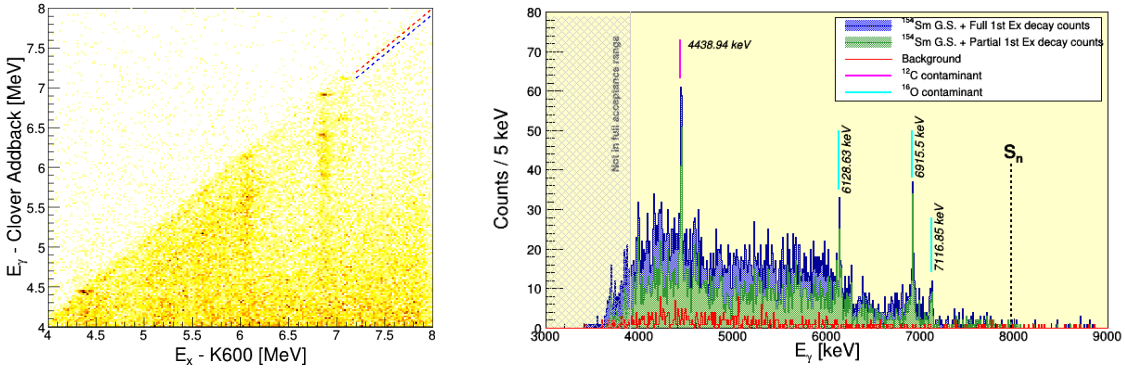


Figure 6.2: $^{154}$Sm co-incidence matrix and direct decay projection

## 6.2 $^{144}$Sm vs $^{154}$Sm

A comparison of the differential cross sections obtained from the $(\alpha, \alpha'\gamma)$ experiments performed for this study is shown in Fig. 6.3. The cross section for direct $\gamma$-decays to the ground state in the spherical $^{144}$Sm is shown in the upper panel. The cross-section for the prolate deformed $^{154}$Sm case is shown in the lower panel, for $\gamma$-decays to the ground state and to the 1st excited state. The cross-sections are presented using bin widths of 100 keV.

The multi-polarity assessment presented in Chapter 5 confirmed that the states observed in Fig. 6.3 are predominantly of E1 character. In $^{144}$Sm, distinct peaks are evident in the lower

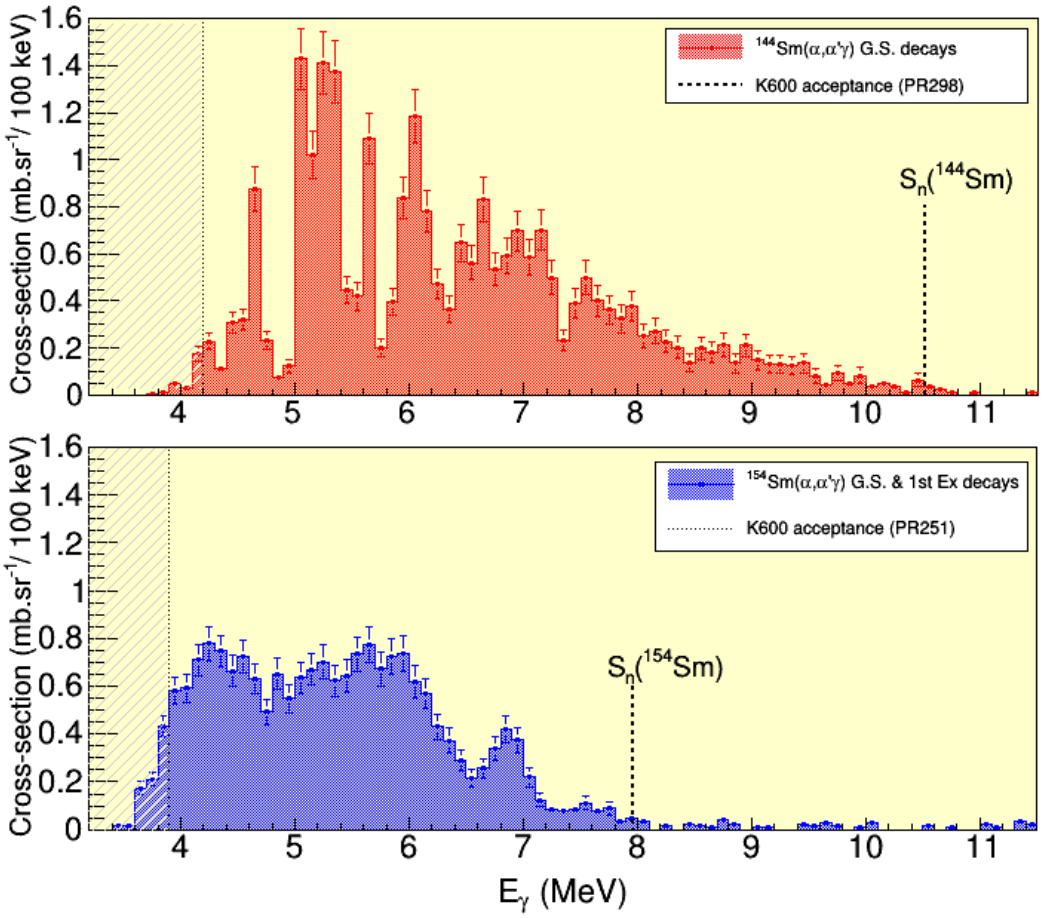


Figure 6.3: $^{144}$Sm Vs $^{154}$Sm Cross-sections

energy region between 4.5-6.5 MeV. The strength of the response appears to significantly taper down thereafter in the higher energy region between 7.5 MeV and the $S_n$ threshold. In $^{154}$Sm, the states appear more evenly spread indicating increased fragmentation of the PDR strength. The strength is concentrated between 4-6.5 MeV, and completely falls away around 7.2 MeV. It should be noted that the experimental set-up was sensitive enough to detect the E1 $^{16}$O contaminant peak at 7.115 MeV, thus the lack of strength between 7 MeV up until the neutron separation threshold at 7.966 MeV is not due to a lack of sensitivity. Rather, excitement of the lower energy region is typically observed for the isoscalar response of the PDR [17].

A general observation of the PDR response from both photonuclear and $(\alpha, \alpha'\gamma)$ experiments

as well as theoretical investigations in the N=82 isotones [17] indicates that a reduction in the proton-neutron asymmetry leads to the PDR being located at higher energy. However, it also leads to a reduction in overall strength. This is further demonstrated in calculations performed using the RHB+RQRPA model with DD-ME2 plus Gogny D1S interactions, for the Sn, Te and Xe isotopic chains [15]. In these calculations, an increase in neutron excess resulted in a shifting of the peak energy and an increase in summed strength. Unfortunately, due to the limitation imposed by the positioning of the K600 focal plane detectors, PDR strength at energies below the full acceptance threshold could not be compared for the two isotopes.

With the commonly used picture of the PDR being interpreted as an oscillation of the saturated core against the neutron skin, one would expect the PDR to exhaust more strength in $^{154}$Sm owing to its 10 extra neutrons. Furthermore, $^{144}$Sm has a closed N=82 neutron shell while in $^{154}$Sm the neutrons in the outer orbitals would be more loosely bound. Thus, the restoring force in the oscillation of skin against core should become weaker, leading to an increase in PDR strength. In the experimental results obtained however, the total measured strength from the direct decay is hindered in comparison to that for $^{144}$Sm.

The effect of the interplay between increasing neutron number versus deformation on how strongly the PDR response presents itself cannot be decoupled from the current experiments data alone. The contribution from statistical decays via intermediate states needs to be taken into account, and a comparison to investigations with other probes as well as theoretical predictions is necessary. Through using the $(\alpha, \alpha'\gamma)$ method however, PDR strength was populated in both Samarium isotopes.

## 6.3 Theoretical Modelling

In order to model the inelastic $\alpha$ scattering cross-section for direct comparison to the experimental quantities obtained, calculations were performed within the framework of a semi-classical model using microscopic transition densities. This model makes the assumption that colliding nuclei move along classical trajectories, whilst treating the internal

degrees of freedom quantum mechanically. For the $^{144}$Sm case, the internal structure of the colliding nuclei was deduced using the Relativistic Quasiparticle Time Blocking Approximation (RQTBA) [33] approach. For $^{154}$Sm, transition densities were obtained using a deformed Hartree-Fock Bogoliobov coupled to quasiparticle random-phase approximation (HFB+QRPA) [13] approach. Details of the calculations were described in Chapter 3. For both calculations, the GDR of each respective nuclei could be predicted very well and thus the predictions for the low-energy dipole strength are assumed to be reliable too.

### 6.3.1 $^{144}$Sm

The RQTBA approach used for the $^{144}$Sm calculation is an extension of the self-consistent relativistic quasiparticle random-phase approximation (RQRPA), incorporating the quasiparticle-phonon coupling (QPC) model. It allows for investigating the effect of coupling two-quasiparticle excitations to collective vibrations within a fully consistent calculation scheme based on covariant energy density functional theory [33]. This framework has been used to calculate dipole spectra for several even-even spherical nuclei, for example $^{124}$Sn which have shown good agreement with experimental photo absorption cross-sections.

The proton and neutron transition densities of the strongest state in the RQTBA prediction at 6.8 MeV is shown in figure 6.4. The typical picture expected for the PDR is observed, where the protons and neutrons are in phase while neutrons dominate at the surface.

Figure 6.5 shows the comparison between the experimental and theoretical cross-sections for the $^{144}$Sm$(\alpha, \alpha'\gamma)$ reaction. The theoretical cross-section was normalised to the solid angle of the experiment in order to make it directly comparable to the differential cross-section measured. The strength is much more fragmented in the experiment compared to the RQTBA prediction, where almost a third of the total strength is contained in the peaks at 7 MeV. This could be because the RQTBA cuts off the coupling for states with more complex than 2q-phonon configurations and also limits the phonon space to only low lying modes. Whilst the RQTBA performs better at reproducing fragmentation compared to the QPM model, coupling to more complex configurations needs to be included in order to obtain a state-by-state description of the PDR that is more comparable with experimental data.

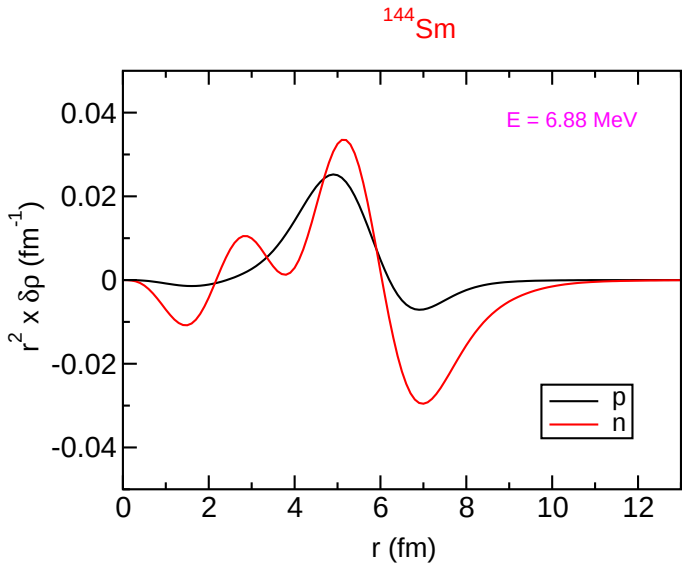


Figure 6.4: RQTBA predicted proton and neutron transition densities for the dipole state at 6.88 MeV in $^{144}$Sm

The effect of including the higher order couplings is expected to augment the fragmentation towards lower energies.

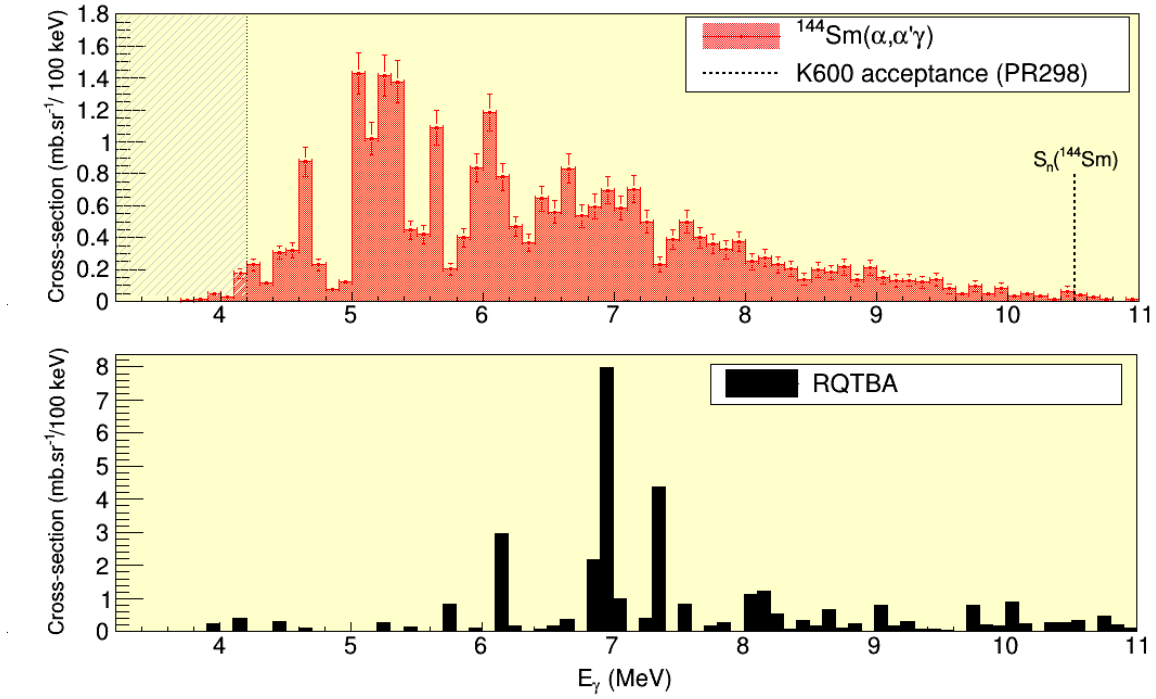


Figure 6.5: Comparison between measured and calculated cross sections for $^{144}$Sm

The cumulative sums of the RQTBA and measured $(\alpha, \alpha'\gamma)$ cross sections are shown in Fig. 6.6. The lack of fragmentation is observed in the stepped appearance for theory as compared to the gradual accumulation for the experiment, however the accumulated strengths appear relatively on par until 7.2 MeV. In the higher energy region, the theory predicts slightly more strength. The total integrated strength between 4.3 MeV (experimental energy threshold) and 10.5 MeV (nuetron seperation energy threshold) in the experiment is $24.3 \pm 3.8$ mb/sr, whilst theory predicts 29.6 mb/sr. This deviates by approximately 15%. Since the experiment measures only the direct decay channel, the statistical decay contribution which is observed to increase with increasing energies may account for this small discrepancy.

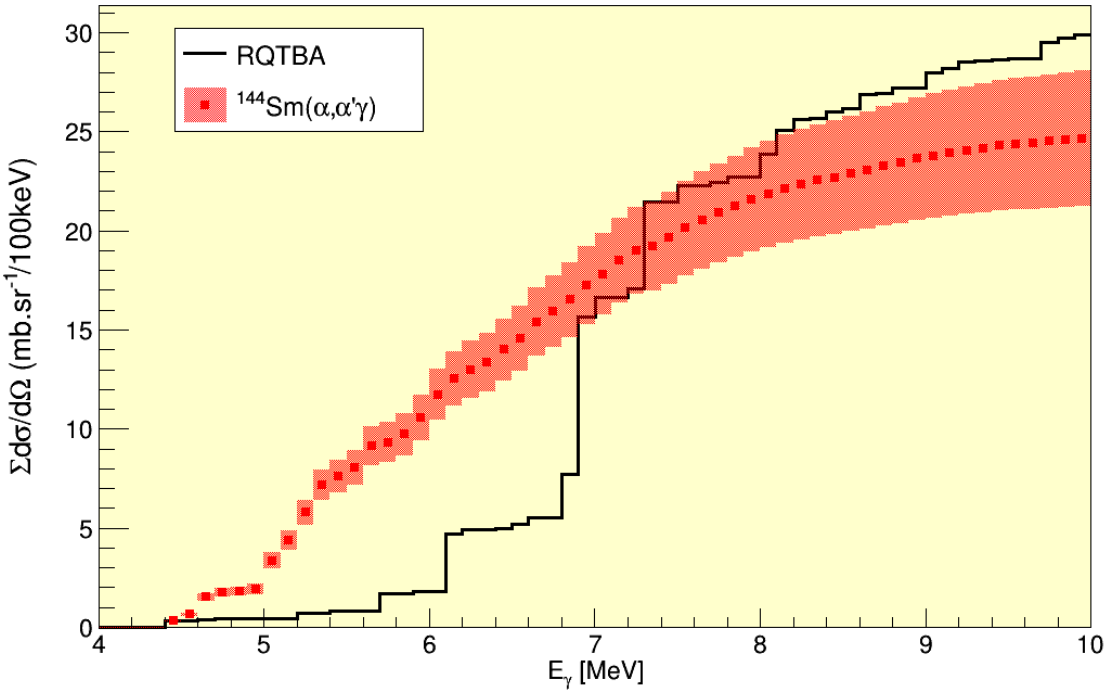


Figure 6.6: Comparison between the experimental extracted and theoretical calculated summed cross-sections for $^{144}$Sm.

### 6.3.2 $^{154}$Sm

For $^{154}$Sm, transition densities obtained using a deformed Hartree-Fock Bogoliobov coupled to quasiparticle random-phase approximation (HFB+QRPA) [13] approach were used. A descriptive detail of the microscopic model used were presented in Chapter 2. This model

reproduces characteristics of the GDR, particularly the isotopic dependence of the broadening and splitting in the GDR extremely well. The proton and neutron transition densities calculated for a K=0 at dipole state at 7.47 MeV and a K=1 dipole state at 8.73 MeV are shown in figure 6.7. The transition densities calculated show predominant isoscalar behaviour, with the protons and neutrons in phase with each other. The neutrons dominate at the surface from around 7 fm, although a small contribution from the protons is still observed. These transitions densities thus reflect the behaviour typically observed for the PDR.

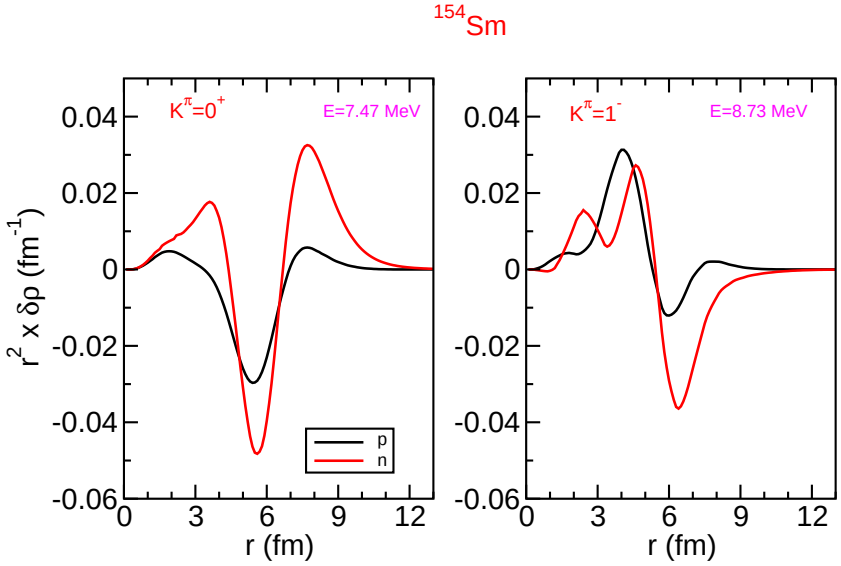


Figure 6.7: Deformed HFB+QRPA predicted proton and neutron transition densities for the K=0 and K=1 dipole states at 7.49 MeV and 7.33 MeV respectively in $^{154}$Sm

A comparison between the experimental and theoretical cross-sections for the $^{154}Sm(\alpha, \alpha'\gamma)$ reaction is shown in Figure 6.8. The K=0 and K=1 contributions to the total predicted cross-sections are highlighted in red and green in the bottom two panels respectively. In the theoretical prediction, a splitting between a lower energy component below 6.2 MeV, and a higher energy grouping of states between 7-10 MeV is observed. The low energy component shows predominant K=0 behaviour whilst the weaker high energy component has a mixed behaviour. Between 7-8 MeV, it is mixed but after 8 MeV mostly K=1 states occur.

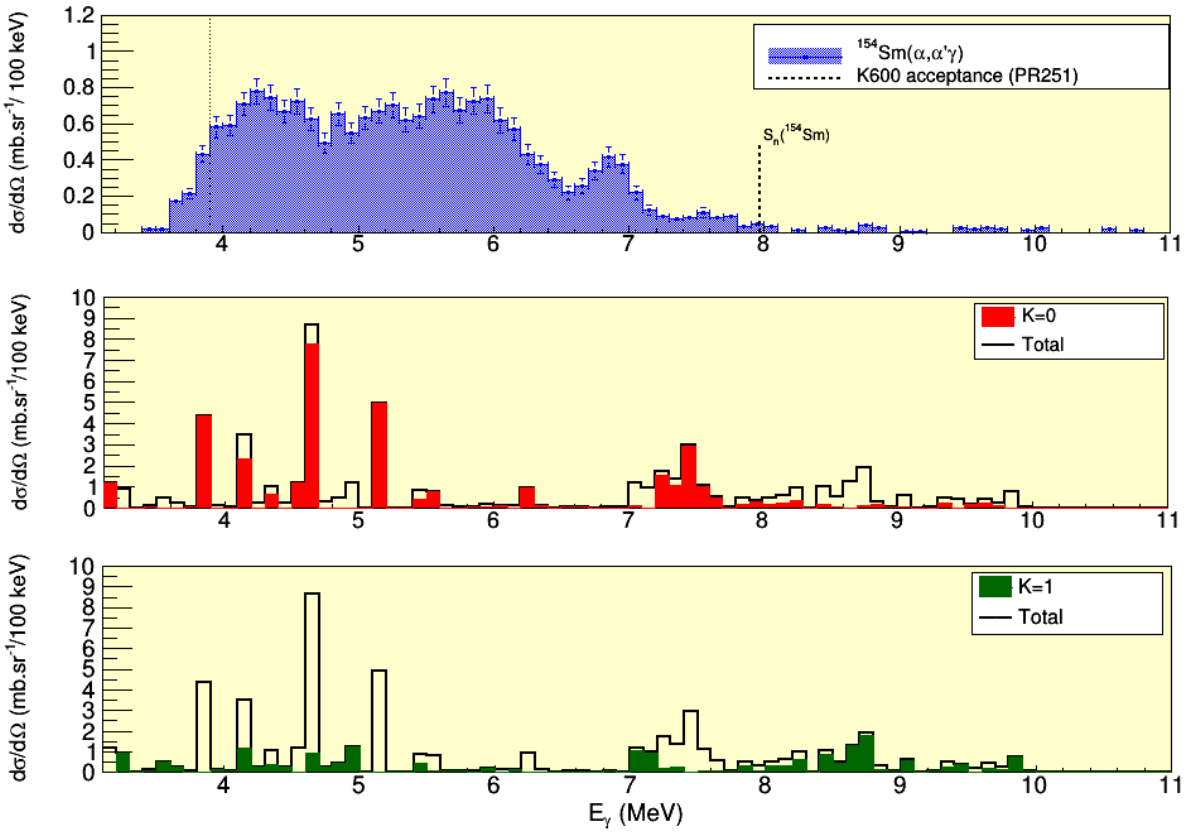


Figure 6.8: Comparison between measured and calculated cross sections for $^{154}$Sm

Due to the experimental limitations, the cross-section could only be measured between 4.2 MeV and the neutron separation energy at 7.89 MeV. Thus the higher energy component could not be measured, although no evidence for strength between 7-8 MeV is observed in the experiment. The small "peak" observed just below 7 MeV might be linked to the high energy component, however it is also likely that a residual contribution from the $^{16}$O contaminant peaks may be present. The contribution for contaminant peaks that were subtracted from the count spectra, were deduced by fitting a gaus + 1st order polynomial function with the centroid fixed at the observed peak. This was done conservatively in order to prevent the subtraction of potential $^{154}$Sm states, however it is possible for the contribution to have been underestimated.

Directly comparing the theoretical predictions to the experimental cross-sections, a larger cross-section with more concentrated states is calculated whereas the states are much more

fragmented in experiment. The deformed HFB+QRPA does not include coupling to complex configurations, however part of the mode-mode couplings to low-lying collective modes is implicitly included due to the deformation and high level density when describing the QRPA states. Hence a strong fragmentation is already produced, although inclusion of higher order coupling effects would improve this further.

The cumulative sums of the calculated and measured $(\alpha, \alpha'\gamma)$ cross sections are shown in Fig. 6.9. The total cumulative experimental cross-section between 4-7 MeV is $17.9 \pm 1.8$ mb/sr whilst theory predicts 25.6 mb/sr. In the region between 4-8 MeV, the total cumulative experimental cross-section is $18.8 \pm 2.1$ mb/sr compared to 36.3 mb/sr predicted by theory. This shows a 30% and 48% discrepancy across the two considered energy regions respectively.

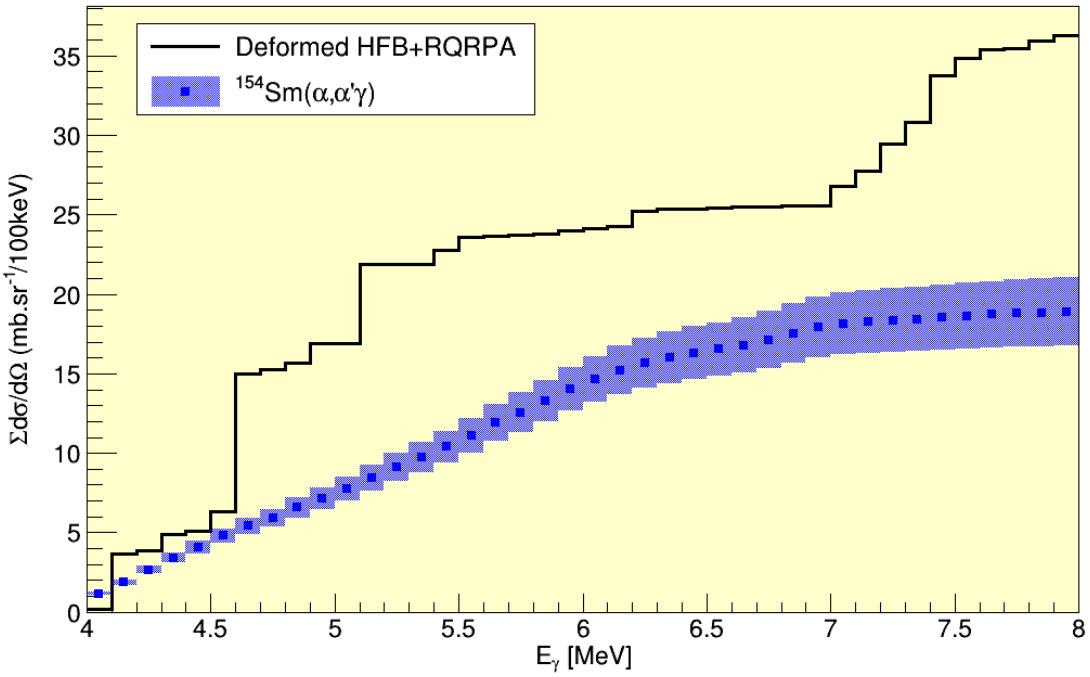


Figure 6.9: Comparison between the experimental extracted and theoretical calculated summed cross-sections for $^{154}$Sm

Again it should be highlighted that in the experiment, only the direct decays to the ground state and to the $1^{st}$ excited state are measured. The contribution from the statistical decay component is not accounted for. Very recently, results from $\gamma, \gamma'\gamma''$ NRF experiments on $^{66}$Zr [55], in which they investigated the contributions to the total photo-absorption cross-

section of both the direct decay channel as well as from decays cascading to low-lying states, have been published. In these results, the average ground state branching ratios for states lying between 5-8 MeV ranged around 0.6-0.8 and showed a decreasing trend with increasing energy further than 8 MeV.

Similar experiments were performed on prolate deformed nuclei $^{156}$Gd [30] and $^{164}$Dy [29], although due to the first excited state lying so low in energy, the contributions between direct decays to the ground state and 1st excited state could not be fully decoupled. Instead, population ratios were computed, which gauge the ratio of all decay chains originating from the photo-excitation excitation to a given low-lying state relative to the direct decay to the ground state and $1^{st}$ excited states. For states in the energy range 5.8-7.4 MeV, population ratios for the $2_1^+$ state ranged between 1.18-2.85 and for the $2_2^+$ ranged between 0.6-1.4. An increasing trend in the ratio with increasing energy was observed as well. These results show that the statistical decay component carries a significant contribution of the PDR strength and could account for the large discrepancy between the cross-sections measured with those calculated by the deformed HFB+QRPA model. This would also account for why the cross-sections measured for $^{144}$Sm is larger than that of $^{154}$Sm, whilst the theoretical models predict that $^{154}$Sm should have the larger cross-section.

## 6.4 $(\alpha, \alpha'\gamma)$ vs $(\gamma, \gamma')$

In Fig. 6.10, a comparison between the experimental $^{144}Sm(\alpha, \alpha'\gamma)$ cross section (upper panel) and the measured B(E1) strength from $^{144}Sm(\gamma, \gamma')$ measurements [56] (lower panel) is shown. In the photon scattering measurements, two experiments with bremsstrahlung photon beams of end-point energies at 7.65 MeV and 9.9 MeV were performed. The scattered photons were then measured with two HPGe detectors positioned at 90° and 130°. Due to the experimental sensitivity of the set-up however, only states up to 7 MeV were considered. It should also be noted that the B(E1) values of the states are for strength concentrated in peaks only, whilst the $(\alpha, \alpha'\gamma)$ cross-sections include the unresolved strength measured.

From a general observation, states across a similar region where the PDR response is ex-

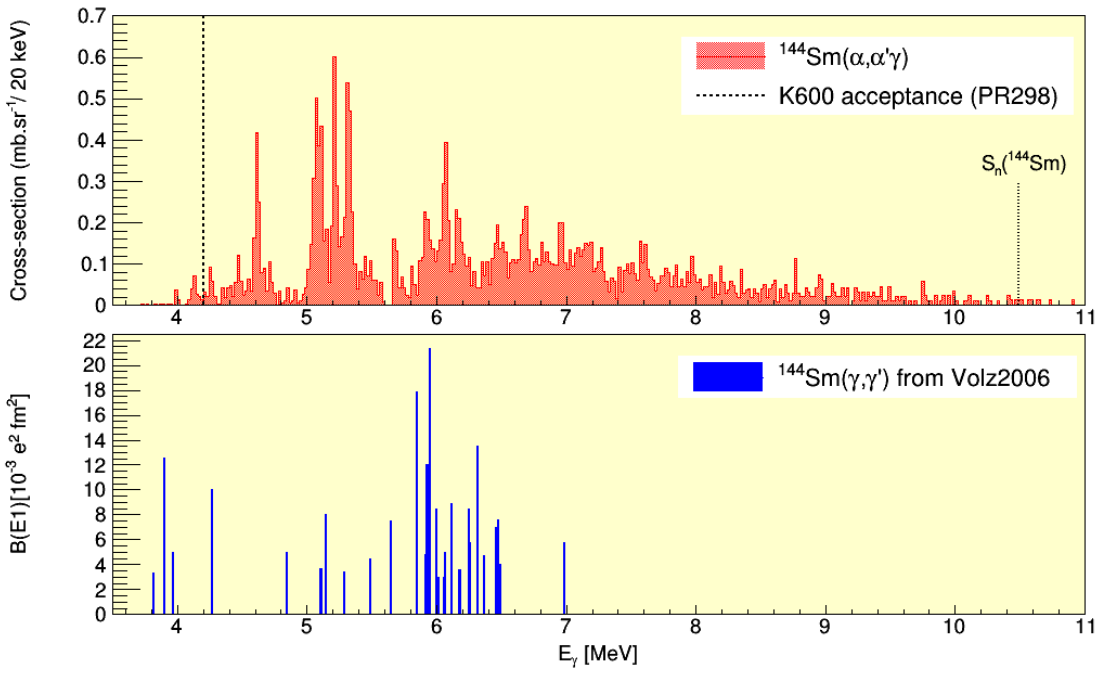


Figure 6.10: Comparison of PDR states observed $^{144}$Sm measured using the $(\alpha, \alpha'\gamma)$ reaction channel in this study vs the $(\gamma, \gamma')$ reaction channel measured in [56]

pected are seen with both probes. The grouping of states between 5.8-6.5 MeV appear relatively strongly excited in both experiments. The bunch of states between 5-5.6 MeV are much more enhanced in the $(\alpha, \alpha'\gamma)$ response as opposed to the $(\gamma, \gamma')$ reaction channel. Whilst a new state in the vicinity of 4.6 MeV is observed with the $\alpha$ probe.

The difference in the responses is a result of the properties of the probes as described in Chapter 2 and the isospin characteristics of the individual states. The $\alpha$ probe is a hadronic probe that interacts predominantly at the surface of the nucleus for the bombarding energy used in the experiment. Whilst the $\gamma$ probe interacts electromagnetically with the nucleus as a whole. The two probes investigate different parts of the transition densities of the PDR states. Thus small differences in the transition density can be enhanced in a different way regarding the strength extracted with the two probes.

In the $^{144}Sm(\alpha, \alpha'\gamma)$, the strength is clearly suppressed in the higher energy region after 7 MeV as has been observed for other N=82 isotones in $(\alpha, \alpha'\gamma)$ at small scattering angles

[22]. This characteristic is identified as isospin splitting of the PDR, where the selectivity of the probe is to the isoscalar response of the PDR.

## 6.5 $(\alpha, \alpha'\gamma)$ vs $(p, p')$

In relativistic proton scattering experiments, the photo absorption cross section can be extracted by means of the virtual photon method. An advantage of this technique lays in the possibility to extract the excitation cross section without being affected by the branching ratio of the gamma decay. For the case of $^{154}$Sm, an experiment using a polarised proton beam was performed at RCNP (Japan) [12]. and the electric dipole cross section in the excitation energy region 5-19 MeV was extracted using the method of polarization transfer observables. The results of this experiment are shown in Fig. 6.11 where the photoabsorption cross section for $^{154}$Sm is depicted.

In their study, the GDR was fitted with two Lorentzians showing a good agreement with the data. The bottom panel shows a zoom in of the PDR region where the strength is reported as subtraction of the GDR fitted Lorentzians. The subtracted strength shows a structure consisting of two bumps with centroids at 5.9 MeV and 7.8 MeV which they assigned to the PDR. Considering that the the energy ratio of the two bumps was about the same as in the GDR region, where a splitting of the resonance structure with respect to their K quantum number occurs, the authors suggested the possibility that the PDR might also show a splitting with K.

Comparing the results of proton scattering to the response measured in this study, the low energy peak located at around 5.9 MeV is excited in both reactions while no strength above 7 MeV is observed for the alpha scattering case. Even though the statistical decay would contribute more to the high energy part of the strength than an isoscalar probe is expected to see, according to the Alaga rule, an increase in the direct decay to the ground state when compared with the low-energy part is expected if the K-splitting is present and the higher energy part is associated to the K=1 component while the lower part is assigned to the K=0 component.

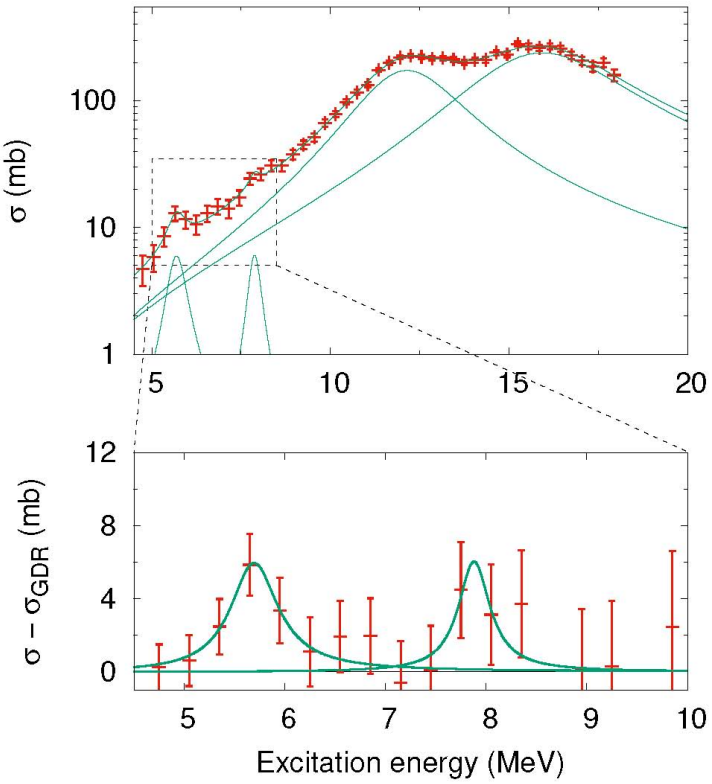


Figure 6.11: Electric dipole cross-section obtained in $^{154}$Sm(p,p') experiments at RCNP [12]

Even though the sensitivity of our setup allows the measurement of high-energy gamma rays up to the particle threshold, no strength is observed above 7 MeV. The splitting observed when comparing the isovector strength extracted from the proton scattering experiment and the isoscalar strength obtained from alpha scattering seems to be related to what is called the "PDR isospin splitting" already observed for this excitation more in several other nuclei with spherical symmetry.

# Chapter 7

# Conclusions

The field of PDR studies has shown to be a very promising line of research towards the understanding of nuclear correlations and the occurrence of collective modes in the many-body nuclear environment owing to the complex structure involved. The low-lying dipole strength has been experimentally observed in different mass regions of the nuclear chart in nuclei with a neutron excess. The presence of these states in the electric dipole response has been corroborated with calculations employing different theoretical models.

As highlighted in Chapter 2, the prediction of this mode in both the isovector and isoscalar electric dipole response enabled complementary studies of the PDR with different probes, and a clear splitting of the populated states involved were observed, thereby accentuating the distinct isospin mixed nature of these states. Mostly nuclei with spherical symmetry have been investigated leaving the question on the role of deformation unresolved. The work performed in thesis therefore aimed to address this point.

In investigations of the GDR in deformed nuclei, a splitting of the response into two peaks corresponding to the out-of-phase oscillation of neutrons against protons along and perpendicular to the symmetry axes were observed (K-splitting) [8, 9]. Since the PDR has been interpreted as an out-of-phase oscillation of the neutron excess against a proton plus neutron core [1], one might expect the same mechanism to hold true thereby leading to a splitting of the low-lying dipole response into two bumps.

A few recent studies using $\gamma$-probes at the HI$\gamma\gamma$S facility attempted to investigate the PDR in the deformed nuclei $^{76}$Se [26], Xe and Mo isotopic chains [27], $^{164}$Dy [29] and

$^{156}$Gd [30], although clear evidence for a splitting effect was not observed for the PDR built on the ground state. Preliminary (p,p') studies on the deformed $^{154}$Sm performed at the Research Center for Nuclear Physics (RCNP) [11, 12] however, showed potential evidence for a splitting in the PDR response similar to the K-splitting observed in the GDR.

In this work, inelastic scattering experiments using the $\alpha-$particle as a probe were performed to investigate, for the first time, the role of nuclear deformation in the isoscalar response of the Pygmy Dipole Resonance (PDR). The aim was to compare the cross section of these low-lying $J^{\pi}=1^{-}$ excited states between the spherical $^{144}$Sm and axially deformed $^{154}$Sm isotopes, to identify if a splitting behaviour similar to that seen in the GDR could be observed in the PDR.

The experiments performed at iThemba LABS, were the first of their kind to couple the K600 magnetic spectrometer with an array of gamma-detectors. Alpha particles accelerated to 120 MeV impinged the Sm targets and the inelastically scattered particles were momentum analyzed by the K600 magnetic spectrometer placed in the zero-degree configuration. The corresponding $\gamma$-decay was detected by a combined system of HPGe and $LaBr_3$:Ce detectors. The $\alpha - \gamma$ coincidence technique was used to obtain the cross section for the population of the pygmy states. The intricate data-extraction process was detailed in Chapter 5. In both nuclei, the region of the PDR was excited and the E1 multipolarity of the transitions was confirmed by the angular correlation between the $\alpha$-particles and the co-incident $\gamma$-rays.

The total exclusive cross section measured for $^{144}$Sm amounted to $24.3 \pm 3.8$ mb/sr while for $^{154}$Sm to $18.8 \pm 2$mb/sr. For the spherical $^{144}$Sm nucleus the strength observed was more concentrated in distinct transitions when compared with the $^{154}$Sm. In the deformed case, the response did not show any clear peak but rather an overall smooth fragmentation. The PDR was found to be in the energy range 4-8 MeV for $^{144}$Sm and 4-7 MeV for $^{154}$Sm, although the study of the lower part of the strength was limited by the energy acceptance of the spectrometer. A distinct splitting in the response was not observed.

The experimental results were compared with the prediction of the RQTBA and the deformed HFB+QRPA theories, respectively. The theoretical cross sections were extracted

within a semiclassical coupled-channel approach. Even though the fragmentation observed in the experiment for the $^{144}$Sm was underestimated by the calculations, a good agreement with the total cross section measured was found. This was not the case for the deformed $^{154}$Sm, where the experimental cross section accounted for only 52% of the predicted cross section in the same excitation region. This considerable discrepancy is related to the assumption that the pygmy dipole states decay predominantly to the ground states and only a small branching ratio via high-lying states. The high-level density of this deformed nucleus and the increasing degree of complexity of the higher lying states makes the contribution from statistical decay no longer negligible. This tendency was observed also in the HI$\gamma\gamma$S experiments on the deformed $^{156}$Gd [30] and $^{164}$Dy [29] nuclei.

An attempt to investigate the presence of a K-splitting in the PDR for $^{154}$Sm using the Alaga rules was also made in this study. However, due to the close proximity of the first excited state located at 82 keV and experimental limitations in the energy resolution, a discrimination between the direct ground state and the first excited state decay could not be achieved. Instead, the isoscalar response extracted in this thesis was compared with the isovector strength obtain from the (p,p') experiment performed at RCNP using the relativistic proton scattering at forward angles. The double bump observed in the isovector channel was not found in the case of the isoscalar strength. The difference obtain between these two experiments is therefore related to the "isospin splitting" of the PDR rather than a splitting of the strength connected with the K quantum number.

The results of this thesis have highlighted the need for future studies on deformed nuclei to include improved detection resolution capabilities so that a better distinction between the ground state and first excited state decays can be achieved. This will allow to probe the validity of the Alaga rule in this excitation and further comment on the K-splitting. An experiment is now planned to measure the photoabsorption cross section of $^{154}$Sm using the high resolution $\gamma$-beam at the HI$\gamma\gamma$S facility for further investigation of this deformed nucleus. The extracted inelastic cross-section will also be compared with statistical model predictions in order to account for the statistical decay contribution to the PDR response.

Investigations of the PDR in additional deformed nuclei would be highly beneficial for establishing a better picture into the general properties of this low lying dipole mode.

# References


1. Mohan, R., Danos, M. & Biedenharn, L. C. Three-Fluid Hydrodynamical Model of Nuclei. *Phys. Rev. C* **3,** 1740–1749. https://link.aps.org/doi/10.1103/PhysRevC.3.1740 (5 May 1971).

2. Suzuki, Y., Ikeda, K. & Sato, H. New Type of Dipole Vibration in Nuclei. *Progress of Theoretical Physics* **83,** 180–184. ISSN: 0033-068X. eprint: https://academic.oup.com/ptp/article-pdf/83/2/180/5383961/83-2-180.pdf. https://doi.org/10.1143/PTP.83.180 (Feb. 1990).

3. Roca-Maza, X. *et al.* Electric dipole polarizability in $^{208}$Pb: Insights from the droplet model. *Phys. Rev. C* **88,** 024316. https://link.aps.org/doi/10.1103/PhysRevC.88.024316 (2 Aug. 2013).

4. Carbone, A. *et al.* Constraints on the symmetry energy and neutron skins from pygmy resonances in $^{68}$Ni and $^{132}$Sn. *Phys. Rev. C* **81,** 041301. https://link.aps.org/doi/10.1103/PhysRevC.81.041301 (4 Apr. 2010).

5. Piekarewicz, J. Pygmy dipole resonance as a constraint on the neutron skin of heavy nuclei. *Phys. Rev. C* **73,** 044325. https://link.aps.org/doi/10.1103/PhysRevC.73.044325 (4 Apr. 2006).

6. Goriely, S. Radiative neutron captures by neutron-rich nuclei and the r-process nucleosynthesis. *Physics Letters B* **436,** 10–18. ISSN: 0370-2693. https://www.sciencedirect.com/science/article/pii/S0370269398009071 (1998).

7. Toft, H. K. *et al.* Level densities and $\gamma$-ray strength functions in Sn isotopes. *Phys. Rev. C* **81,** 064311. https://link.aps.org/doi/10.1103/PhysRevC.81.064311 (6 June 2010).

8. Carlos, P. *et al.* The giant dipole resonance in the transition region of the samarium isotopes. *Nuclear Physics A* **225,** 171–188 (1974).

9. Carlos, P., Beil, H., Bergere, R., Lepretre, A. & Veyssiere, A. The giant dipole resonance in the transition region for the neodymium isotopes. *Nuclear Physics A* **172,** 437–448. ISSN: 0375-9474. https://www.sciencedirect.com/science/article/pii/0375947471907251 (1971).

10. Itoh, M. *et al.* The effect of deformation in the isoscalar giant dipole resonance. *Nuclear Physics A* **731,** 41–48 (Feb. 2004).

11. Krugmann, A. *et al.* Low-energy dipole modes in the heavy deformed nucleus $^{154}$Sm via inelastic polarized proton scattering at 0°. *EPJ Web of Conferences* **38,** 11001. https://doi.org/10.1051/epjconf/20123811001 (2012).

12. Krugmann, A. *Off-Yrast low-spin structure of deformed nuclei at mass number A≈150* en. PhD thesis (Technische Universität, Darmstadt, June 2014). http://tuprints.ulb.tu-darmstadt.de/4289/.

13. Yoshida, K. & Nakatsukasa, T. Shape evolution of giant resonances in Nd and Sm isotopes. *Phys. Rev. C* **88,** 034309. https://link.aps.org/doi/10.1103/PhysRevC.88.034309 (3 Sept. 2013).

14. Bhat, R., Devi, R. & Khosa, S. Microscopic study of deformation systematics in the samarium mass chain. *Bulg. J. Phys* **29,** 114–127 (2002).

15. Paar, N., Vretenar, D., Khan, E. & Colò, G. Exotic modes of excitation in atomic nuclei far from stability. *Reports on Progress in Physics* **70,** R02. arXiv:nucl-th/0701081 (May 2007).

16. Lanza, E., Pellegri, L., Vitturi, A. & Andrés, M. Theoretical studies of Pygmy Resonances. *Progress in Particle and Nuclear Physics* **129,** 104006. ISSN: 0146-6410. https://www.sciencedirect.com/science/article/pii/S0146641022000643 (2023).

17. Savran, D., Aumann, T. & Zilges, A. Experimental studies of the Pygmy Dipole Resonance. *Progress in Particle and Nuclear Physics* **70,** 210–245. ISSN: 0146-6410. https://www.sciencedirect.com/science/article/pii/S0146641013000057 (2013).

18. Bracco, A., Lanza, E. & Tamii, A. Isoscalar and isovector dipole excitations: Nuclear properties from low-lying states and from the isovector giant dipole resonance. *Progress in Particle and Nuclear Physics* **106,** 360–433. ISSN: 0146-6410. https://www.sciencedirect.com/science/article/pii/S0146641019300031 (2019).

19. Steinwedel, H. & D.Jensen, J. Hydrodynamik von Kerndipolschwingungen. *Zeitschrift für Naturforschung A* **5,** 413–420. https://doi.org/10.1515/zna-1950-0801 (1950).

20. Bastrukov, S., Molodtsova, I., Podgainy, D., Mişicu, Ş. & Chang, H.-K. Elasticity of nuclear medium as a principal macrodynamical promoter of electric pygmy dipole resonance. *Physics Letters B* **664,** 258–264. ISSN: 0370-2693. https://www.sciencedirect.com/science/article/pii/S0370269308006151 (2008).

21. Colò, G., Cao, L., Van Giai, N. & Capelli, L. Self-consistent RPA calculations with Skyrme-type interactions: The skyrme-rpa program. *Computer Physics Communications* **184,** 142–161. ISSN: 0010-4655. https://www.sciencedirect.com/science/article/pii/S0010465512002627 (2013).

22. Savran, D. *et al.* Fragmentation and systematics of the pygmy dipole resonance in the stable $N = 82$ isotones. *Phys. Rev. C* **84,** 024326. https://link.aps.org/doi/10.1103/PhysRevC.84.024326 (2 Aug. 2011).

23. Van Giai, N. & Sagawa, H. Spin-isospin and pairing properties of modified Skyrme interactions. *Physics Letters B* **106,** 379–382. ISSN: 0370-2693. https://www.sciencedirect.com/science/article/pii/0370269381906468 (1981).

24. Van Giai, N. & Sagawa, H. Monopole and dipole compression modes in nuclei. *Nuclear Physics A* **371,** 1–18. ISSN: 0375-9474. https://www.sciencedirect.com/science/article/pii/0375947481907417 (1981).

25. Isaak, J. *et al.* Dipole response in $^{128,130}$Te below the neutron threshold. *Phys. Rev. C* **103,** 044317. https://link.aps.org/doi/10.1103/PhysRevC.103.044317 (4 Apr. 2021).

26. Goddard, P. M. *et al.* Dipole response of $^{76}$Se above 4 MeV. *Phys. Rev. C* **88,** 064308. https://link.aps.org/doi/10.1103/PhysRevC.88.064308 (6 Dec. 2013).

27. Massarczyk, R. *et al.* Nuclear Deformation and Neutron Excess as Competing Effects for Dipole Strength in the Pygmy Region. *Phys. Rev. Lett.* **112,** 072501. https://link.aps.org/doi/10.1103/PhysRevLett.112.072501 (7 Feb. 2014).

28. Alaga, G. Selection rules for beta and gamma particle transitions in strongly deformed nuclei. *Nuclear Physics* **4,** 625–631. ISSN: 0029-5582. https://www.sciencedirect.com/science/article/pii/0029558287900666 (1957).

29. Papst, O. *et al.* Photo response of $^{164}$Dy. *Phys. Rev. C* **102,** 034323. https://link.aps.org/doi/10.1103/PhysRevC.102.034323 (3 Sept. 2020).

30. Tamkas, M. *et al.* Low-lying dipole strength in the well-deformed nucleus $^{156}$Gd. *Nuclear Physics A* **987,** 79–89. ISSN: 0375-9474. https://www.sciencedirect.com/science/article/pii/S0375947419300661 (2019).

31. Harakeh, M. N. & van der Woude, A. *Giant Resonances: Fundamental High-Frequency Modes of Nuclear Excitation* (Oxford: Clarendon Press, 2001).

32. Harakeh, M. N. & Dieperink, A. E. L. Isoscalar dipole resonance: Form factor and energy weighted sum rule. *Phys. Rev. C* **23,** 2329–2334. https://link.aps.org/doi/10.1103/PhysRevC.23.2329 (5 May 1981).

33. Litvinova, E., Ring, P. & Tselyaev, V. Relativistic quasiparticle time blocking approximation: Dipole response of open-shell nuclei. *Phys. Rev. C* **78,** 014312. https://link.aps.org/doi/10.1103/PhysRevC.78.014312 (1 July 2008).

34. Cramer, J. & Eidson, W. Angular correlations and nuclear polarization from the inelastic scattering of alpha particles. *Nuclear Physics* **55,** 593–612. ISSN: 0029-5582.

https://www.sciencedirect.com/science/article/pii/0029558264901798 (1964).

35. Harakeh, M. & Put, L. W. *ANGCOR Program code* (Private Communication).

36. *AngCor Package* Available at https://github.com/padsley/AngCorPackage.

37. Rybicki, F., Tamura, T. & Satchler, G. Particle-gamma angular correlations following nuclear reactions. *Nuclear Physics A* **146,** 659–676. ISSN: 0375-9474. https://www.sciencedirect.com/science/article/pii/0375947470907487 (1970).

38. Rose, H. J. & Brink, D. M. Angular Distributions of Gamma Rays in Terms of Phase-Defined Reduced Matrix Elements. *Rev. Mod. Phys.* **39,** 306–347. https://link.aps.org/doi/10.1103/RevModPhys.39.306 (2 Apr. 1967).

39. Kunz, P. & Comfort, J. *Modified CHUCK3 Program code* Available at https://github.com/padsley/CHUCK3.

40. Nolte, M., Machner, H. & Bojowald, J. Global optical potential for $\alpha$ particles with energies above 80 MeV. *Phys. Rev. C* **36,** 1312–1316. https://link.aps.org/doi/10.1103/PhysRevC.36.1312 (4 Oct. 1987).

41. Harakeh, M. N. & Dieperink, A. E. L. Isoscalar dipole resonance: Form factor and energy weighted sum rule. *Phys. Rev. C* **23,** 2329–2334. https://link.aps.org/doi/10.1103/PhysRevC.23.2329 (5 May 1981).

42. Rose, M. E. The Analysis of Angular Correlation and Angular Distribution Data. *Phys. Rev.* **91,** 610–615. https://link.aps.org/doi/10.1103/PhysRev.91.610 (3 Aug. 1953).

43. Adsley, P., Li, K., Jivan, H., Morris, L. & Pellegri, L. *A practical guide to using the AngCor package* 2019. arXiv: 2001.11104 [nucl-ex].

0. Neveling, R. *et al. Guide to the K600 magnetic spectrometer* (June 2020 version).

45. Fujita, H. *et al.* Realization of matching conditions for high-resolution spectrometers. *Nuclear Instruments and Methods in Physics Research A* **484,** 17–26 (2002).

46. Neveling, R. *et al.* High energy-resolution zero-degree facility for light-ion scattering and reactions at iThemba LABS. *Nuclear Instruments and Methods in Physics Research A* **654,** 29–39 (2011).

47. Bertozzi, W. *et al.* Focal Plane Instrumentation: A very high resolution MWPC system for inclined tracks. *Nuclear Instruments and Methods* **141,** 457–476 (1977).

48. *MIDAS Wiki Page* Available at http://midas.triumf.ca.

49. *k600analyser code* Available at https://github.com/padsley/k600analyser.

50. Brun, R. *et al. ROOT Data Analysis Framework* version v6-18-02. Aug. 2019. https://root.cern/about/.

51. *jRelKin code* Available at http://nukesim-classes.sourceforge.net/software_index.html.

52. Agostinelli, S. & et. al. Geant4—a simulation toolkit. *Nuclear Instruments and Methods A* **506,** 250–303 (2003).

53. *k600 GEANT simulation code* Available at https://github.com/KevinCWLi/K600.

54. Löher, B. *et al.* The decay pattern of the Pygmy Dipole Resonance of 140Ce. *Physics Letters B* **756,** 72–76. ISSN: 0370-2693. https://www.sciencedirect.com/science/article/pii/S0370269316001386 (2016).

55. Savran, D. *et al.* Model-independent determination of the dipole response of $^{66}$Zn using quasimonoenergetic and linearly polarized photon beams. *Phys. Rev. C* **106,** 044324. https://link.aps.org/doi/10.1103/PhysRevC.106.044324 (4 Oct. 2022).

56. Volz, S. *et al.* The photoresponse of stable N=82 nuclei below 10 MeV. *Nuclear Physics A* **779,** 1–20. ISSN: 0375-9474. https://www.sciencedirect.com/science/article/pii/S0375947406005823 (2006).